UNIVERSITY OF CALIFORNIA
RIVERSIDE

Dynamic Models of Earthquake Rupture on Fault Stepovers and Dip-Slip Faults Using Various Friction Formulations

A Thesis submitted in partial satisfaction
of the requirements for the degree of

Master of Science

in

Geological Sciences

by

Kenny Ryan

December 2012

Thesis Committee:
Dr. David D. Oglesby, Chairperson
Dr. Elizabeth S. Cochran
Dr. James H. Dieterich

The Thesis of Kenny Ryan is approved:

_____

_____

_____
Committee Chairperson

University of California, Riverside

Acknowledgements

I would like to especially thank my committee members. First and foremost, David Oglesby, for being a great guide and mentor throughout the degree process. David has an invaluable talent for explaining difficult concepts and problem solving. Additionally, I would like to thank Elizabeth Cochran and Jim Dieterich for their thoughtful comments and corrections. The geophysics group has also helped be hone in on a valuable scientific skillset. Also, I'd like to thank my family members for their support; many times they have helped me stay on track, even with my consistently hectic schedule. They have also kept me grounded and made me a more well-rounded person. Lastly, I'd like to thank Corrie Neighbors for her support and understanding along the way. Not only has she encouraged me and shown confidence in my abilities, but she helped me realize I can set challenging goals and succeed.

Table of Contents

List of Figures

List of Tables

Introduction

Earthquake faults throughout the Earth are quite heterogeneous with respect to geometric and material properties, and determining how these properties influence earthquake rupture is an ongoing challenge in seismology. One such geometric complexity is a fault stepover: a set of discontinuous, parallel fault segments that are offset from each other at the Earth's surface. The fault segments may overlap or have gaps along strike. Observationally, fault stepovers are found around the world. Wesnousky (1988) examined fault steps in California and Turkey and suggested that faults steps impede earthquake ruptures, since more energy is needed to jump from one fault segment to the next than to propagate along a single fault segment. Additionally, Wesnousky (1988) further suggests that the number of steps along large strike-slip faults decrease with time as cumulative slip smoothes out the fault. Whether or not rupture jumps from one segment to the next is critically important for hazard analysis, since seismic moment is proportional to the ruptured area, and the ground motion distribution also depends quite strongly on the pattern of ruptured faults. The 1992 Landers, California, M_w 7.2 earthquake is a prime example of such a case—it ruptured at least 5 major faults with a right-stepping geometry to the north, and was the largest earthquake in the contiguous United States in 40 years (Sieh et al., 1993).

Non-vertical dip-slip faults, on which seismic slip is parallel to the dip angle, have a geometrical and mass asymmetry between the hanging wall and the footwall near the Earth's surface. In reverse/thrust faults the hanging wall is thrust over the footwall and

the footwall is pushed under the hanging wall (under compression), while in normal faults the hanging wall and footwall slide away from each other (under extension). Earthquakes on these fault types are also observed around the world (e.g., Ekström et al., 2012). One such event was the 1978 Tabas-e-Golshan, Iran, M_s 7.4 earthquake, a thrust event that killed 20,000 people and destroyed over 15,000 houses (Berberian, 1982). Reverse/thrust earthquakes are often associated with more intense ground motion than normal earthquakes. Cocco and Rovelli (1989) found evidence of larger peak ground motions for a group of thrust earthquakes in Friuli, Italy, 1976, versus a group of normal earthquakes in the Apennines region of Italy from 1979 to 1984.

Studying both complex fault geometries, e.g., fault stepovers, as well as asymmetric geometries, e.g., non-vertical dip-slip faults, can provide information for earthquake hazard mitigation. One way to study these earthquake types is dynamic modeling, in which the earthquake and corresponding motion is simulated computationally, in time. Since actual earthquakes involve two sides of a fault surface sliding against each other, friction is an inherent part of earthquake processes. Therefore, in order to simulate an earthquake dynamically one must implement friction parameters. For example, Ida (1972) examined the elastic wave field around a crack tip and the condition for rupture growth under the assumption that frictional strength decreases with displacement. Andrews (1976b) implemented this method by modeling earthquake rupture with the stipulation that, for a point on the fault surface, shear stress decreases with displacement. Using the finite element computer code FaultMod (Barall, 2008) we combine complex

and asymmetric fault geometries with laboratory-based friction laws to examine how faults, with certain geometries and friction laws, rupture.

First Order Complex and Asymmetric Fault Geometries

For years earthquake physicists have implemented complex and asymmetric fault geometries into computer codes that simulate earthquake rupture. Many numerical studies of stepovers examine two basic types of the strike-slip variety: compressional and dilational (extensional) stepovers (Segall and Pollard, 1980; Harris et al., 1991; Harris and Day, 1993; Kase and Kuge, 1998; Harris and Day, 1999; Duan and Oglesby, 2006; Oglesby, 2008). With compressional stepovers fault slip results in compression in the region between the fault segments and with dilational stepovers fault slip results in extension in the region between the fault segments. Those indicate the generation of strong perturbations in dynamic stresses between the offset fault segments during earthquake rupture. In this study we model strike-slip stepovers, both compressional and dilational, comprised of planar fault segments that have variable offset distances. Additionally, some laboratory and numerical studies have focused on modeling reverse/thrust and normal faults that intersect the free surface or are buried (Brune, 1996; Nielsen, 1998, Oglesby et al., 1998; Oglesby and Archuleta, 2000a; Oglesby et al., 2000b). These studies indicate strong perturbations in dynamic normal stress, for both reverse/thrust and normal fault ruptures as waves from the rupture reflect off the free surface and hit the fault again, causing dynamic clamping and unclamping (buried faults

dramatically reduce this effect). In this study we model a fixed geometry for both reverse and normal-type ruptures on planar faults that intersect the free surface.

Friction Laws

It is well known that earthquake ruptures are controlled by friction on faults. The general friction equation for a point on an interface (e.g., fault surface) without cohesion is:

$$\tau \leq \mu\sigma^{eff} \tag{1}$$

where τ is the shear stress, μ is the friction coefficient, and σ^{eff} is the effective normal stress (positive in compression in our notation). When the shear stress at that point becomes equal to the friction coefficient multiplied by the normal stress, sliding commences, relieving the shear stress at that same point. Before, during, and after this process, the friction coefficient and effective normal stress may also change. When the shear stress is smaller than the product of the former two, sliding ceases. For earthquakes this is a cyclic process that helps explain why earthquakes occur every so many years along the same faults. It is intuitive that dynamic (kinetic) coefficients of friction are often smaller than their static counterparts – sliding a heavy cardboard box across a slick household floor demonstrates this. Initially it is more difficult to move, but once the box begins sliding it becomes easier. The nature of such coefficients of friction has been explored in the laboratory for many years (Rabinowicz, 1951).

One such friction formulation that describes this observation is slip-weakening friction (Ida, 1972):

$$\mu = \begin{cases} \dfrac{\mu_{dynamic} - \mu_{static}}{d_o} d\delta + \mu_{static}, & d\delta < d_o \\ \mu_{dynamic}, & d\delta \geq d_o \end{cases} \tag{2}$$

where δ is displacement and d_o is a slip distance over which the friction coefficient drops from its static value to its kinetic value, and is referred to as the effective slip-weakening distance. For computational studies, a nonzero value of d_o is necessary to resolve the stress drop (i.e., rupture front) with more than one time step. It is also a reasonable physical assumption, since energy being focused by seismic waves driving rupture is probably not focused at a single point, but a finite volume (Andrews, 1976b), leading to an apparent surface energy associated with the onset of fault slip. Additionally, laboratory studies on rock friction show gradual stress drops (Dieterich, 1978b, 1979). Andrews (1976b, 1985) was a pioneer in using the slip-weakening formulation to model spontaneous earthquake rupture in 2-D.

More complex and realistic friction formulations have also been developed from laboratory experimentation. One such formulation is rate- and state-dependent friction (Dieterich, 1978b, 1979; Ruina, 1983). Dieterich (1978) shows that, through experiments and analysis of a spring slider system, the friction coefficient of rock varies with time and slip velocity. More specifically, the static friction increases with stationary contact time, and the dynamic friction also changes with the contact time of sliding asperities – small

contact surfaces across the fault that are continually sliding into and out of existence – as well as with slip velocity history. Dieterich (1979) further shows through laboratory experiments that a positive increase in slip speed leads to an abrupt increase in frictional strength, after which the frictional strength falls toward a dynamic value. Using the constitutive relations proposed by Dieterich (1978b, 1979), Ruina (1983) formulated state variable friction laws that include the time and velocity dependence of friction coefficient. The general form of the rate- and state-dependent friction law is:

$$\tau = \left[\mu_o + a \ln\left(\frac{V}{V_o}\right) + b \ln\left(\frac{\theta}{\theta_o}\right) \right] \sigma^{eff} \tag{3}$$

where μ_o represents a constant reference value for the coefficient of friction; a and b are constitutive parameters estimated from laboratory experiments; V_o and θ_o are reference values for slip rate and the state of the sliding surface, respectively; θ can be thought of as the average age of contacts at some sliding velocity, and the bracketed term is the friction coefficient. Note that for an increase in sliding velocity V there is a corresponding increase in friction, and as sliding velocity grows the asperities are in contact for smaller amounts of time, making θ small and ultimately decreasing friction. Later, Linker and Dieterich (1992) further developed the rate-state framework to include the friction coefficient's dependence on normal stress. They found that increases in normal stress led to decreases in the state variable θ and decreases in normal stress led to increases in θ. This result indicates that the friction coefficient at least partially compensates for changes in normal stress.

Finite Element Code FaultMod

FaultMod is a finite element method (FEM) computer code developed by Michael Barall, of Invisible Software, Inc. (Barall, 2008). For the U.S. Geological Survey it is specially designed for physics-based dynamic models of earthquake rupture on faults with complex and asymmetric geometries and complex material properties (Barall, 2009). Generally, finite element codes divide a given continuum of mass (e.g., the Earth's surface) into a number of elements that can then be used to run computations on (e.g. Hughes, 2000). For dynamic earthquake simulations this process involves solving non-equilibrium force balance equations and time stepping. The elemental shapes are hexahedral in this study, such that the fault and surrounding region are constructed of these six-sided elements, making a mesh. FaultMod has a built-in mesh generator that creates the mesh before the simulation begins. Calculations for each time step are done on the vertices of elements (i.e. nodes), except for stress calculations, which are done at the centroids of the elements. For points that would lie on a fault, there are two concurrent nodes, a common node and a differential node. The common node is the node that would be at a location with no fault, whereas the differential node has degrees of freedom corresponding to motion of one side of the fault relative to the other side. This way fault slip can be calculated. FaultMod performs earthquake simulations on all nodes in the following fashion:

(1) A trial step, assuming the same accelerations from the previous time step

(2) Calculate nodal forces due to the time-stepped accelerations in (1)

(3) Solve for fault slip, slip rate, and acceleration

(4) Apply solutions of fault slip, slip rate, and acceleration as kinematic boundary conditions

(5) Solve force balance equations to obtain displacement, velocity, and acceleration along all nodes in the mesh

(6) Update all variables

In order to solve (3) a friction law must be used, and several friction laws are implemented in FaultMod, including slip-weakening and rate-state friction (above). Simulations in this study are 2-D and are constrained to allow motion only parallel to the plane (plane strain). Although FaultMod can incorporate different types of materials, we assume a homogeneous linearly elastic material. Additionally, FaultMod only allows isotropic materials. The mass of each element is lumped at the vertices.

Summary

The functional form of the friction law employed in dynamic earthquake simulations is directly related to the energy partitioning of rupture and slip (e.g., Kanamori and Rivera, 2006). Earthquake ruptures can propagate along geometrically complex faults by turning and jumping along fault segments (Wesnousky, 1988), however, this is dependent on how much energy is available to further rupture propagation and how much energy is needed. For planar fault stepovers with homogeneous stress, rupture can jump segments or it can arrest at the edge of a segment. Since friction laws, along with stress regimes, implicitly specify the energy budget, different laws can lead to different rupture

dynamics. Using realistic, laboratory-derived friction laws to simulate rupture is a constant ambition in seismology. The rate-state friction formulation includes intuitive variables such as time, slip speed history, and normal stress history as well as exhibits reasonable properties such as stick-slip sliding, creep, and healing (Dieterich, 1978b, 1979; Linker and Dieterich, 1992). Particularly, including the change in friction coefficient with normal stress history is imperative for earthquakes that produce large dynamic fluctuations in normal stress, including both stepovers and dip-slip faults that penetrate the free surface.

In this study we use FaultMod to run dynamic earthquake simulations on fault stepovers using the various friction formulas listed above. Firstly, we investigate effects of the functional form of the friction laws on jumping rupture at stepovers. The functional forms are associated with unique energy budgets that can determine how far rupture can jump within a given amount of time. We find that making the energy budgets similar between the friction parameterizations makes the rupture processes more similar at the stepover region (e.g., similar maximum jump distances). We also find that for larger jumps the rupture speeds increase to supershear speeds, even though the initial stress conditions would preclude such a result on a planar strike-slip fault (Andrews, 1976b). Secondly, we add to the stepover simulations by introducing the Linker-Dieterich formulation, in which friction coefficient depends on normal stress. It is well known that stepovers exhibit perturbations in normal stress along the offset region during rupture, with the sign being opposite for compressional and dilational stepovers. Adding the normal-stress-

dependent state variable to the friction formulation decreases the maximum rupture jump for both types of stepover, however.

Additionally, we apply the Linker-Dieterich formulation to normal and reverse dip-slip faults, both of which are known to exhibit dynamic fluctuations in normal stress due to the free surface (Brune, 1996; Nielsen, 1998; Oglesby et al., 1998). Differences in shear stress direction between normal and reverse faults produce asymmetric normal stress perturbations along the fault during rupture, causing the motion from a reverse fault to be larger than that of an otherwise equivalent normal fault. Adding a normal-stress-dependent state variable serves to mitigate this effect. We also find that decreasing the initial shear stress inhibits rupture more on normal faults than on reverse faults, given that the faults intersect the free surface. More specifically, smaller initial shear stress results in slower rupture propagation for dip-slip models. Thus, the relative position of the rupture front to dynamic changes in normal stress is altered, resulting in reverse fault ruptures traveling updip in a region of decreased normal stress, and normal fault ruptures traveling updip in a region of increased normal stress.

Chapter 1: Using Various Friction Laws to Dynamically Model Fault Stepovers

Abstract

It is well known from both observational and numerical studies that fault stepovers can under some circumstances allow through-going rupture, and under other circumstances cause rupture to terminate (e.g., Wesnousky, 1988; Knuepfer, 1989; Harris and Day, 1993; Kase and Kuge, 1998; Duan and Oglesby, 2006). Past studies have shown that the dynamics (e.g., slip, slip rate, stress drop) of earthquakes are affected by the choice of frictional parameterization. However, the effects of different friction law formulations on jumping rupture have not been extensively explored. In this study we use numerical models to investigate how 4 different frictional parameterizations affect the ability of rupture to jump a stepover. We compare linear slip-weakening friction (Ida, 1972; Palmer and Rice, 1973; Andrews, 1976b) and 3 forms of rate- and state-dependent friction (Dieterich, 1978b, 1979; Ruina, 1983): the ageing law, slip law, and slip law with strong rate-weakening (e.g., Rice, 1999, 2006; Beeler and Tullis, 2003; Beeler et al., 2008; Rojas et al., 2009). We use the 2-D dynamic finite element method (Barall, 2008) to model earthquake rupture along strike-slip stepovers, in both extensional and compressional settings. We have found that for parameterizations with the same effective slip-weakening distance, friction laws with similar functional forms (i.e., the ageing law vs. slip-weakening friction) have similar maximum jump distances, while those with significantly different functional forms (i.e., the ageing law and slip-weakening friction vs. the slip law) can have large relative differences in maximum jump distance. Average fracture energy is specific to the functional form of each friction formulation, and exerts a

strong control on the maximum jump distance perpendicular to strike. In particular, we find that the slip law, which has lower fracture energy for a given effective slip-weakening distance than the ageing law or the slip-weakening law, allows rupture to jump larger stepover widths than the ageing or slip-weakening law. With friction laws scaled to have equivalent fracture energies (but different effective slip-weakening distances), we find that the functional form of the friction law has a second-order effect on jumping rupture, with friction laws with steeper initial weakening (e.g., the slip law) allowing longer jumps. Finally, with our specific parameterizations we find that delays in rupture across the stepover systems can lead to a previously-unseen mode of supershear transition once the rupture re-nucleates on the secondary fault segment, even if the stress field on the system prior to rupture is such that a standard Burridge-Andrews supershear transition would be precluded (Burridge, 1973; Andrews, 1976b). Studies of multiple friction laws in complex geometries such has fault stepovers can lead to more realistic rupture dynamics and better understanding the dependence of rupture properties on the type of friction law utilized in models and statistical analysis.

Introduction

The purpose of this study is to compare rupture properties along strike-slip fault stepovers using several friction formulations. Fault stepovers are systems of parallel, disconnected fault segments offset from one another at the Earth's surface. There can also be some overlap, no overlap, or gaps in the along-strike direction between the fault segments. Strike-slip stepovers, specifically, are such systems with two or more strike-

slip fault segments. The amount of horizontal offset between the strikes of the fault segments is referred to as step width. In nature, fault stepover widths from cm to km have been observed (Vedder and Wallace, 1970; Bartlett et al., 1981). Whether or not an earthquake rupture terminates at or jumps across a fault stepover is critical in determining the ultimate magnitude of such an event. There have been many benchmark studies on fault steps over the past three decades including both numerical (e.g., Segall and Pollard, 1980; Harris and Day, 1993; Kase and Kuge, 2001; Duan and Oglesby, 2006) and observational (e.g., Wesnousky, 1988; Sieh al., 1993; Lettis et al., 2002; Wesnousky, 2006) studies. Such studies show that earthquakes are preferentially stopped by larger stepover widths – the offset distance of the fault segments in a stepover system. In particular, field observations suggest that earthquake ruptures may not jump compressional stepovers with step widths greater than 5 km or dilational stepovers with step widths greater than 8 km (Wesnousky, 1988; Knuepfer, 1989). In addition to showing that ruptures may jump dilational stepovers more easily than compressional stepovers, some studies further indicate that dilational stepovers can have larger rupture delays at the stepover region than compressional cases (Harris and Day, 1993). Additionally, the location of rupture re-nucleation on the secondary segment of a stepover system varies depending on whether the system is compressional or dilational. Nucleation typically occurs after rupture along the primary segment has terminated (e.g., Harris and Day, 1993; Kase and Kuge, 1998). Additionally, stopping phases – seismic radiation that results from the abrupt end of primary fault – are shown to control the ability of rupture to jump across a stepover in both numerical and observational studies

(Bernard and Madariaga, 1984; Spudich and Frazer, 1984; Oglesby, 2008; Elliot et al., 2009).

It is well known that earthquakes are a result of stored elastic energy due to friction on faults. Additionally, the friction coefficient partially determines the dynamics during rupture. All of the numerical studies of stepovers cited above utilize linear slip-weakening (SW) friction (Ida, 1972; Palmer and Rice, 1972; Andrews, 1976). However, there have been no thorough investigations of the rupture properties of stepovers using laboratory-derived friction laws such as rate- and state-dependent friction (Dieterich, 1978b, 1979; Ruina, 1983), which could provide more realistic representations of rupture nucleation and dynamics. Rate- and state-dependent (RS) friction laws are controlled by slip velocity and time evolution of one or more state variables, but typically show an effective slip-weakening behavior at the onset of slip, as pointed out by Okubo (1989), Dieterich and Kilgore (1994), and Bizzarri et al. (2001). A state variable within the RS friction formulation can be thought of as related to strength of contacts, assuming the contacts become stronger as they mature. Because RS friction parameterizations have been indicated in laboratory experiments, they provide a reasonable basis on which to model the dynamics of earthquake rupture. For a given parameterization, friction laws can be characterized in terms of their effective slip-weakening curves at the onset of earthquake rupture. Steep slip-weakening curves indicate that relatively less fracture energy is needed for rupture to start and propagate, when compared to shallower curves with the same stress drop. For SW friction, the coefficient of friction drops linearly with

slip. The RS ageing law also has a relatively linear drop in friction with slip (compared to the slip law). However, many lab studies, including high-speed experiments, show nonlinear slip-weakening curves (Dieterich, 1979; Tsutsumi and Shimamoto, 1997; Prakash 1998; Prakash and Yuan, 2004; Tullis and Goldsby 2002, 2003a, 2003b; and Hirose and Shimamoto, 2005). Accordingly, the RS slip law has an initially steeper, concave-up functional form with slip (Ruina, 1980; Ruina, 1983). Therefore, the RS slip law may be a more viable friction formulation from an experimental perspective than friction parameterizations that lead to more linearly shaped slip-weakening curves.

Some dynamic rupture simulation studies implement the RS framework (e.g., Okubo, 1989) including strong rate-weakening friction (e.g., Zheng and Rice, 1998; Rojas et al., 2009), in which shear stress at a point on the fault surface drops considerably around some sliding velocity. It is well known that not many pseudotachylites are found near faults, possibly because of low friction (Sibson, 1973). Strong rate-weakening friction allows for a substantial drop in the friction coefficient with increasing slip velocity, thereby simulating, for example, flash heating, or melting of micro-asperities (Rice, 1999, 2006; Beeler and Tullis, 2003; Beeler et al., 2008). Strong rate-weakening frictional behavior is observed in laboratory experiments by Tsutsumi and Shimamoto (1997), Prakash (1998, 2004), Tullis and Goldsby (2002, 2003a, 2003b), and Hirose and Shimamoto (2005) at high slip rates ($\approx$ 1 m/s). The experimental studies cited above agree that the velocity at which substantial weakening occurs is on the order of 0.2 m/s, while the static and sliding coefficients of friction range between 0.6 – 0.9 and 0.2 – 0.3,

respectively. Using these values in earthquake simulations can help investigate the effect of such weakening mechanisms at stepover regions. Although large reductions in frictional coefficient over sizeable lengths of fault could imply unrealistically large stress drops, strong rate-weakening friction may be possible over small sections of fault on the order of kilometers (Nielsen and Olsen, 2000).

The functional form of frictional weakening is directly related to the earthquake rupture energy budget (e.g., Andrews, 1976b; Kanamori and Rivera, 2006). The total energy of the earthquake can be split into 3 categories: fracture energy, energy expended against friction, and radiated seismic energy. Fracture energy can also be thought of in relation to the average slip of a rupture zone (Rice, 2006) if the stress-slip weakening curve associated with friction continually decreases, on average across the fault, until slip ceases. In this case the effective slip weakening distance d_o – the slip distance over which the stress drops during the rupture process (Rabinowicz, 1951) – would be equal to the average total slip across the fault. The effective fracture surface energy (EFSE) for a specific location along a rupture defined by Palmer and Rice (1973) and Andrews (1976b) is:

$$G = \int_0^{d_o} \left(\tau(\delta) - \tau_f \right) d\delta \tag{1.1}$$

where τ is the shear stress, and δ is the cumulative slip. Many numerical studies constrain the EFSE to be relatively constant over the rupture surface; however, this assumption is not necessarily realistic. For example, Andrews (2005) points out that EFSE (and therefore d_o) is not constant along rupture and grows as a result of the

dynamics of the earthquake process. Inelastic deformation within the damage zone of a fault should also contribute to the energy budget of the earthquake (for numerical simplicity, it is commonly lumped together with the fracture energy). It should be noted that estimating the EFSE can be somewhat subjective for nonlinear friction formulations due to a subjective choice of d_o (e.g., Bizzarri and Cocco, 2003; Rojas et al. 2009). Because the shape of the stress-versus-slip curve can be different for different friction laws, the energy budget of a simulated earthquake is directly related to the friction parameterization. It is widely known that dynamic models exhibit undershoot or overshoot of sliding stresses (e.g., Mai et al., 2006) and can lead to uncertainties in the EFSE. For SW friction, d_o is more easily defined and implemented numerically. However, RS friction has no easily defined d_o variable among its parameters. Among the RS formulation, the constitutive parameter L – represented as a characteristic slip distance – is closely related to d_o. Cocco and Bizzarri (2002) show that L and d_o are linearly proportional, and that for typical parameters the ratio d_o/L is approximately 15 for the RS ageing law.

Earthquake rupture speed has proven to be an extremely important aspect of seismology in that it is directly related to key aspects of earthquakes including slip, stress drop, and ground motion. The ability of rupture to propagate at supershear rupture speed is particularly important because such a rupture can produce relatively larger fault-parallel particle motion, and the resulting Mach cones carry large stresses and particle velocities far from the fault (e.g., Dunham and Archuleta, 2004; Bernard and Baumont, 2005).

Supershear rupture velocities are inferred from several seismic observations of the 1979 Imperial Valley earthquake, the 1992 Landers earthquake, the 1999 Izmit earthquake, the 2001 Kunlun earthquake, and the 2002 Denali Fault earthquake (e.g., Archuleta, 1982; Olson and Apsel, 1982, Spudich and Cranswick, 1984; Olsen et al., 1997; Bouchon and Vallée, 2003, Ellsworth et al. 2004). Laboratory experiments show supershear transition of mode II cracks along homogeneous interfaces (Rosakis et al., 1999; Rosakis 2002; Xia et al., 2004)) and bi-material interfaces (Xia et al., 2005). Supershear rupture propagation is also predicted and explored in many computational and theoretical studies (e.g., Andrews, 1976; Day, 1982b; Harris and Day, 1997; Cochard and Rice, 2000; Madariaga and Olsen, 2000; Fukuyama and Olsen, 2002; Dunham et al., 2003). Burridge (1973) and Andrews (1976b) demonstrate that a traveling shear wave in front of a rupture front can increase stress to the yield level ahead of the crack tip, resulting in a "daughter" crack that travels along the fault interface at supershear speed. For Mode II rupture, rupture speeds are limited to either $V_{rupt} \leq V_{Rayleigh}$ or $V_{rupt} \geq V_{shear}$ for energetically favorable conditions (i.e., rupture speeds between the Rayleigh and Shear wave speeds are prohibited). Dynamic modeling parameter studies show that the seismic S ratio

$$S = \left[\frac{\left(\tau_y - \tau_0 \right)}{\left(\tau_0 - \tau_f \right)} \right] \tag{1.2}$$

where τ_y is the yield strength, τ_o is the initial loading stress, and τ_f is the final sliding stress, controls the ability of rupture to make the transition to supershear speed on planar faults (Andrews, 1976b; Das and Aki, 1977; Day, 1982b). For 2-D simulations, S = 1.77

is the threshold value, above which ruptures cannot make the transition to supershear speeds (Andrews, 1976b).

For values of S between 0 and 1.77, there is an associated transition length L_{trans} (e.g., Xia et al., 2004)

$$L_{trans} = f(S)\left[\frac{(1+\nu)}{\pi}\right]\left[\frac{\left(\tau_y - \tau_f\right)}{\left(\tau_0 - \tau_f\right)^2}\right]Gd_0 \tag{1.3}$$

$$f(S) = \frac{9.8}{\left(1.77 - S\right)^3} \tag{1.4}$$

where ν is Poisson's ratio and G is the shear modulus. A sub-Rayleigh rupture must travel a distance L_{trans} before supershear speed is reached. Liu and Lapusta (2008) show that "favorable heterogeneities", such as a preexisting subcritical crack or small patch of high prestress could facilitate mode II cracks changing from sub-Rayleigh to supershear speed (as a secondary crack is driven to supershear speed by the main crack). Dunham (2007) demonstrates that changes in fracture energy and stress drops along strike could lead to the supershear transition. Additionally, Dunham (2007) shows that the supershear transition length can be sensitive to the effective slip-weakening distance curve, specific to the friction formulation used, i.e., the transition length is smaller for more rapid decreases in stress with slip due to smaller critical nucleation lengths.

Prior studies that investigate the effects of frictional parameterization on rupture dynamics have focused on planar faults, and studies of fault dynamics on non-planar

faults have almost entirely used simple SW friction. Few studies have seen supershear transitions that result from complex fault geometries such as fault stepovers (e.g., Oglesby et al., 2008). The seismic S ratio is not only important as a predictor for supershear transition, but can also help determine maximum jumping rupture lengths along fault stepovers (Harris and Day, 1993). The use of multiple types of friction formulations in such studies could provide some generality to results concerning the jump-ability and rupture speed at stepovers, or at least relative values of such parameters among different friction parameterizations. Analyzing several different friction formulations can help to illuminate the robustness of the results.

Method

2-D earthquake rupture models can provide reasonable tests on geometrical parameters and scale to 3-D quite well (e.g., Harris and Day, 1993; Harris and Day, 1999). In this study we use the 2-D finite element method (FEM) code FaultMod (Barall, 2008) to model mode II dynamic rupture, with a frictional interface, along fault stepovers, in both compressional and dilational settings (figure 1.1). Rupture is constrained to take place on one or both of two parallel fault segments. Each fault segment is 50 km in length, and the overlap between segments is 7 km. The overlap is large enough to allow rupture to re-nucleate on the secondary fault in both compressional and dilational settings. The stepover width, or offset distance, is variable and allows us to determine the maximum distance rupture can jump (perpendicular to strike) along stepovers with our parameterizations. FaultMod automatically generates meshes, uses grid doubling away

from the fault system to reduce computation resources without loss of accuracy, and has been validated in SCEC/USGS rupture benchmark problems (Barall, 2009; Harris et al., 2009). The code incorporates artificial viscous damping (Dalguer and Day, 2007) as well as algorithmic damping to help damp spurious oscillations, and energy-absorbing boundary conditions along the mesh edges to avoid artificial reflections from the model boundaries. We consider frictional effects on systems with relatively small and large absolute stress fields, with small and large stress drops, respectively (Tables 1.1-1.2). Large absolute stress fields are approximately 5 times that of the small absolute stress fields.

We compare four friction formulations, including linear slip-weakening (SW) friction and three forms of rate- and state-dependent friction: ageing law (RS-AL), slip law (RS-SL), and slip law with strong rate-weakening (RS-SRW). The criterion for linear slip-weakening friction is as follows (Ida, 1972):

$$\mu = \begin{cases} \dfrac{\mu_{dynamic} - \mu_{static}}{d_o} d\delta + \mu_{static}, & d\delta < d_o \\ \mu_{dynamic}, & d\delta \geq d_o \end{cases} \tag{1.5}$$

The general form of RS friction is (Ruina, 1980, 1983; Linker and Dieterich 1992):

$$\tau = \left[\mu_o + a \ln\left(\frac{V}{V_o}\right) + b \ln\left(\frac{\theta}{\theta_o}\right) \right] \sigma^{eff} \tag{1.6}$$

where μ_o represents a constant reference value for the coefficient of friction; a and b are constitutive parameters estimated from laboratory experiments; V_o and θ_o are reference values for slip rate and the state of the sliding surface, respectively, such that when V =

V_o and $\theta = \theta_o$ the friction coefficient is μ_o; θ abstractly represents the average age of contacts at some sliding velocity; and σ^{eff} is the effective normal stress.

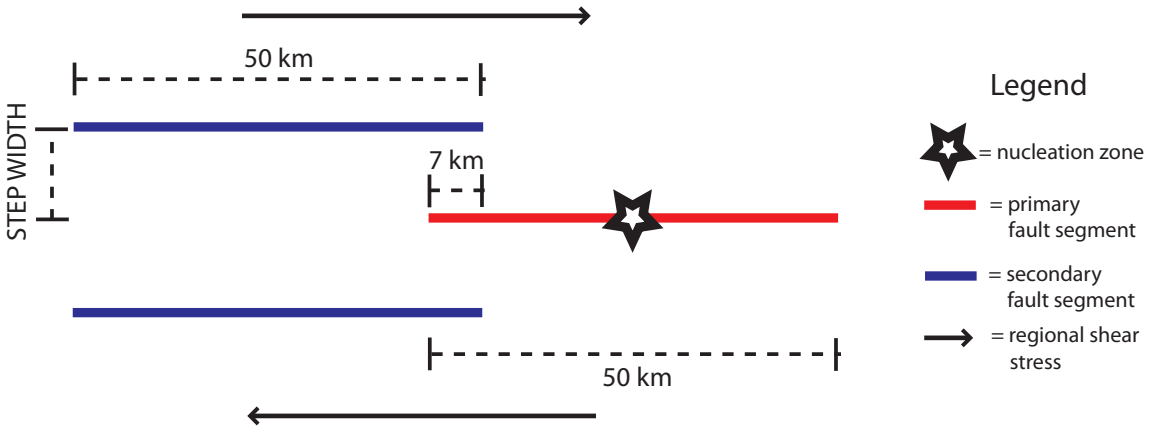

Figure 1.1. Cartoon fault geometry of 2-D models using dynamic finite element code FaultMod (Barall, 2008, 2009). Arrows denote the regional stress field. Note that the position of the secondary fault segment signifies whether the system is compressional (top) or dilational (bottom). The star denotes the nucleation zone. Fault segment length and overlap are fixed. Stepover width is variable. For any given simulation, only one secondary (blue) fault is present.

Following Barall (2009), we use a modified form of the bracketed term in eq. 1.6 that does not become singular for very small slip velocities:

$$\mu = \arcsin h\left[\frac{V}{2V_o}\exp\left(\frac{\mu_o + \psi}{a}\right)\right] \approx \mu_o + a\ln\left(\frac{V}{V_o}\right) + \psi \qquad (1.7)$$

This form of the RS law closely approximates eq. 1.6 for slip velocities of seismological interest. Note that the right hand side of eq. 1.7 has the form of the effective friction coefficient in eq. 1.6 with $\psi = b\ln(\theta/\theta_o)$, or conversely, $\theta = \theta_o\exp(\psi/b)$. Conceptually, ψ represents the strength of contacts.

1.1 Low Stress Models

τ_o	15.00 MPa
σ_o	24.00 MPa
τ_o (nucleation zone)	20.00 MPa
Density	2670 kg/m^3
S-wave speed	3464 m/s
P-wave speed	6000 m/s
Nucleation Radius	3000 m
Nucleation Speed	1750 m/s
Element Size	100.0 m
V_{ini}	1.000e-12 m/s
V_o	1.000e-6 m/s
a	0.008000
b	0.01200
L (ageing law)	0.02330 m
L (slip law)	0.1505 m
μ_o	0.6000
μ_{lv}	0.6000
μ_w	0.3000
V_w	0.1000 m/s
μ_{static}	0.8299
$\mu_{dynamic}$	0.5487
d_o	$\approx$ 0.3 – 0.6 m

1.2 High Stress Models

τ_o	75.00 MPa
σ_o	120.0 MPa
τ_o (nucleation zone)	100.0 MPa
Density	2670 kg/m^3
S-wave speed	3464 m/s
P-wave speed	6000 m/s
Nucleation Radius	600.0 m
Nucleation Speed	1750 m/s
Element Size	50.00 m
V_{ini}	1.000e-12 m/s
V_o	1.000e-6 m/s
a	0.008000
b	0.01200
L (ageing law)	0.02015 m
L (slip law)	0.1000 m
μ_o	0.6000
μ_{lv}	0.6000
μ_w	0.3000
V_w	0.1000 m/s
μ_{static}	0.8465
$\mu_{dynamic}$	0.5340
d_o	$\approx$ 0.2 – 0.6 m

Tables 1.1-1.2. A list of stress values, material properties, model properties, and friction parameters used for low and high stress models.

For the RS-AL, the state variable evolves according to the equation:

$$\frac{d\theta}{dt} = \frac{-1}{\theta_{ss}}\left(\theta - \theta_{ss}\right) \tag{1.8}$$

or equivalently,

$$\frac{d\psi}{dt} = \frac{-bV_o}{L}\left(\exp\left(\frac{-\psi_{ss}}{V}\right) - \exp\left(\frac{-\psi}{b}\right)\right) \tag{1.9a}$$

In the RS-SL, the state variable evolves according to the equation:

$$\frac{d\psi}{dt} = \frac{-V}{L}\left(\psi - \psi_{ss}\right) \tag{1.9b}$$

Both the RS-AL (eq. 1.9a) and the RS-SL (eq. 1.9b) reduce to the standard formula for steady-state sliding:

$$\psi_{ss} = -b\ln\left(\frac{V}{V_o}\right) \tag{1.9c}$$

RS-SRW, notably different from the RS-SL, incorporates the following steady-state equations (e.g., Rice, 1999, 2006; Beeler and Tullis, 2003; Rojas et al., 2009):

$$\psi_{ss} = a\ln\left(\frac{2V_o}{V}\sinh\left(\frac{\mu_{ss}(V)}{a}\right)\right) \tag{1.10a}$$

$$\mu_{ss}(V) = \mu_w + \left(\mu_{lv}(V) - \mu_w\right)\left(1 + \left(\frac{V}{V_w}\right)^{1/8}\right)^{-1/8} \tag{1.10b}$$

$$\mu_{lv}(V) = \mu_s - (b-a)\ln\left(\frac{V}{V_o}\right) \tag{1.10c}$$

where μ_s is the strong friction coefficient, μ_w is the weak friction coefficient, and V_w is the velocity around which the weakening (of frictional strength) occurs.

Slip occurs when the Coulomb stress criterion $|\tau + \Delta\tau| > \mu^*|(\sigma + \Delta\sigma)|$ is satisfied, although general μ evolves differently with respect to each friction formulation used in this study. In order to make a comparison among linear SW friction and RS formulations, we must define d_o for our RS formulations. In this way we may use common d_o values and thus isolate the effects of the formulation itself. For our RS laws, we estimate d_o as the distance over which approximately 98% of the total stress drop occurs. Because d_o depends on constitutive parameters in the RS formulation for each law (for a given stress regime), namely, L, we use specific L values for each RS formulation to form a common effective slip-weakening distance. Figure 1.2 shows a simplified energy budget schematic for earthquakes, and how it is related to the functional form of friction laws. Radiated energy density can be thought of as an average for all points along the fault. We strongly note that radiated energy density should be thought of as an average over the entire fault; radiated energy density from a single point cannot be determined easily from stress-versus-slip weakening curves since large portions of the fault are slipping simultaneously, and have complex stress wave interactions. However, fracture energy is dissipated for single points along the fault making it easily measurable from models. Note that all our models have fracture energy that is approximately constant for all ruptured points (i.e., all points have approximately the same d_o) under our homogeneous initial conditions, but unless otherwise noted, the fracture energies are not necessarily the same between the different friction parameterizations (even with equivalent d_o). We illustrate the method of effective slip-weakening distance equalization by plotting the stress as a function of slip for all friction formulations in our

low stress and high stress models in figure 1.3. Note that with equivalent d_o, the fracture energies for these parameterizations (the area underneath the weakening curves) are quite different. Figure 1.4 shows the same friction formulations, instead, with equivalent fracture energy. Thus, the areas under the weakening curves up to d_o are approximately equal (< 3% difference).

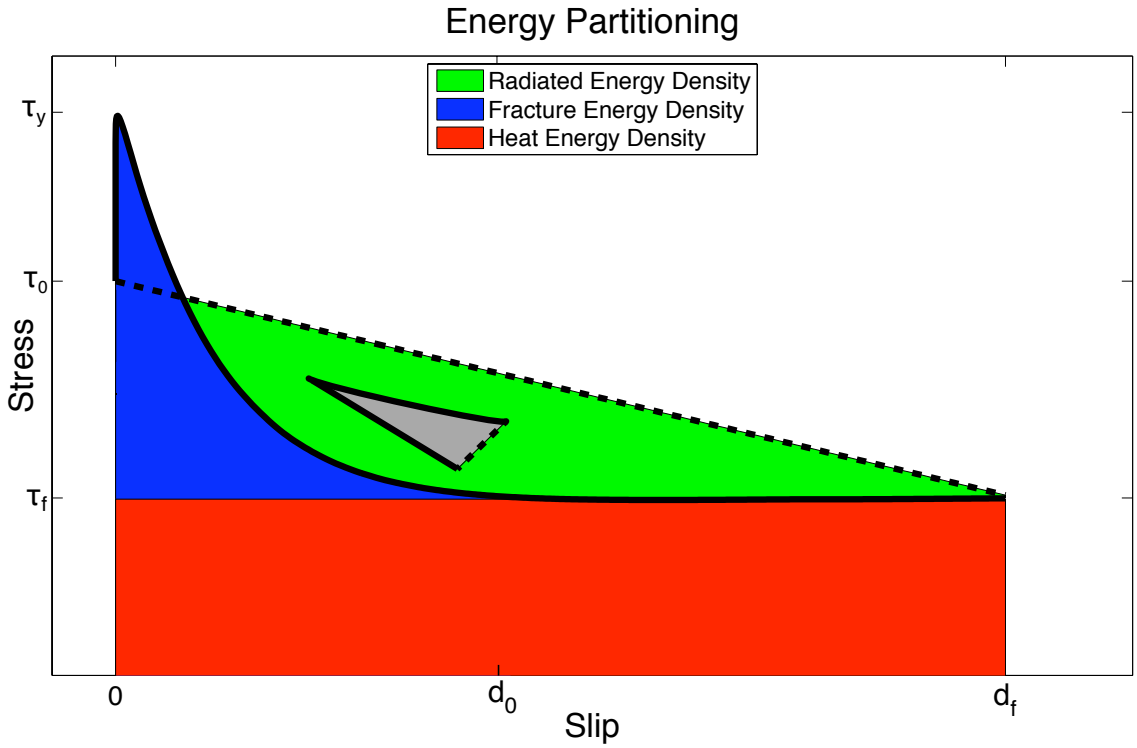

Figure 1.2. A simplified schematic of energy partitioning for an earthquake. The gray triangle within the radiated energy density indicates the full subtraction of the fracture energy density. Note that the figure shows a non-linear weakening curve for generality. Different friction laws produce different weakening curve geometries.

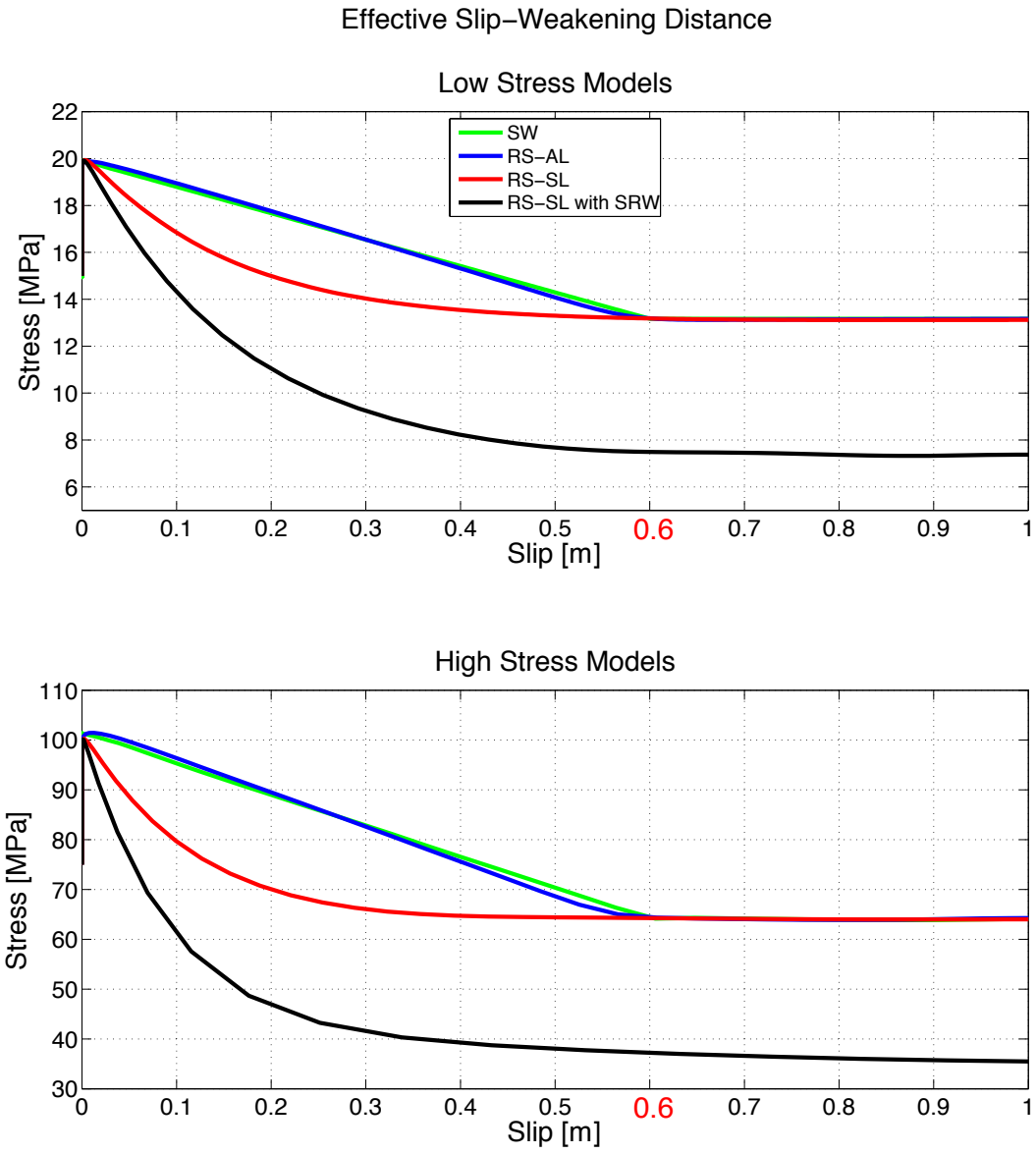

Figure 1.3. Effective slip-weakening distance curves for both low and high stress models are shown in the top and bottom panels, respectively. In order to make a valid comparison of all friction parameterizations used in this study, we tune each friction formulation to have the same effective slip-weakening distance. For the ageing and slip law formulations, we measure the effective slip-weakening distance as the distance over which the stress drop is 98% complete for a point on a fault segment. The slip law with strong rate-weakening has the same L (length parameter in the rate-state framework) value as the slip law. We measure d_o to be approximately 0.6 m for all models. Although this criterion is subjective, it provides a common basis for all models. Note the associated fracture energy density (i.e., the area under the weakening curve) varies among friction parameterizations.

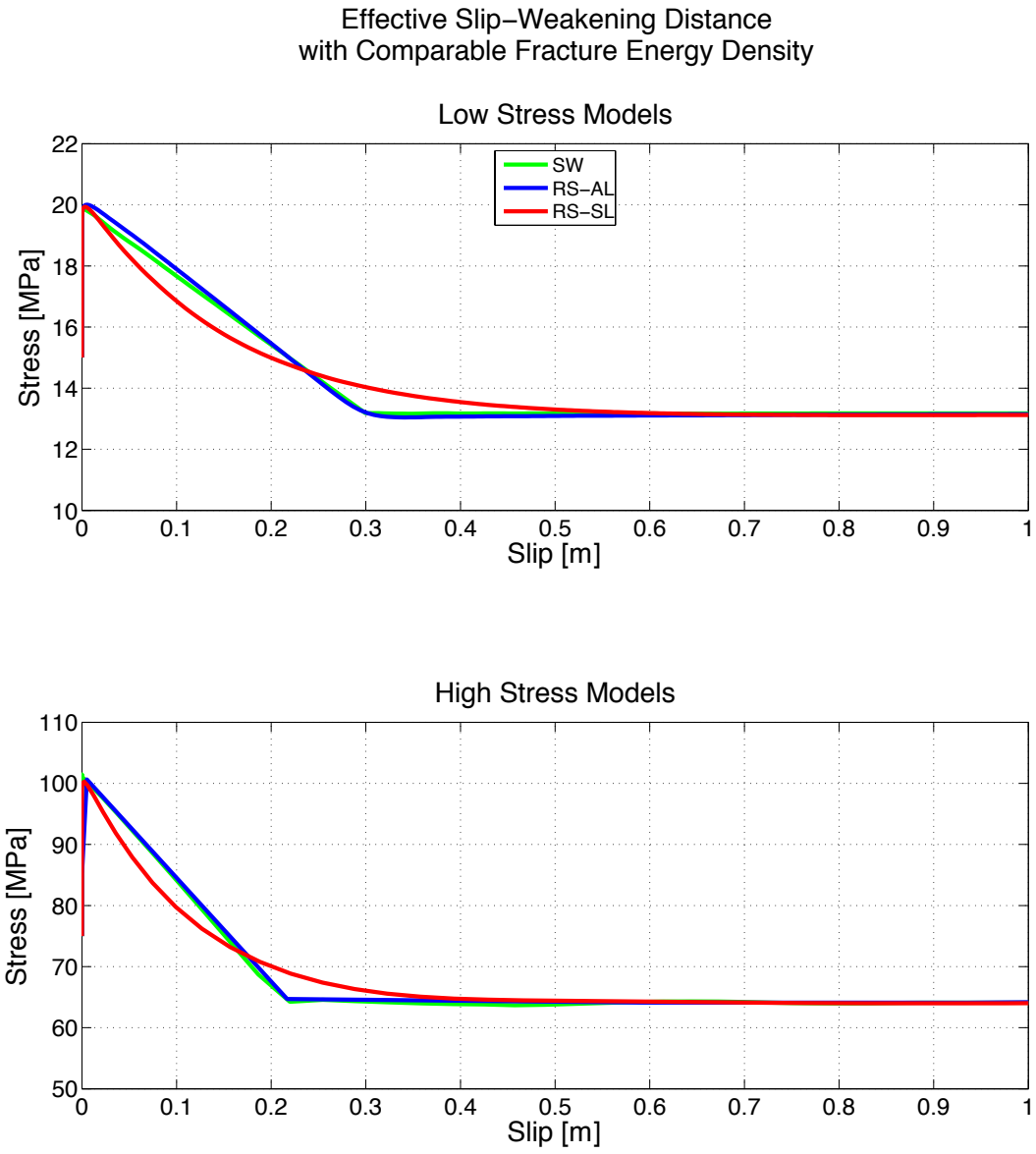

Figure 1.4. Effective slip-weakening distance curves for both low and high stress models are shown in the top and bottom panels, respectively, with comparable fracture energy densities. In order to equate fracture energy densities among friction parameterizations used in this study, the associated effective slip-weakening distances cannot always equate. Note that linear slip-weakening friction and the rate-state ageing law have similar functional forms, and therefore can have similar effective slip-weakening distances and fracture energy densities.

Fault length controls the slip duration in our (2-D) study, so stopping phases that penetrate inward from the along-strike edges control rupture duration. Therefore, our models represent a seismogenic zone of roughly 25 km (Harris and Day, 1993). We choose a Poisson ratio of 0.25, so that $\alpha = \sqrt{3}\beta$ where α is the P-wave velocity and β is the S-wave velocity. In order to accurately resolve the rupture process, FEM discretization must be able to resolve: (1) the time it takes a P-wave to traverse the smallest element size, (2) state-variable evolution (for RS simulations), (3) discretization in the cohesive zone (Palmer and Rice, 1973). To check for this, we adapt equation (A3b) from Bizzarri and Cocco (2003):

$$\Delta x << \frac{V_{rupt}}{V_{ave}} d_o \tag{1.11}$$

and the general condition (e.g., Andrews, 1985):

$$\Delta x \geq V_p \Delta t \tag{1.12}$$

where Δx is the smallest element size, Δt is one time step, and V_{ave} is the average velocity of a node from the time it reaches yield stress to sliding stress. Additionally we check that the number of elements within the cohesive zone for each model is 4 or more, which we consider the minimum for resolution of the process. Note that cases with the lowest number of elements in the cohesive zone involve RS-SRW models. In order for eqs. 1.11 and 1.12 to be satisfied, our high stress models have 50 m mesh increments along the fault, while our low stress models have 100 m mesh increments along the fault. Within each stress system, we use the same grid increments in all friction laws for comparability. Additionally, a reliable way to determine that our models have the correct resolution is to

compare rupture fronts at various times (Harris et al., 2009). Therefore we have run test models of RS-SRW at 50 m elements for our low stress case and 25 m elements for our high stress case. We find the percent difference of rupture velocity between the larger increments and smaller increments to be less than 3% at 20 km away from the nucleation center. Also, it has been shown that for mode II ruptures, there are similar mesh convergent rates for the RS-SL and RS-AL using a finite difference method (Rojas et al., 2009).

Rupture is artificially nucleated by an expanding zone of increased shear stress in the middle of the primary fault segment (see figure 1.1) within a nucleation half-width r_n, 3 km for low stress models and 0.6 km for high stress models; rupture is subsequently allowed to propagate spontaneously according to the friction formulation. The nucleation zone in both low and high stress models is large enough to limit discretization effects, and is proportional to $(\mu d_o)/(\tau_y - \tau_o)$, where μ is the shear modulus. Thus, the low stress models have an r_n that is 5 times the size of the high stress models. Although this study does not focus on details within the nucleation process, we try to limit the size of the nucleation zones in order to limit the effects of artificial nucleation on the rupture process. Further work is required to see how the size of the nucleation zone can affect rupture properties along fault stepovers.

Results

Comparing Different Friction Parameterizations with equivalent d_o

A main purpose of this study is to directly compare several different friction parameterizations on earthquake rupture at stepovers. One way to make a comparison between otherwise equivalent models is by equating the effective slip-weakening distance d_o for each friction formulation as described above. Under the assumption of equivalent d_o, we find significant differences in rupture properties among the friction laws within the stepover region. We find that for the same d_o, the RS-SL allows rupture to jump larger stepover widths than equivalent RS-AL models or linear SW models, for both compressional and dilational stepover systems (figure 1.5). The RS-AL and linear SW models are very similar with regard to maximum jumping distance due to the fact that their weakening curves have very similar functional forms. However, the RS-SL, which has a more concave-up weakening curve, and smaller fracture energy when compared to RS-AL and linear slip-weakening models. Thus, it allows more seismic wave energy release along the primary segment and requires a smaller critical patch size to initiate rupture along the secondary fault segment. Hence, secondary nucleation along the secondary fault segment can more easily occur when using the RS-SL, according to our criteria. Strong rate-weakening (RS-SRW) models are able to jump very large stepovers widths (> 7 km) because of their larger stress drop, and the corresponding large seismic wave energy. Overall, high stress models show less difference in maximum jumping distance between the SW, RS-AL, and RS-SL simulations than the low stress models (figure 1.5). We attribute this effect to a shrinking ratio of fracture energy to the total

potential energy of an earthquake with increasing slip. Figure 1.6 illustrates this effect. We use the same d_o for all models discussed above, and the ratio of fracture energy to seismic wave energy approximately scales with the ratio of d_o to the total slip, assuming the yield shear stress is close to the initial shear stress. The total slip for the high stress models, however, is much larger than the low stress models. In other words, the ratio of seismic radiation energy to fracture energy increases for our high stress models, resulting in the different friction formulations producing similar effects on the rupture dynamics (i.e., maximum jump distance) even though they have different functional forms. We acknowledge that for the RS-AL, SW, and RS-SRW models with a low stress regime, compressional steps have larger maximum jump distances than dilational steps, which is different from some previous studies (e.g., Harris and Day, 1993), possibly due to different stress regimes.

Comparing Different Friction Parameterizations with equivalent Fracture Energy

We note that there are other ways to compare the different friction laws (e.g., by equating their effective slip-weakening distance). With equivalent d_o, we attribute differences in maximum rupture jump distances to both the functional form of the friction laws, and to the associated energy budget. In order to test the effect of the functional form separately from that of the fracture energy, we modeled earthquake ruptures with fracture energy using RS-AL, RS-SL, and SW friction (figure 1.4). Note that we do not consider the strong rate-weakening formulation here since it is a specialized version of the slip law

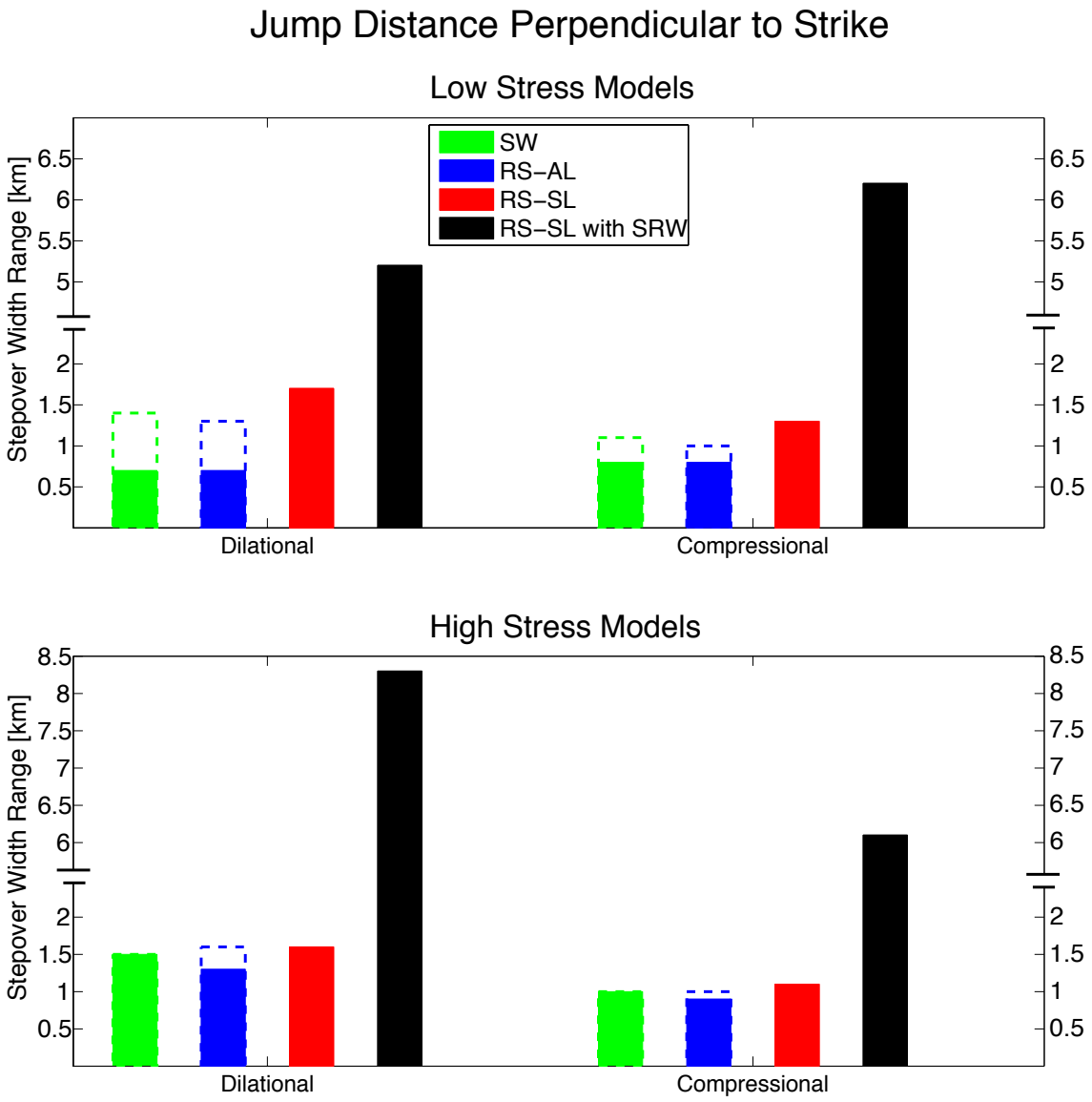

Figure 1.5. Maximum jump distances for both low and high stress models are shown in the top and bottom panels, respectively. For each friction formulation, the maximum rupture-jump distance perpendicular to strike is shown. Models with equivalent slip weakening distances have maximum jump distances indicated by solid regions (excluding the strong rate-weakening models). Models with equivalent fracture energy density have maximum jump distances indicated by dashed regions. Dashed regions are never lower than solid regions. Note that the y-axis is broken due to the relatively large jump distance for RS-SL models incorporating strong rate-weakening friction.

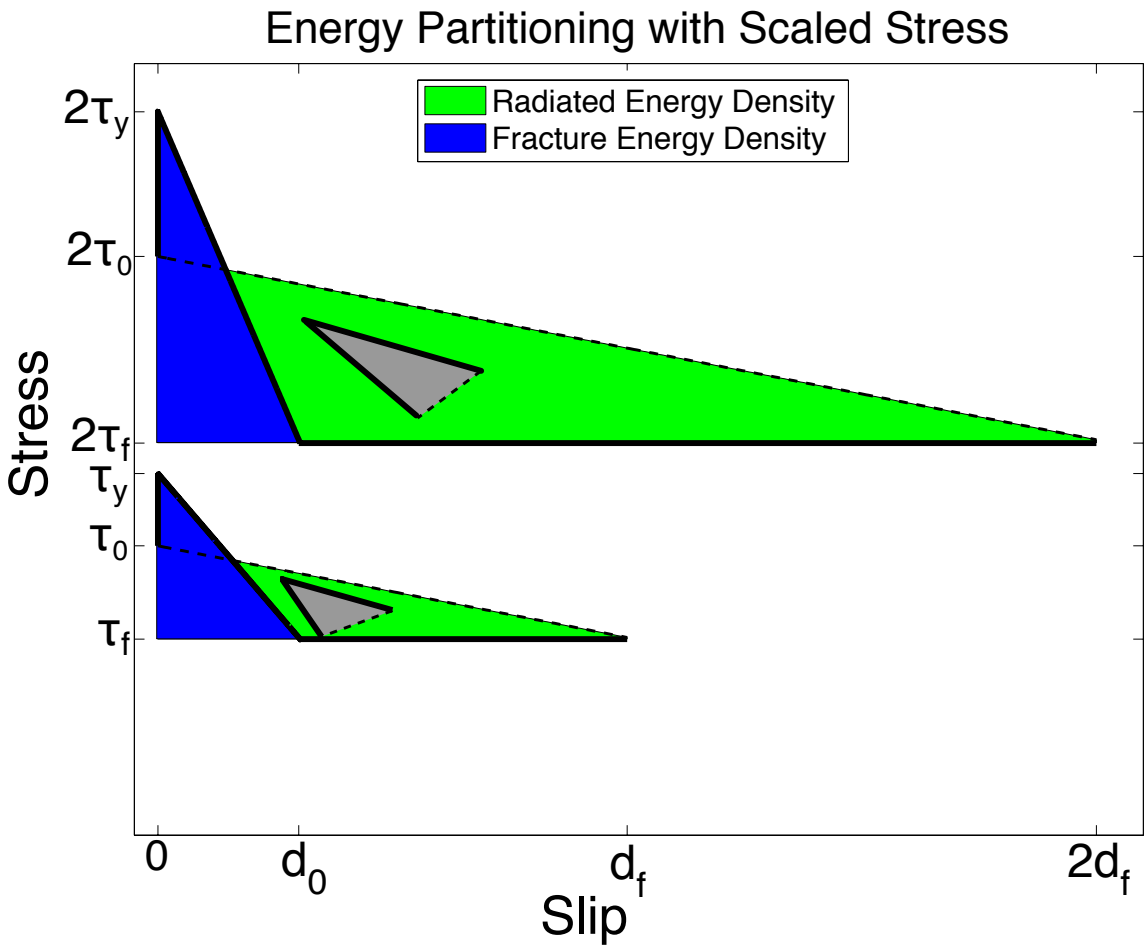

Figure 1.6. Linear slip-weakening curves scaled up by stress, while holding the effective slip-weakening distance as well as frictional coefficients constant, result in a larger ratio of seismic radiation density to fracture energy density.

and has a vastly different energy budget. With all fracture energies scaled to the fracture energy of the prior RS-SL models (a value of d_0 = 0.6 m is used in equation 1.1 to determine the fracture energy for RS-SL models), the difference in maximum rupture-jumping distance between the SW and RS-AL vs. the RS-SL simulations is substantially smaller (figure 1.5). Thus, the fracture energy associated with each friction law has a first order effect on maximum jump distance, especially for the low stress cases. Due to

our grid resolution, a difference in maximum jump width of 50 m and 100 m is not significant for our high and low stress models, respectively. The high stress models indicate that maximum rupture jump distance can be very similar, regardless of the friction law used, with the exception of RS-SRW models. Even though the primary effect on maximum jump distance appears to come from the fracture energy, the functional form for each friction law still affects maximum jump distance, although this effect is not as strong. This result is consistent with numerical studies (Dunham 2007), which have shown that the slope of the slip-weakening curve can determine the critical nucleation size (i.e., steeper slopes like that of the RS-SL require smaller nucleation zones for rupture to propagate outside the nucleation zone). Further studies are needed to fully examine the variation between different friction laws, especially with more complex energy budgets that include off-fault damage zones or variable fracture energy along strike.

Stepovers as a Mechanism for Supershear Transition

For the high stress models in this study, we find a supershear transition in the stepover region along the secondary fault segment for certain parameterizations. The supershear transition occurs at and above certain minimum stepover widths in both extensional and compressional settings. The transition of rupture to supershear speed might seem somewhat surprising, given that our initial conditions in principle preclude our models from a supershear transition according to the standard Burridge-Andrews mechanism. The seismic S ratio is set to 2.6 for these models, larger than 1.77 – the value at which the

supershear transition does not occur for single-fault 2-D models. Thus, this supershear transition mechanism is a previously-unobserved one that is related to the fault geometry and rupture-jumping process. Dynamic waves from rupture on the primary fault segment alter the stress field along the secondary fault segment before it ruptures, increasing the shear stress and reducing the normal stress, and thereby priming the secondary fault segment for supershear rupture. The supershear transition occurs preferentially along compressional and dilational regimes after a delay in rupture at the stepover for the RS-AL, RS-SL, and linear SW friction formulations. RS-SL models with strong rate-weakening produce supershear rupture because they have a lower seismic S ratio (due to their larger stress drop). Models that show a supershear rupture transition from the primary fault segment to the secondary fault segment show a longer time delay from the end of the primary rupture to the start of the secondary rupture than do models that do not show supershear rupture. Models that have longer delays have larger stepover widths. Therefore in order for the supershear transition to occur, there is a corresponding minimum stepover width. For compressional regimes, the minimum stepover widths required for sustained supershear rupture on the secondary fault are 0.6 km, 0.6 km, and 0.7 km for linear SW friction, RS ageing law, and RS slip law, respectively, with equivalent d_o. All step widths above the minimum sustain supershear rupture for the entire length of the secondary fault segment (unless rupture cannot jump to the secondary fault segment). However, the appearance of supershear rupture in dilational regimes seems to be less systematic, and although they too have minimum step widths required for the supershear transition, there is no discernible pattern (i.e., not all step widths above

the minimum necessarily sustain supershear rupture speed). Ultimately, this effect probably depends on the variability of the seismic S ratio and L_{trans} along strike near the re-nucleation zone. We emphasize that for both compressional and dilational settings, re-nucleation occurs at zones of decreased normal stress, as shown in figure 1.7.

We find that the ability of rupture to make the transition to supershear speed on the secondary fault is related to the spatial distribution of the seismic S value in the region of re-nucleation. Plots of the seismic S ratio right before rupture along the secondary fault segment are shown in figure 1.7. Figure 1.7a shows the case of a sample compressional regime with a 0.4 km stepover width using RS-AL; in this case, rupture does not sustain supershear speed. Figure 1.7b shows another sample case – a compressional regime with a 1 km stepover width – that rapidly transitions to (and sustains) supershear speed after re-nucleation on the secondary fault. For the Burridge-Andrews supershear transition mechanism to operate, the rupture must propagate a distance L_{trans} before the S wave stress ahead of the crack tip can instigate supershear rupture. The value for this distance at each point on the secondary fault is shown for each plot. For cases of sustained supershear rupture (figure 1.7b) on the secondary fault segment, S and L_{trans} values are small in the vicinity of the re-nucleation region. Thus, we see that to allow supershear rupture over the entire secondary fault, supershear S values (< 1.77) need only occur in small regions that contain the re-nucleation point (but larger than the critical crack length). Put another way, a supershear transition occurs if the value of the reduced L_{trans} is less than or equal to the width (along strike) of the zone of reduced L_{trans}. For example,

if L_{trans} is 1 km over a width of more than 1 km, then the transition to supershear occurs if self-sustaining slip occurs there. That is the case for figure 1.7b. Conversely, in Figure 1.7a (no supershear transition), while S is less than 1.77 around the nucleation zone, L_{trans} is still large, preventing a supershear transition over the length of the second fault. Once rupture begins to travel at supershear speed along the secondary fault segment, it satisfies $\sqrt{2}\beta < V_{rupt} < \alpha$ as predicted by Andrews (1976b).

Figure 1.7c shows a typical supershear transition for a compressional regime with a 0.7 km step. We see larger velocity parallel to the fault once the rupture reaches supershear speed. Note that there is a substantial delay (≈15 seconds) from rupture ending on the primary segment to rupture beginning on the secondary segment. Once re-nucleation occurs, supershear rupture propagates immediately. We point out the P-wave front, the supershear (S-S) Mach cone, and the sub-Rayleigh (S-R) slip pulse at 38.8 seconds. A single strike-slip fault model 100 km in length (approximately the total length of both fault segments of the stepover models) with a high stress regime does not show the supershear rupture transition, confirming that the transition is not a result of directivity.

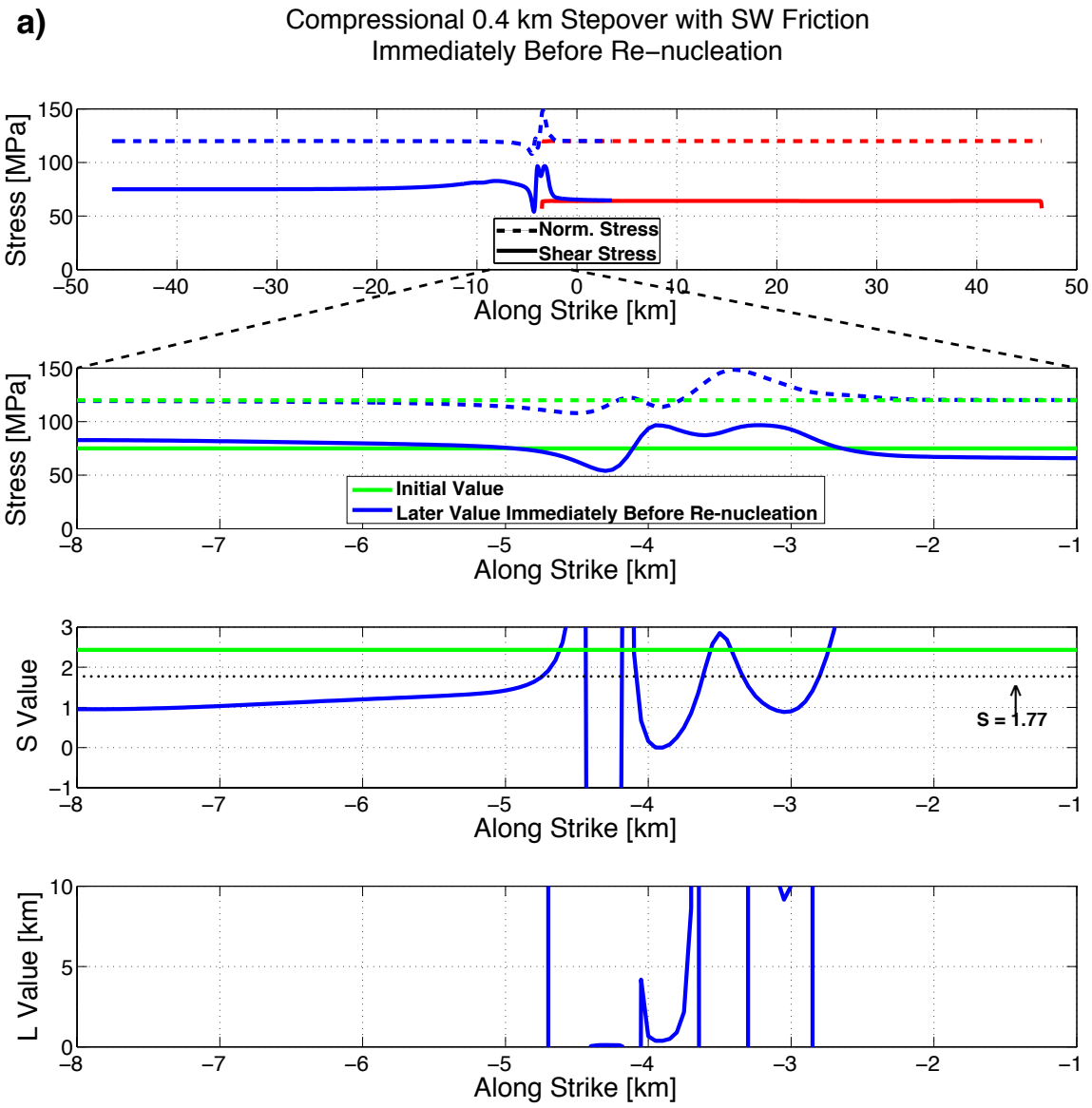

Figure 1.7a. Top panel: Stress snapshots right before the time of re-nucleation on the secondary fault segment for a compressional 0.4 km step using slip-weakening friction. Bottom panels: S ratio and L_{trans} at -8 km to -1 km. Re-nucleation occurs at -3.9 km along strike. S and L_{trans} values are not low enough along an extended section of fault to create sustained supershear rupture on the secondary fault.

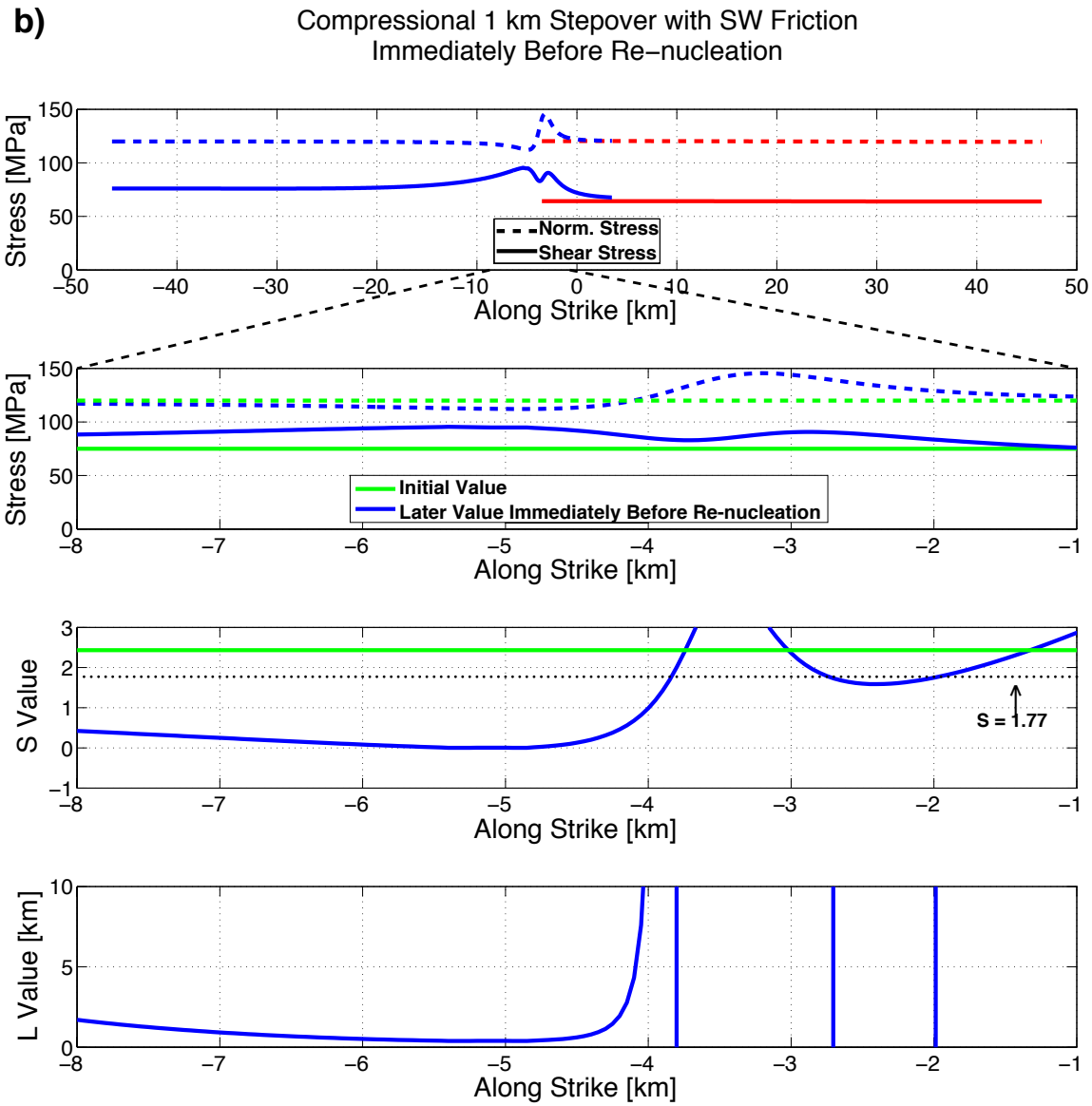

Figure 1.7b. Top panel: Stress snapshots right before the time of re-nucleation on the secondary fault segment for a compressional 1 km step using slip-weakening friction. Bottom panels: S ratio and L_{trans} at -8 km to -1 km. Re-nucleation/supershear propagation begins at -5 km along strike. S and L_{trans} values are low enough along an extended section of fault to create sustained supershear rupture on the secondary fault.

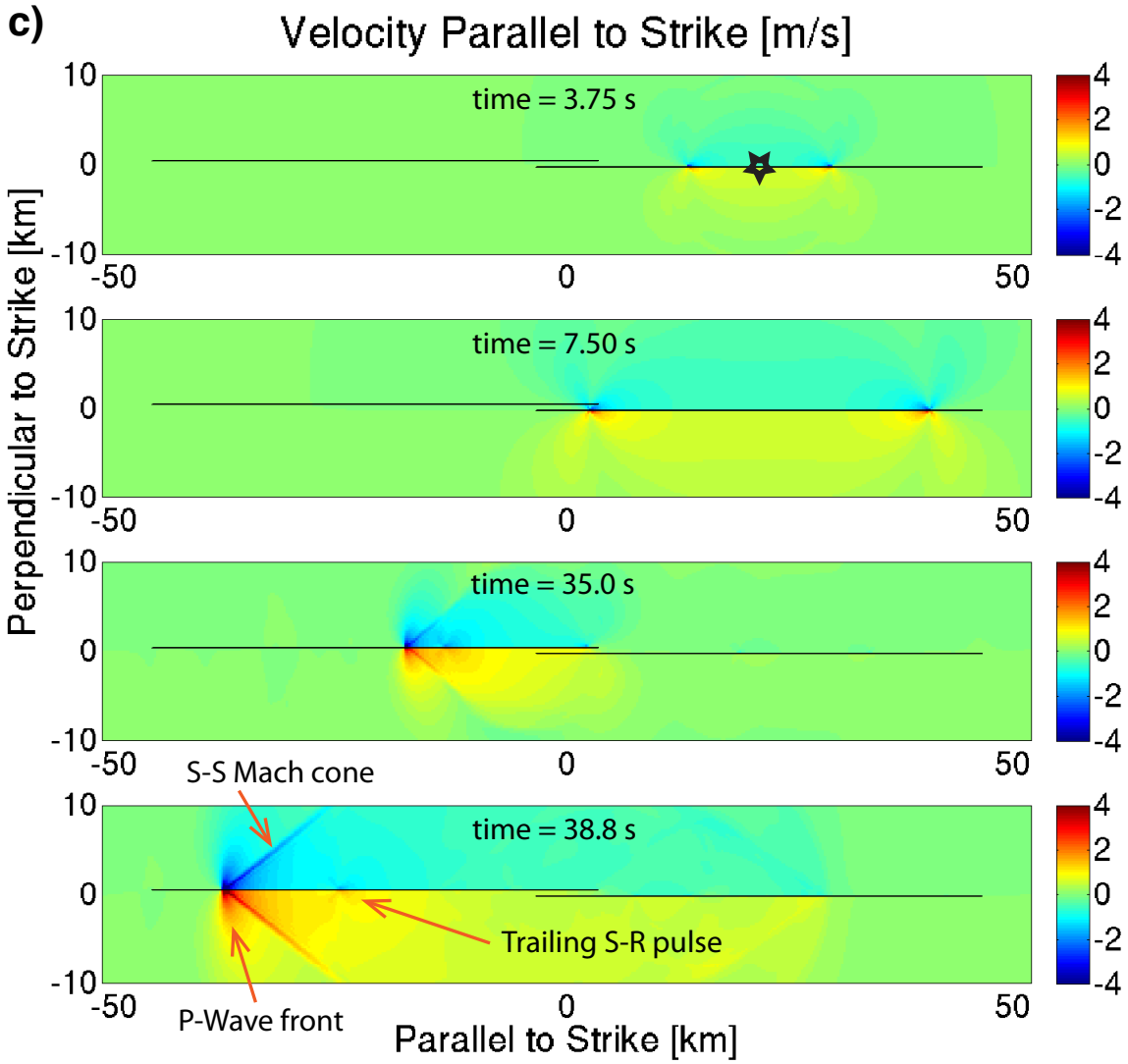

Figure 1.7c. Velocity parallel to strike for a characteristic supershear transition on a compressional 0.7 km step using the ageing law. The nucleation zone is denoted by the black star. Velocity increases substantially on the secondary fault segment. There is a delay (about 15 seconds) in rupture ending on the first segment and rupture beginning on the second segment. Additionally, at 38.8 seconds we label the supershear (S-S) Mach cone, the P-wave front, and the sub-Rayleigh (S-R) slip pulse that trails the supershear rupture.

Discussion

This study focuses on the effects of various friction laws on rupture propagation along strike-slip stepovers. Within our friction framework, we use a value of effective slip-weakening distance d_o of about 0.6 m to institute some uniformity to all friction formulations, consistent with recent studies that show values on the order of 1 m (Ide and Takeo, 1997; Oslen et al. 1997). Our results indicate that the functional form of friction can give significant effects on the rupture dynamics at stepovers. When we assume a constant d_o for all friction parameterizations, we see that differences in the energy budgets (in particular, the surface energy relative to the total energy release) correlate to differences in maximum jump distance. In these cases the rate-state slip law has a smaller fracture energy density than either the rate-state ageing law or the slip-weakening law, and produces more seismic radiation that allows rupture to jump further. Those differences in maximum jump distance are decreased substantially when we equate fracture energy densities for the friction laws, but the larger initial stress-slip slope of the slip law still causes it to produce slightly larger maximum jump distances. One way to decrease the differences further may be to increase the initial shear stress for models using the classic slip-weakening friction and the ageing law, so that they have the same average amount of seismic radiation as the slip law. High stress models show more similar maximum jump distances between different friction formulations than low stress models, for either equal d_o or equal fracture energy. This implies that the type of friction law can become less important for modeling jumping rupture with high absolute stresses. We also point out that the ageing law produces approximately linear weakening curves,

similar to that of slip-weakening friction, making it easier to tune slip-weakening friction to mimic the ageing than to mimic the slip law. However, one very important aspect of rate-state friction, in particular the ageing law, is the intuitive healing process (e.g. frictional strength increases with contact time) that cannot be mimicked by slip-weakening friction. Thus, even if the short-term stepover jumping behavior of the slip-weakening and rate-state ageing laws is very similar, the long-term behavior of faults under these different frictional assumptions may be quite different.

Our results show that the likelihood that rupture can jump a certain fault stepover is dependent upon the friction parameterization employed. Observations of jumping rupture could potentially provide insight into which friction law is more valid. For example, for a known stress drop, jump distance, fault geometry, and slip distribution in time, one could provide a simple model with a preferred friction law. Adopted evolution laws can influence probabilities of jumping rupture at stepovers and affect the predicted magnitude of simulated earthquakes. Such effects may be critically important for smaller step widths, especially if portions of the fault undergo strong rate-weakening. Earthquakes with high slip rates would be especially susceptible to non-linear weakening curves and large dynamic drops in friction coefficient, with a consequent higher likelihood of jumping stepovers. High-speed laboratory studies that show such nonlinear weakening curves are certainly a good reason to explore strong rate-weakening properties in dynamic simulations of real world faults. In light of our general results, dynamic simulations based on real fault steps can produce variable results depending of the

friction law used (as well as stress regime and material properties). We have also seen that in high stress regimes, the maximum jump distance tends to converge to a maximum jump value for the 3 different friction laws (excluding the slip law with strong rate-weakening), suggesting that is probably not as crucial to consider effects from different friction laws in high stress drop, high seismic radiation, homogeneous models. However, it is not obvious under which circumstances the effects of friction law might be accentuated (e.g., heterogeneous prestress).

For the high stress regime, we show that fault stepovers can serve as a trigger for a previously undocumented mode of supershear transition, even though the initial seismic S ratio (2.6) along the fault is too large for the transition to occur on a planar strike-slip fault. Seismic waves from the primary fault segment alter the stress field along the re-nucleation zone of the secondary segment before rupture initiates, bringing the seismic S ratio to a value that allows supershear rupture speeds in this area. Once the rupture reaches supershear speed, it can remain supershear even outside the area of favorable stress. Other numerical studies have indicated supershear transition mechanisms along strike-slip faults, including zones of high frictional resistance (Dunham, 2003) and zones of favorable prestress (Fukuyama and Olsen, 2002; Liu and Lapusta, 2008), and changes in fault strike (Oglesby et al., 2008; Oglesby and Mai, 2011). Laboratory experiments on homalite with a frictional interface (Xia et al., 2004) show the sub-Rayleigh to supershear transition. However, their initial stress configuration allows supershear speed under the Burridge-Andrews mechanism. Observational evidence for supershear rupture speeds

suggests strong fault-parallel ground motion when compared to sub-Rayleigh ruptures (e.g., Archuleta, 1984; Dunham and Archuleta, 2004), and we see such motion in our supershear models along the S-wave Mach cone.

We acknowledge some limitations in this study so that future studies can expand on the current results. All models are 2-D, indicating that rupture energy is concentrated along a plane, and therefore produce larger average slip, slip rates, and stress drops than analogous 3-D models. The models produced for this study are primarily crack-like (i.e., slip pulses are spatially large and fall off asymptotically), likely due to large loading stress (initial shear stress) (Zheng and Rice, 1998). We use spatially homogeneous frictional properties and assume that RS friction operates at high slip rates even though it is laboratory-derived at low slip rates, suggesting that our models do not entirely account for large scale asperities and slip rates. Additionally, the stress regime on the secondary fault is changed by stopping phases – seismic radiation produced by rapid rupture termination along the primary fault (Madariaga, 1976) that can cause rupture to re-nucleate on the secondary fault segment. Stopping phases in our models result from clamping the ends of each fault segment over one element with a high frictional coefficient. Oglesby (2008) shows that slip gradient and rupture acceleration can strongly affect maximum jump distance by modulating stopping phase amplitude. In particular, as the stress and slip gradients decrease at the edge of the primary fault the ability of rupture to jump also decreases. However, both high and low slip gradients have been observed at stepovers (Elliot et al., 2009).

Future work (chapter 2) will incorporate state-variable dependence on normal stress (Linker and Dieterich, 1992) in order to produce more realistic ruptures. Including a normal-stress dependent state variable within the RS framework could emphasize or de-emphasize normal stress asymmetries between compressional and dilational steps. Such a friction parameterization will likely alter the energy budget in regions that have large perturbations in normal stress.

Chapter 2: Effects of Normal-Stress-Dependent State at Stepovers & Dip-Slip Faults

Abstract

Previously we have demonstrated that the maximum rupture jump distance along stepovers can vary depending on the frictional parameterization used, with the primary factor being amount of fracture energy associated with a certain effective slip weakening distance. The development of the rate- and state-dependent friction framework (Dieterich, 1978b, 1979; Ruina, 1983) includes the dependence of friction coefficient on normal stress (Linker and Dieterich, 1992), however, a direct dependence of the friction law on time-varying normal stress in dynamic models has not yet been extensively explored. Using rate- and state-dependent friction laws and a dynamic finite element code (Barall, 2008) we investigate the effect of the Linker-Dieterich dependence of state variable on normal stress at stepovers and dip-slip faults, where normal stress should not be constant with time (e.g., Harris and Day, 1993; Nielsen, 1998). Specifically, we use the relation $d\psi/dt = -(\alpha/\sigma)(d\sigma/dt)$ from Linker and Dieterich (1992), in which a change in normal stress leads to a change in state variable of the opposite sign. We investigate a range of values for alpha, which scales the impact of the normal stress change on state, from 0 to 0.5 (laboratory values range from 0.2 to 0.56). For stepovers, we find that adding normal-stress dependence to the state variable delays or stops re-nucleation on the secondary fault segment when compared to normal-stress-independent state evolution. This inhibition of jumping rupture is due to the fact that re-nucleation along the secondary segment occurs in areas of decreased normal stress in both compressional and dilational stepovers. A decrease in normal stress results in an increase in state variable

(and thus fault strength) in those same areas, thereby hindering rupture in both cases. However, the magnitude of such an effect differs between dilational and compressional systems. Additionally, it is well known that the asymmetric geometry of reverse and normal faults can lead to greater slip and a greater peak slip rate on reverse faults than on normal faults, given the same initial conditions for each (e.g., Nielsen, 1998; Oglesby et al., 1998; Oglesby and Archuleta, 2000a, Oglesby et al., 2000b). For dip-slip models, we find that adding the Linker-Dieterich normal stress dependence to the state variable serves to mitigate differences in peak slip rate between reverse and normal fault models. However, differences in total slip among reverse and normal fault models remain relatively unchanged. We also examine effects from initial shear stress (loading stress). Decreasing the initial shear stress of the dip-slip models results in reverse fault ruptures propagating further updip than normal ruptures. Models using slip-weakening friction do show very similar results with regard to loading stress, indicating that this is not an exclusive rate-state effect. For rate-state ageing law models, we add a small (5 km) rate-strengthening zone on the uppermost portion of a reverse and a normal fault model to study the effects of a rate-strengthening zone rupture. We find that the normal fault rupture does not allow a substantial stress drop within the rate-strengthening zone. However, the reverse fault rupture does produce a significant stress drop even in the rate-strengthening zone, due to the dynamic decrease in normal stress. One result of this effect may be a higher likelihood of reverse fault rupture propagating to the surface than a corresponding normal fault rupture.

Introduction

Modeling geometrically complex faults in order to simulate realistic earthquake ruptures is an ongoing challenge in seismology. For single planar fault geometries it can be shown that normal stress is constant in time. One example is a single strike-slip fault in a homogeneous elastic half space (or whole space). However, for faults with more complex or asymmetric geometry (e.g., stepovers and non-vertical dip-slip faults intersecting the free surface), the normal stress can change with time, leading to changes in the frictional strength, and thus changes in the time evolution of rupture and slip. To investigate the effects of this time-dependent normal stress, we focus firstly on fault stepovers, parallel fault segments of a single system that are horizontally separated by a small distance (mm to km) at their edges, and are found all over the world (Wesnousky, 1988; Knuepfer, 1989). For a given amount of slip on one fault, the normal stress change in the stepover region for a compressional stepover is the negative of that of an extensional one (e.g., Harris and Day, 1993). Stepovers can be considered a first order geometric complexity when it comes to modeling earthquake ruptures. Many researchers have used dynamic modeling to investigate the effects of fault geometry on rupture propagation and slip at a stepover. (e.g., Harris and Day, 1993; Kase and Kuge, 1998; Duan and Oglesby, 2006). These works have shown that termination of slip on the primary fault segment causes complex static and dynamic stress fields in the stepover region, which can result in rupture re-nucleating along the secondary fault and continuing, leading to a larger earthquake than otherwise might have been expected. For example, Harris et al. (1991) and Harris and Day (1993) show that dynamic differences in

normal and shear stress determine when and where re-nucleation takes place on the secondary fault, assuming a normal-stress independent friction coefficient. Kase and Kuge (1998) also note that rupture propagation on the primary fault triggers rupture on the secondary fault by altering the stress field in the medium along the fault system. Duan and Oglesby (2006) show that the dynamic stress field for a stepover system can vary with the rupture history (i.e., prior earthquakes) and therefore such effects can determine future rupture nucleation.

While single, planar strike-slip faults do not produce normal stress changes, strong normal stress perturbations are one similarity of stepovers and dip-slip faults. For stepovers these perturbations result from the stress interaction of two or more fault segments, whereas for dip-slip faults the normal stress fluctuations come from seismic wave reflections from the free surface (Brune, 1996; Nielsen, 1998; Oglesby et al., 1998; Oglesby and Archuleta, 2000a, Oglesby et al., 2000b). Specifically, for non-vertical dip-slip faults, the free surface allows seismic waves to reflect and hit the fault again, altering the stress field on the fault near the free surface. Oglesby et al. (1998) show that as rupture approaches the free surface along a normal fault, there is a decrease in normal stress ahead of the crack tip and an increase in normal stress behind the crack tip; this effect leads to reduced fault motion near the surface. In contrast, reverse faults produce a normal stress increase ahead of the crack tip, and a normal stress decrease behind, leading to increased fault motion near the surface. Furthermore, when rupture travels updip along a dip-slip fault and reaches the free surface, it produces a breakout phase, a slip pulse

traveling back downdip (Burridge and Halliday, 1971; Oglesby et al., 1998), with reverse/thrust faults having stronger breakout phases than normal faults. Numerical and experimental studies have seen asymmetric differences in slip velocity, total slip, and ground motion between reverse and normal faults, with reverse faults being larger on all accounts (Brune, 1996; Nielsen, 1998; Oglesby et a., 1998). Such effects have large implications for dynamic stress drop, which depends on both the time-dependent friction coefficient and time-dependent normal stress.

Experimental and observational evidence show that reverse/thrust faults produce more intense motion than that of normal faults. Brune's (1996) foam block models indicate enhanced slip for thrust models relative to normal models. Observationally, the 1994 Northridge, California and 1971 San Fernando, California earthquakes – both of which were thrust events – produced larger ground motion than expected (Nason, 1973; Abrahamson and Somerville, 1996). Allen and others (1998) also show evidence for high vertical acceleration and ground motion during the San Fernando earthquake. Cocco and Rovelli (1989) find evidence for larger dynamic stress drop and ground motion (3 times as much) for reverse earthquakes near Friuli, Italy against normal earthquakes in the Apennines region of Italy. McGarr (1984) shows that, when regression lines are fit to acceleration and velocity data from compressional and extensional tectonic regimes in North America, peak velocities and peak accelerations in compressional environments (e.g., thrust faults) are 2 to 3 times greater than for extensional environments (e.g., normal faults). We note that differing stress magnitudes

between compressional and extensional regimes could heavily influence some of these results.

Existing numerical studies have modeled earthquakes on stepovers and dip-slip faults using classic slip-weakening friction. However, experimental studies show that rate- and state-dependent (RS) friction is a more accurate approximation of real-world frictional behavior. Physically, the RS parameterization reproduces frictional behaviors measured in laboratory settings, such as stick-slip sliding, creep, and rate-strengthening (Dieterich, 1979; Marone et al., 1990). Theoretically, RS friction incorporates intuitive friction variables such as time and slip velocity (Dieterich, 1978b). Based on previous studies of RS friction (Dieterich, 1978b, 1979; Ruina, 1983), Linker and Dieterich (1992) have further developed laboratory-derived friction laws to account for their observation that the friction coefficient depends on normal stress history. Their physical experiment involves sliding blocks of Westerly granite while perturbing the blocks with changes in normal stress. They show that, at constant slip rate and an initial steady state, a sudden change in normal stress results in a change in the state variable in the opposite direction. The change in state with respect to normal stress is shown in the following equation (13) from Linker and Dieterich (1992):

$$\frac{\partial \theta}{\partial \sigma} = \frac{-\alpha \theta}{b \sigma} \tag{2.1}$$

where θ is the state variable, σ is the normal stress, α is experimentally determined, and b is a constitutive parameter determined previously by Dieterich (1979). Furthermore, they determine that ultimately θ evolves toward the steady state value prior to the normal

stress perturbation, since the steady state (and therefore friction coefficient) is not dependent on normal stress ($\theta_{ss} = L/V$). Linker and Dieterich (1992) determined values for alpha of 0.2 for the rate-state ageing law and 0.56 for the rate-state slip law for Westerly granite. If the state variable compensates for changes in normal stress based on the value of α, there could be complex and profound effects on models that have large fluctuations in normal stress, including stepover and dip-slip ruptures.

Simulating unstable and stable sliding zones (e.g., outer boundaries of seismogenic zones) with RS friction has been suggested (e.g., Scholz, 1998, Hyndman et al., 1998). In particular, the increase in the steady-state friction coefficient with slip rate can characterize the stable sliding zones that border the seismogenic zones. Within the RS formulation a positive rate-strengthening parameter (a – b), where a and b are experimentally determined previously by Dieterich (1978b, 1979) through observed stress drop, indicates velocity strengthening or stable slip, and a negative parameter indicates velocity weakening or unstable slip. For reverse/thrust faults it has been suggested that such rate-strengthening zones can simulate weak zones in the inner margin of the trenches, possibly characterized by large amounts of sedimentation. Kanamori (1972) noted that sediments in the trench could be a mechanism for tsunami earthquakes – earthquakes that produce relatively small ground shaking but larger than expected tsunamis. Granular material such as fault gouge tends to stabilize slip (Marone et al., 1990) and therefore might be the mechanism for rate-strengthening zones. Hyndman and others (1998) point out that rate-strengthening regions can be caused by unconsolidated

sediments updip and either temperature or hydrated serpentinite at depth, and that seismogenic zones typically lie between 10 km and 40 km depth. Experiments on ultrafine-grained quartz and corresponding regression analysis (Chester and Higgs, 1992) suggest that rate-weakening behavior occurs between 100^{o} and 300^{o} C under wet conditions, while higher temperatures lead to a rate-strengthening parameter (a – b) of 0.03.

The use of laboratory-derived friction laws can be a very helpful tool in analyzing rupture dynamics (Okubo, 1989). The objective of this study is to build upon the Linker and Dieterich (1992) framework by applying their friction law to both simple stepover and dip-slip fault models. Because both types of models involve dynamic perturbations in normal stress on the faults, it is important to incorporate a friction law that has realistic dependence on time-dependent normal stress. For stepover models we concentrate on the effect of frictional parameterization on maximum rupture jump distance for both compressional and dilational steps, since this will strongly influence potential earthquake size as well as estimates of ground motion. For dip-slip models we concentrate on particle motion, for both reverse and normal events, to characterize key differences between them and assess the relative hazards of such events.

Method

We use the 2-D finite element method (FEM) code FaultMod (Barall, 2008) to model mode II dynamic rupture along fault stepovers and dip-slip faults (figure 2.1).

Additionally, we use stress and friction regimes consistent with observed stress drops as well as average values for density and wave velocities within the mid crust (e.g., Harris and Day, 1997) (Tables 2.1-2.2). For stepover models each fault segment is 50 km in length, and the overlap between segments is 7 km. The overlap is large enough to allow rupture to re-nucleate on the secondary fault in both compressional and dilational settings. Nucleation is at the middle (along-strike) of the primary fault. The stepover width, or offset distance, is variable and allows us to determine the maximum distance rupture can jump (perpendicular to strike). The secondary fault is placed to simulate either a compressional or extensional regime, given the same regional shear stress direction (figure 2.1). Additionally, stepover ruptures are simulated in high and low stress regimes with the absolute level of stress differing by a factor of approximately 5 (see tables 2.1-2.2).

For dip-slip models, dip angle and downdip length are fixed at 45 degrees and 35 km, respectively. Nucleation is at approximately 18.4 km depth. The direction of shear stress is switched to simulate either a reverse or normal fault. FaultMod generates meshes, uses grid doubling away from the fault system to reduce computation resources without loss of accuracy, incorporates artificial viscous damping (Dalguer and Day, 2007) as well as algorithmic damping to help damp spurious oscillations, and energy-absorbing boundary conditions to diminish artificial reflections from the model boundaries.

Laboratory-derived friction laws (Dieterich, 1978b, 1979; Ruina, 1980, 1983) are used in our simulations to mimic the frictional properties of rock. The general form of the rate- and state- constitutive law (Ruina, 1983; Linker and Dieterich 1992) is:

$$\tau = \left[\mu_o + a \ln\left(\frac{V}{V_o}\right) + b \ln\left(\frac{\theta}{\theta_o}\right) \right] \sigma^{eff} \tag{2.2}$$

where μ_o represents a constant reference value for the coefficient of friction; a and b are constitutive parameters estimated from laboratory experiments; V_o and θ_o are reference values for slip rate and the state of the sliding surface, respectively; θ can be thought of as the average age of contacts at some sliding velocity; V is the slip speed and σ^{eff} is the effective normal stress (incorporating pore fluid pressure). FaultMod implements a modified arcsinh form of the friction coefficient (bracketed term in eq. 2.2) that does not become singular for very small slip velocities:

$$\mu = \arcsin h\left[\frac{V}{2V_o} \exp\left(\frac{\mu_o + \psi}{a}\right) \right] \approx \mu_o + a \ln\left(\frac{V}{V_o}\right) + \psi \tag{2.3}$$

This form closely approximates eq. 2.2 for all slip rates of seismological interest. Note that the right hand side of eq. 2.3 has the form of the effective friction coefficient in eq. 2.2, with $\psi = b\ln(\theta/\theta_o)$, or conversely, $\theta = \theta_o \exp(\psi/b)$.

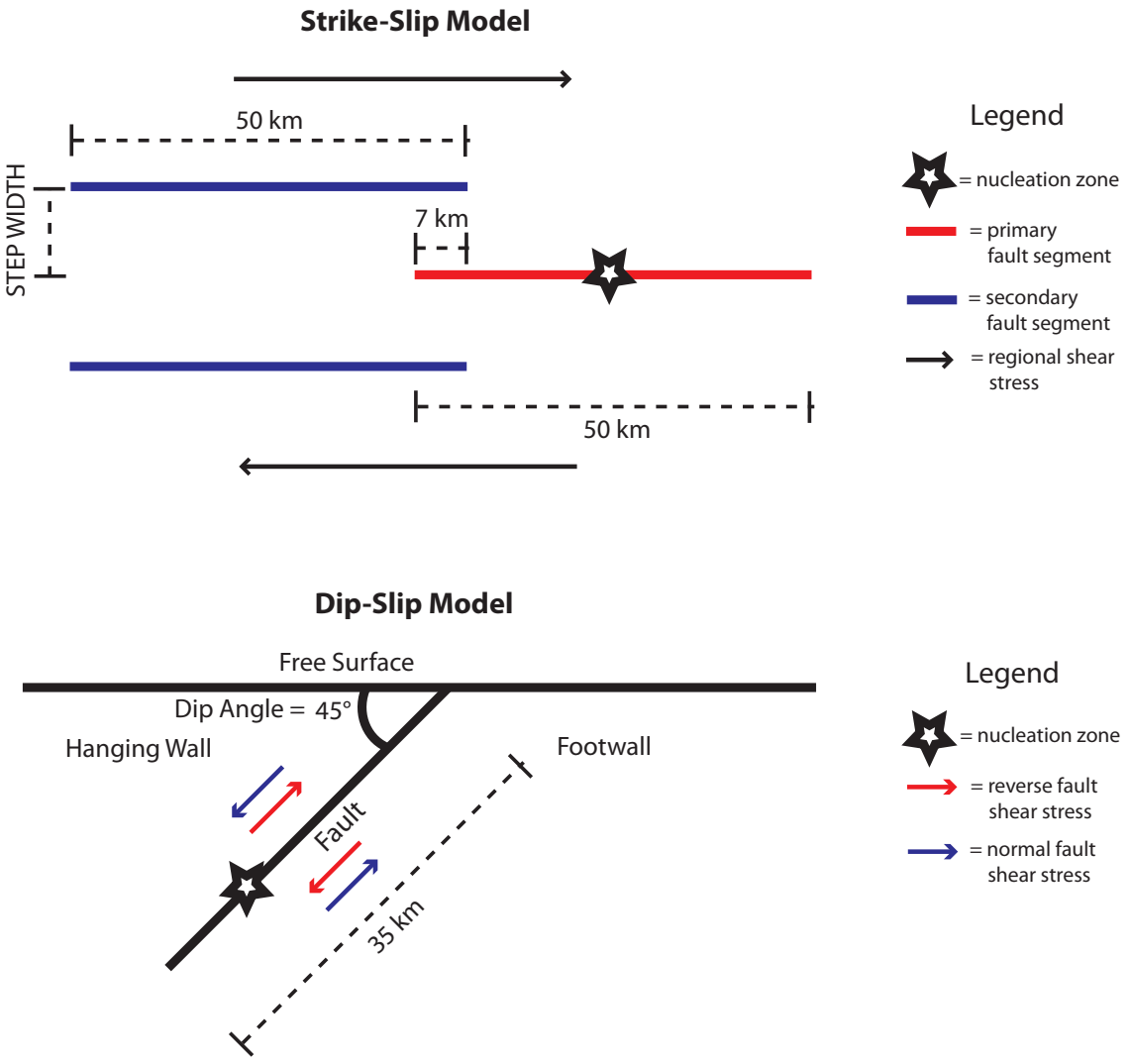

Figure 2.1. Cartoon fault geometry of 2-D models for stepovers (in mapview) and dip-slip faults (in profile view) using dynamic finite element code FaultMod (Barall, 2008). For any given stepover simulation, only one secondary fault (represented by a blue line) is present, indicating either a compressional or dilational regime. Step width is variable. For any given dip-slip simulation, only one type of stress regime is present (represented by either red or blue arrows), indicating either a reverse or normal fault. Fault dip angle and downdip distance are fixed. Arrows denote the shear stress direction. The star denotes the nucleation zone.

2.1 Low Stress Models

τ_o	13.78 - 16.10 MPa
σ_o	24.00 MPa
τ_o (nucleation zone)	20.00 MPa
Density	2670 kg/m^3
S-wave speed	3464 m/s
P-wave speed	6000 m/s
Nucleation Radius	3000 m
Nucleation Speed	1750 m/s
Element Size	~100 m
V_{ini}	1.000e-12 m/s
V_o	1.000e-6 m/s
a	0.008000
b	0.01200
a (rate-strengthening)	0.01600
L (ageing law)	0.02330 m
L (slip law)	0.1505 m
μ_o	0.6000
μ_{lv}	0.6000
μ_w	0.3000
V_w	0.1000 m/s
α	0 – 0.5000
μ_{static}	0.8299
$\mu_{dynamic}$	0.5487
d_o	≈0.6 m

2.2 High Stress Models (stepover models only)

τ_o	75.00 MPa
σ_o	120.0 MPa
τ_o (nucleation zone)	100.0 MPa
Density	2670 kg/m^3
S-wave speed	3464 m/s
P-wave speed	6000 m/s
Nucleation Radius	600.0 m
Nucleation Speed	1750 m/s
Element Size	50.00 m
V_{ini}	1.000e-12 m/s
V_o	1.000e-6 m/s
a	0.008000
b	0.01200
L (ageing law)	0.02015 m
L (slip law)	0.1000 m
μ_o	0.6000
μ_{lv}	0.6000
μ_w	0.3000
V_w	0.1000 m/s
α	0 – 0.2000
μ_{static}	0.8465
$\mu_{dynamic}$	0.5340
d_o	≈0.6 m

Tables 2.1-2.2. Stress values, material properties, model properties, and friction parameters used for low and high stress models. Both dip-slip and stepover models utilize table 2.1 properties; only stepover models utilize table 2.2 properties in addition.

For the rate-state ageing law (RS-AL), the state variable evolves according to the equation:

$$\frac{d\psi}{dt} = \frac{-bV_o}{L}\left(\exp\left(\frac{-\psi_{ss}}{V}\right) - \exp\left(\frac{-\psi}{b}\right)\right) \tag{2.4a}$$

In the rate-state slip law (RS-SL), the state variable evolves according to the equation:

$$\frac{d\psi}{dt} = \frac{-V}{L}\left(\psi - \psi_{ss}\right) \tag{2.4b}$$

where L is the characteristic length in the rate-state formulation, and ψ_{ss} is the steady state value that depends on slip velocity and the characteristic length L. We use values of L for both the RS-AL and RS-SL that correspond to an effective slip-weakening distance of about 0.6 m. Both laws have the same standard steady-state formula:

$$\psi_{ss} = -b\ln\left(\frac{V}{V_o}\right) \tag{2.5}$$

One version of our RS-SL models incorporates strong rate-weakening, which is intended to simulate flash heating around some sliding velocity, via its steady-state formula, with which a relatively larger drop in shear stress occurs around some reference velocity:

$$\psi_{ss} = a\ln\left(\frac{2V_o}{V}\sinh\left(\frac{\mu_{ss}(V)}{a}\right)\right) \tag{2.6a}$$

$$\mu_{ss}(V) = \mu_w + \left(\mu_{lv}(V) - \mu_w\right)\left(1+\left(\frac{V}{V_w}\right)^{1/8}\right)^{-1/8} \tag{2.6b}$$

$$\mu_{lv}(V) = \mu_s - (b-a)\ln\left(\frac{V}{V_o}\right) \tag{2.6c}$$

where μ_s is the strong friction coefficient, μ_w is the weak friction coefficient, and V_w is the velocity around which the weakening occurs.

In order to incorporate normal stress effects on the state variable we use an adapted form of eq. 13 from Linker and Dieterich (1992, eq. 2.1 in this study):

$$\frac{d\psi}{dt} = \frac{-\alpha}{\sigma+\sigma_{off}}\frac{d\sigma}{dt} \tag{2.7}$$

where α is the Linker-Dieterich parameter that scales the effect of normal stress on state (determined experimentally), σ is the normal stress, and σ_{off} is an offset stress to keep the equation stable at low values of normal stress. The total evolution of ψ, for each time step, is the combination of eqs. 2.4a and 2.7, or 2.4b. and 2.7 using the ageing law or slip law, respectively. Since an increase/decrease in ψ corresponds to an increase/decrease in the friction coefficient by almost the same amount (see eq. 2.3), a change in normal stress

with time results in a change in friction coefficient with time of the opposite sign (see eq. 2.7). For example, a positive change in normal stress (clamping) results in a transient decrease in friction coefficient, and vice versa. Note that most previous studies (chapter 1) have used only eqs. 2.4a and 2.4b for the evolution of the state variables – particularly in cases of complex fault geometry. In the previous chapter, the state variable depended on slip speed history and time, whereas now it depends on slip speed history, time, and normal stress history. The Linker-Dieterich parameter α has been experimentally determined to be in the range 0.2-0.56 for low slip speeds (i.e., μm/sec) (Linker and Dieterich, 1992). For our stepover models, we use a value of 0 or 0.2 for α. For our dip-slip models, we use values of 0, 0.2, and 0.5 in order to illuminate trends for reverse and normal fault ruptures. For comparison, some models incorporate classic slip-weakening friction, where friction coefficient drops linearly with slip from the yield coefficient to the final coefficient over a critical slip-weakening distance. In this manner we can assess which aspects of our results are exclusive to rate-state friction, and which are more generic.

In order to simulate zones of weak fault coupling near the free surface of our dip-slip models, we incorporate rate-strengthening frictional behavior. We note the differential equation of steady state friction with respect to the logarithm of slip velocity:

$$\frac{df_{ss}}{d\ln V} = a - b \tag{2.8}$$

This equation shows that when constitutive parameter b is larger than constitutive parameter a, the steady state friction value decreases as velocity increases, and thus

represents a velocity-weakening zone. However, when constitutive parameter b is smaller than constitutive parameter a, the steady state friction value increases with increasing velocity, and represents a velocity-strengthening zone. Such a zone is seismically stable, and in principle cannot spontaneously nucleate earthquake slip. Since Dieterich (1978b, 1979) experimentally determined a and b values to be on the order of 0.01, we use values of 0.008 and 0.012 for parameters a and b, respectively, for all rate-weakening models. We use values of 0.016 and 0.012 for parameters a and b, respectively, in the uppermost 5 km (along dip) for one reverse fault model and one normal fault model to represent a region of rate-strengthening.

For dip-slip models, we vary the initial shear stress (i.e., loading stress) from 13.78 MPa to 16.10 MPa with constant normal stress of 24 MPa, which produces a range of rupture velocities. The type of rupture (i.e., crack-like vs. pulse-like) can depend on the initial loading conditions; a self-healing, pulse-like rupture has been shown to be more likely under lower loading stress conditions, when compared to the requirements for crack-like rupture (Zheng and Rice, 1998). For analogous classic slip-weakening models, this corresponds to changing the seismic S ratio ($S = \tau_y-\tau_o/\tau_o-\tau_f$, where τ_y is the yield shear stress,τ_o is initial shear stress, and τ_f is the final shear stress). Decreased loading stress corresponds to an increase in S.

Results

Stepovers

Using the Linker-Dieterich formulation we test the effects of normal-stress-dependent state (eq. 2.7) on dynamic ruptures at stepovers. In the following we compare the maximum rupture-jumping distance for models with $\alpha = 0$ (no dependence of state on normal stress) and $\alpha = 0.2$ (figure 2.2). The maximum jump distance should be sensitive to changes in frictional strength along the re-nucleation zones of the secondary fault segments. We see that in both extensional and compressional stepover regimes, models with $\alpha = 0.2$ have smaller maximum jump distances than models with $\alpha = 0$ for all friction laws. Larger values of alpha (e.g., 0.5) continue the effect of decreasing maximum jump distance with increasing alpha, but for brevity we do not show those results in this study. The results for dilational and extensional stepovers may seem counter-intuitive: according to the Linker-Dieterich formulation one might expect results to be anti-symmetric (i.e., decreasing jump distance for extensional stepovers and increasing jump distance for compressional stepovers) since extension should lead to increased friction and compression should lead to decreased friction (according to eq. 2.5). However, we have found that both the dilational and compressional stepover models re- nucleate rupture on the secondary fault segments in regions of decreased normal stress, although the magnitude of such normal stress reductions is quite different for dilational vs. compressional stepovers (figure 2.3). In both cases, decreased normal stress results in a short-term increase in state and friction, compared to standard slip-weakening friction. Thus, incorporating normal stress dependent state (eq. 2.5) in the

models reduces the maximum jumpable stepover width for both extensional and compressional stepovers relative to models with no such normal stress dependence in state, since the state variable, and hence frictional resistance, is increased in regions of dynamic normal stress reduction. We note that stepover models in this study are crack-like (i.e., slip pulses are spatially large and fall off asymptotically).

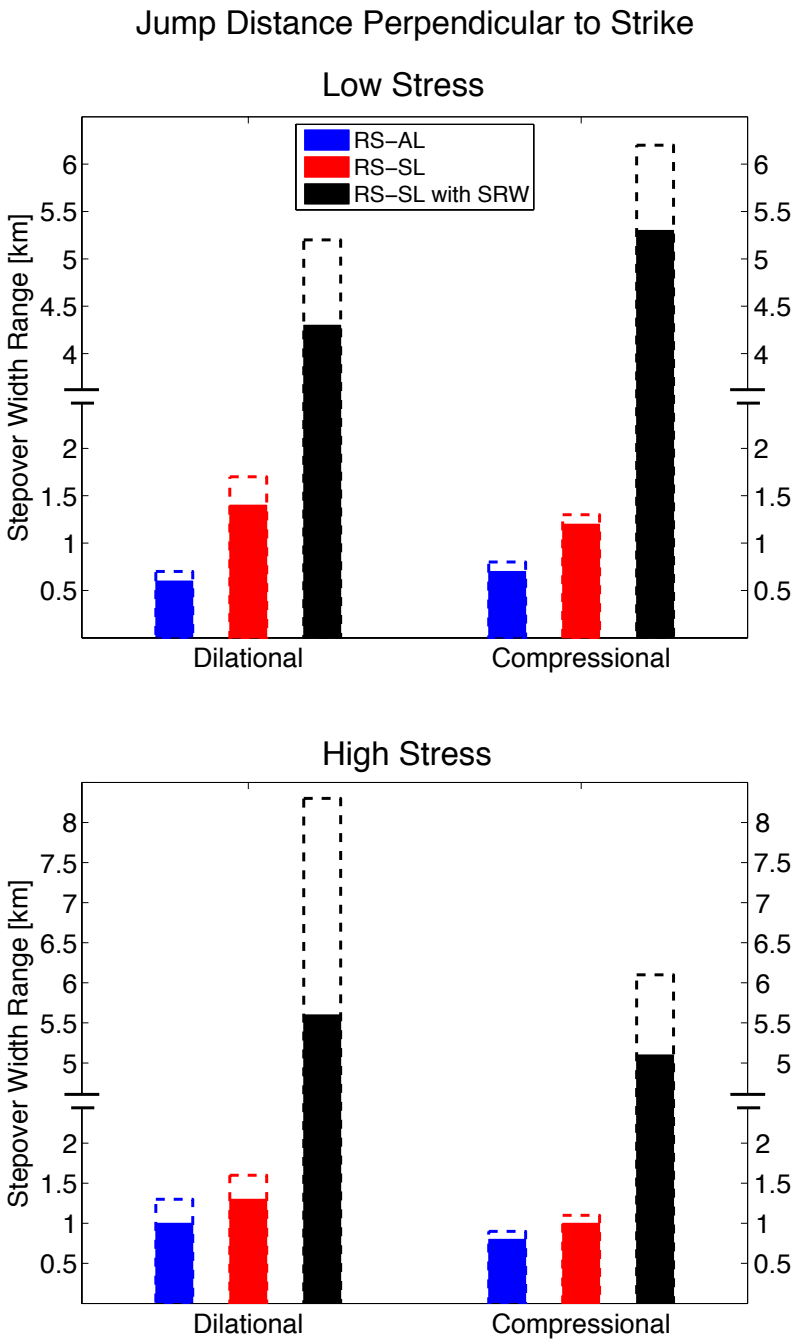

Figure 2.2. Maximum jump distance without (dashed bars) and with (solid bars) a normal-stress-dependent state (α=0.2) for all rate-state friction laws. All rate-state friction laws show a decrease in max jump distance for both dilational and compressional steps. In this study, the difference in maximum jump distance that results from a normal-stress-dependent state is more substantial for dilational systems than for compressional systems. Both low and high stress models are shown.

The decrease in maximum jump distance due to a normal-stress-dependent state variable shown in figure 2.2 is more substantial for dilational stepovers than compressional stepovers. In other words, the ratio of the amount of decrease to the maximum jump distance without a normal-stress-dependent state is larger for dilational models. This is due to the difference in magnitude of dynamic normal stress reduction that facilitates re-nucleation at dilational versus compressional steps. With that in mind we analyze snapshots of stress and state variable ψ along strike, immediately before re-nucleation on the secondary faults with the RS-SL and RS-AL (figure 2.3). Note that for figure 2.3 we choose to display results for stepovers with the largest maximum jump distance with a normal-stress-dependent state, since these are large step models common to both normal-stress-dependent and normal-stress independent states. For a 1.4 km dilational stepover with a low stress regime using the RS-SL (figure 2.3a) we find that re-nucleation takes place in a region of increased shear stress and reduced normal stress. The area around the re-nucleation location (black-dashed circle in figure 2.3a) shows a substantial increase in the state variable, and therefore friction coefficient. The increase in friction coefficient makes it harder for rupture to re-nucleate, and thus decreases the maximum jumpable distance. However, the re-nucleation zone is bordered by a region of increased normal stress on the left that corresponds to a decrease in state that would promote rupture toward the left once it started. For a 1.2 km compressional stepover with a low stress regime using the RS-SL (figure 2.3b) we find that re-nucleation takes place in a region of increased shear stress and reduced normal stress, and is bordered to the right by a large region of increased normal stress. In spite of the different nature of the

stepover, this effect is similar to that of the dilational stepover. The region surrounding the nucleation midpoint shows an increase in the state variable and therefore friction coefficient, however, it is bordered to the right by a large region of decreased state variable. The bordering region of decreased state variable is certainly close enough to the nucleation midpoint to influence re-nucleation in a way that makes it less resistant than the comparable dilational model in figure 2.3a. While this effect may be dependent on critical crack size, it explains why the max jump distance is reduced more so for the dilational stepovers than for the compressional stepovers when using a normal-stress-dependent state variable. Results are similar to RS-AL models (figure 2.3c-d), although there are relatively sharper peaks in normal stress change and state variable change along the re-nucleation zone for RS-AL models. Additionally, RS-AL models show larger spikes in shear stress at the edges of the primary fault after rupture has ceased there. High stress models show similar results to that of the low stress models.

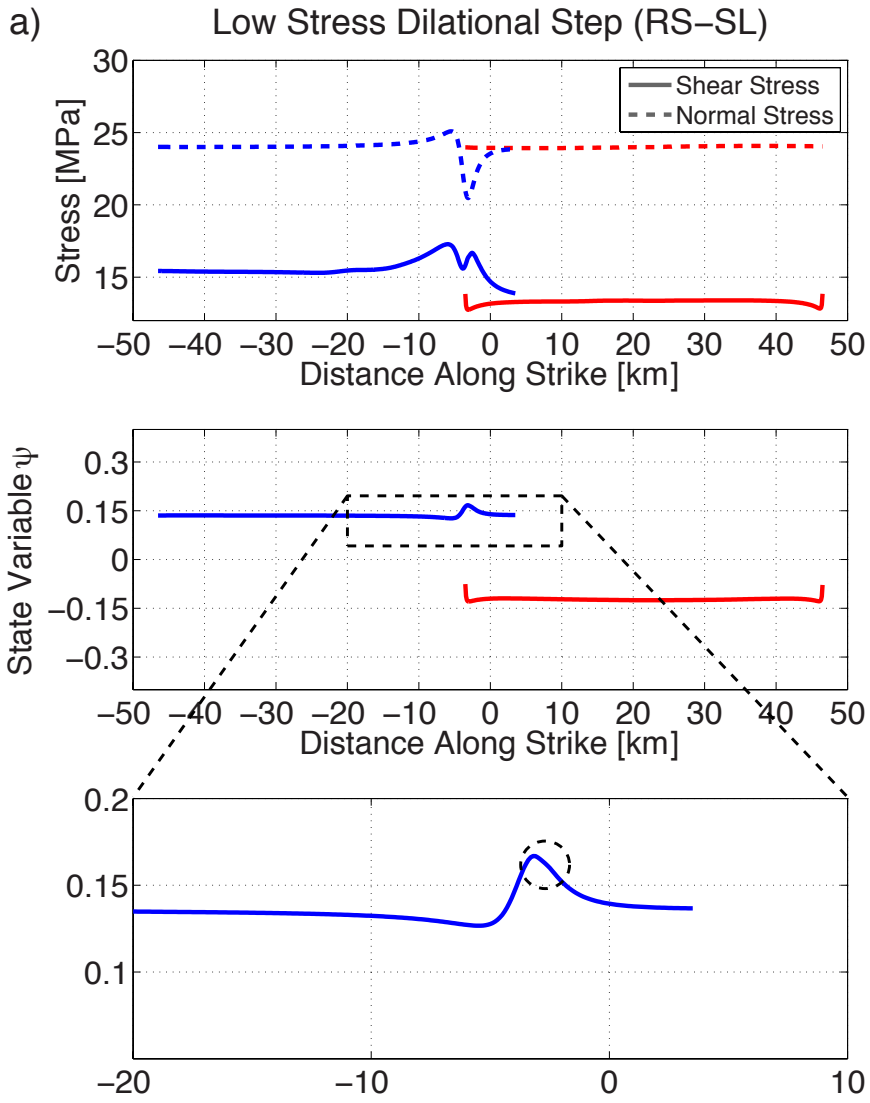

Figure 2.3a. Stress and state snapshot immediately before re-nucleation across a 1.4 km dilational step using the slip law with low stress. Both shear and normal stresses are shown. Red indicates the primary fault and blue indicates the secondary fault. A change in normal stress results in a change of the state variable that opposes the effect of clamping or unclamping on the fault friction. We use an alpha of 0.2, in agreement with laboratory experiments (Linker and Dieterich, 1992). The dashed black circle indicates the location of re-nucleation. Re-nucleation takes place in a zone of decreased normal stress and therefore increased state. Additionally, there is a zone of decreased state that borders re-nucleation on the left. The magnitude of this effect (change in state with change in normal stress) depends on the alpha parameter in the state evolution equation.

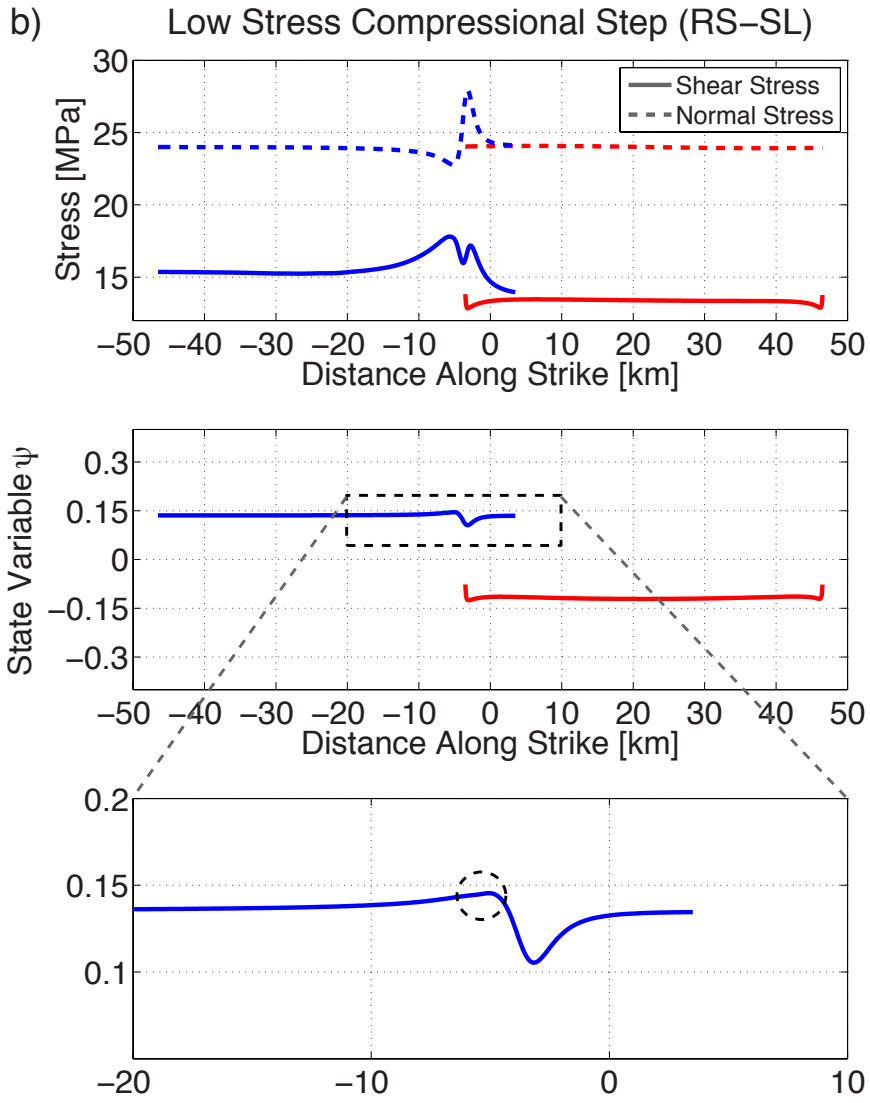

Figure 2.3b. Stress and state snapshot immediately before re-nucleation across a 1.2 km compressional step using the slip law with low stress. Both shear and normal stresses are shown. Red indicates the primary fault and blue indicates the secondary fault. The dashed black circle indicates the location of re-nucleation. Re-nucleation takes place in a zone of decreased normal stress and therefore increased state. Note that the increase in state along the re-nucleation zone is smaller for the compressional step than for the dilational step. Additionally, there is a zone of decreased state that borders re-nucleation on the right.

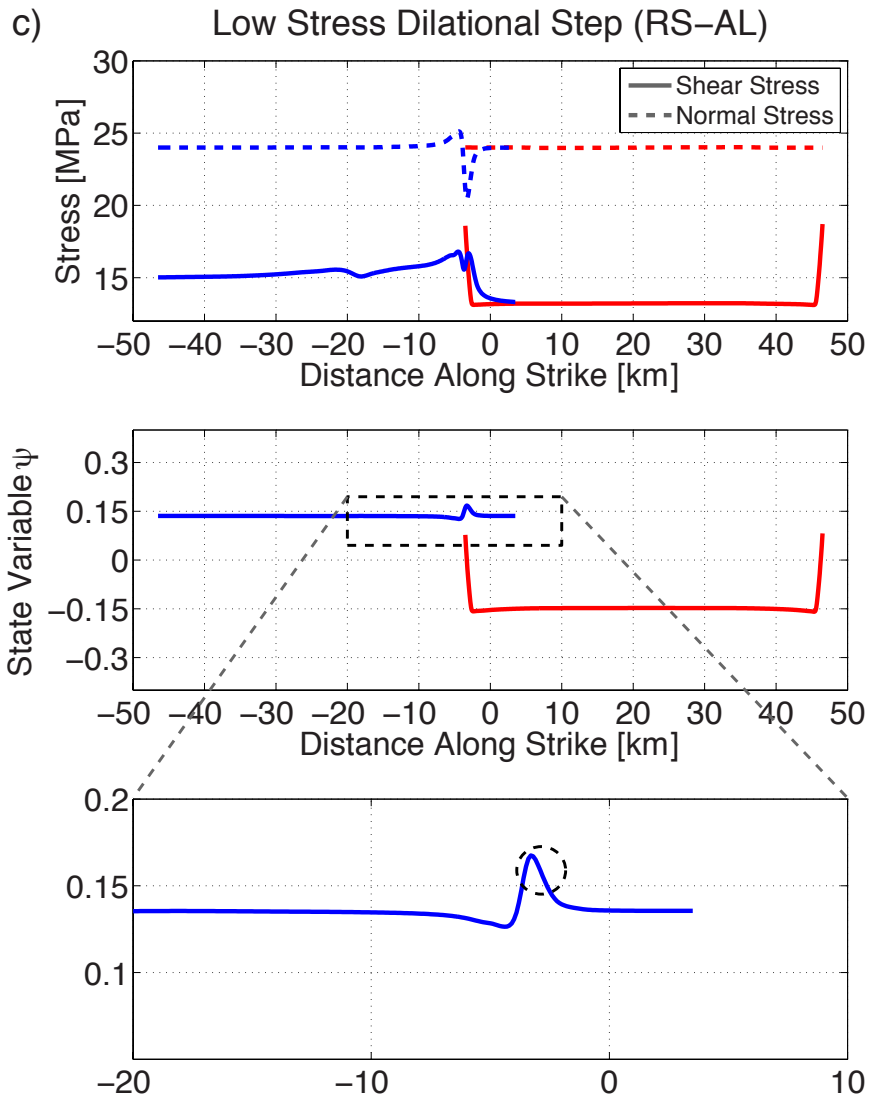

Figure 2.3c. Stress and state snapshot immediately before re-nucleation across a 0.6 km dilational step using the ageing law with low stress. Results are similar to slip law models, although there are relatively sharper peaks in normal stress change and state variable change along the re-nucleation zone for ageing law models. Additionally, ageing law models tend to produce larger peaks in shear stress at the edges of the primary fault than do slip law models.

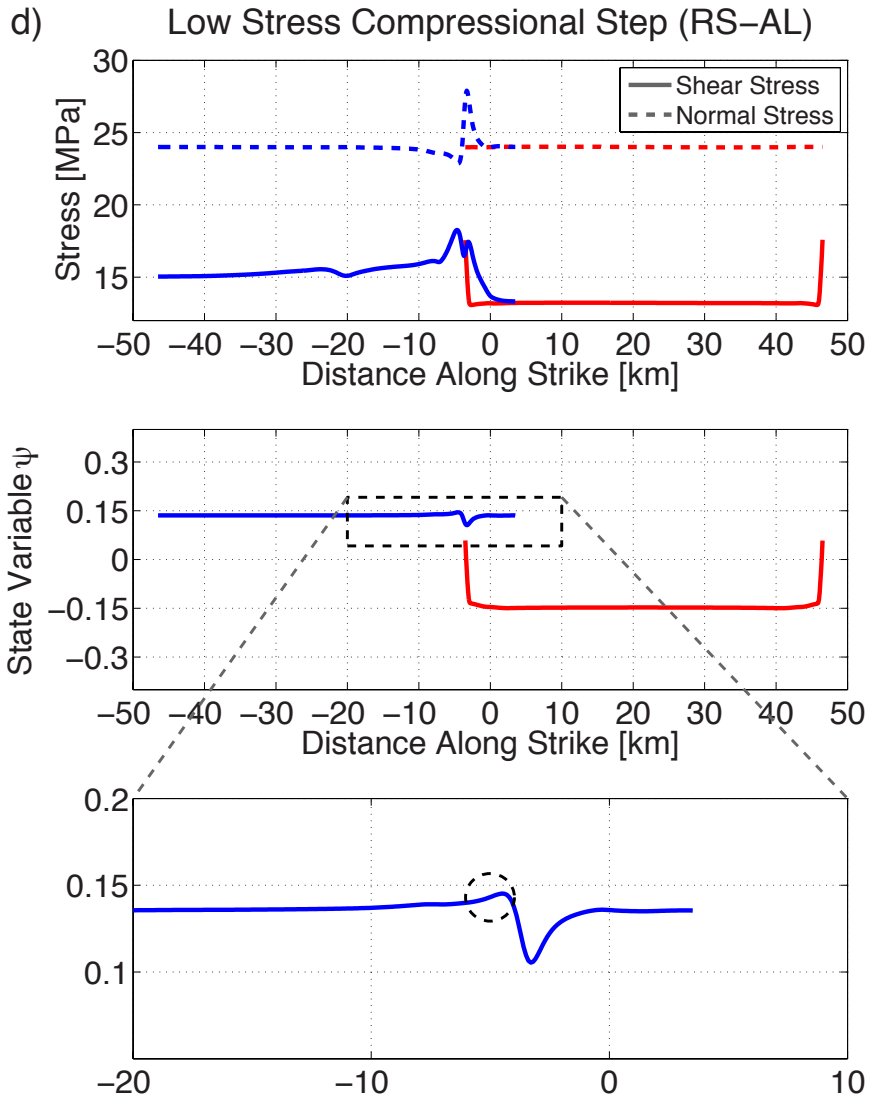

Figure 2.3d. Stress and state snapshot immediately before re-nucleation across a 0.7 km compressional step using the ageing law with low stress. Again, results are similar to slip law models, although there are relatively sharper peaks in normal stress change and state variable change along the re-nucleation zone for ageing law models.

In figure 2.4 we examine the weakening (i.e., stress vs. slip) curves for points within 1 km of the nucleation midpoints for both a typical dilational stepover model and a typical compressional stepover model using both RS-SL and RS-AL laws, with and without a normal-stress-dependent state variable ($\alpha = 0.2$ or $\alpha = 0$). The insets show maximum shear resistance for simulations. In all cases, including normal-stress-dependent state results in an increase in maximum shear resistance. However, both laws show a relatively larger increase in frictional resistance for dilational stepovers than compressional stepovers. This result is consistent with the observation that both dilational and compressional stepovers re-nucleate in regions of decreased normal stress, and thus increased fault strength (increased state) relative to the $\alpha = 0$ case. The increase in shear resistance for dilational systems is present over almost the entire effective slip weakening distance ($\approx$0.6 m), implying that in such cases there is a larger increase in dissipated surface energy (i.e., the area under the curves from 0 to 0.6 m slip) during the nucleation process for the dilational stepovers than the compressional stepovers. Note that figure 2.4 gives results for step widths that correspond to maximum jump distance with a normal-stress-dependent state.

Dip-Slip Faults

We also use the Linker-Dieterich frictional formulation in dynamic dip-slip models to investigate how normal-stress-dependent state may affect the asymmetric properties of reverse and normal faults, which result from the free surface boundary condition (Brune,

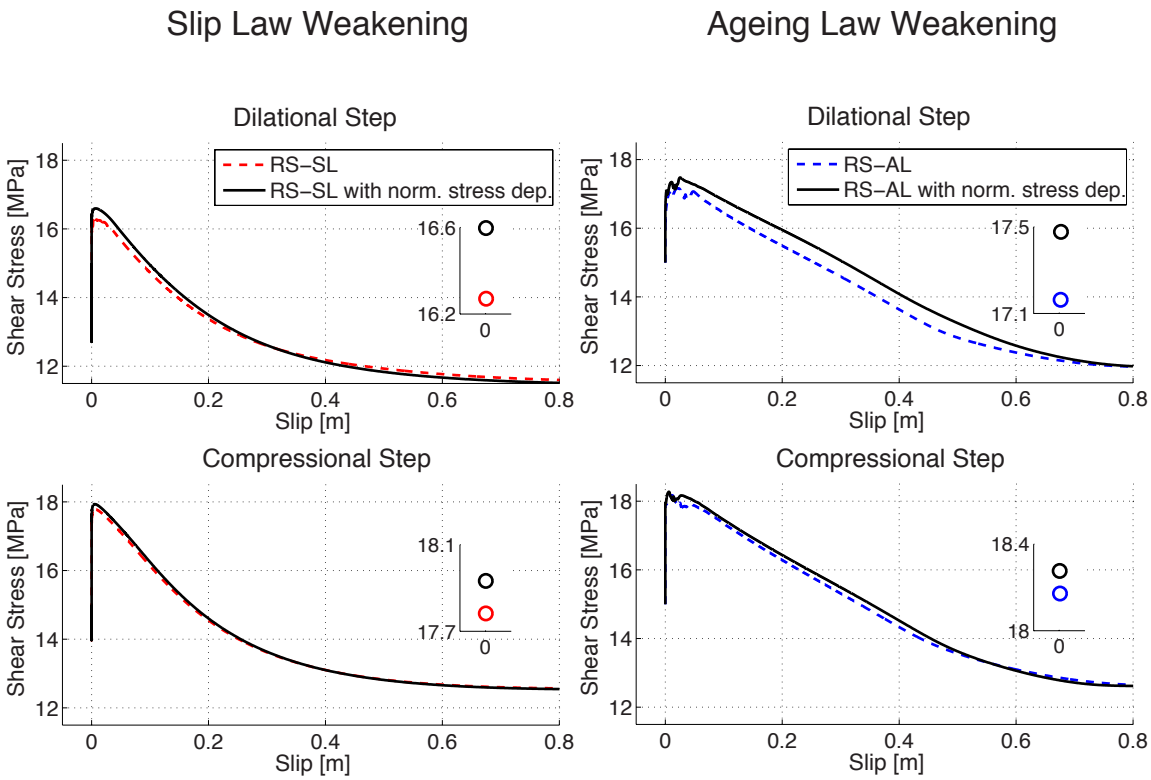

Figure 2.4. Weakening curves for models using the rate-state slip law and ageing law parameterizations. Each weakening curve represents an average from locations within 1 km of the re-nucleation midpoint. The left panels show results for dilational and compressional step widths of 1.4 and 1.2 km, respectively, using the slip law with and without normal-stress dependence. The right panels show results for dilational and compressional step widths of 0.6 and 0.7 km, respectively, using the ageing law with and without normal-stress dependence. All insets show the maximum shear stress value with and without normal-stress dependence (with the same units as the main plots). For both rate-state laws there is a larger amount of dissipated energy (area under the curves) for models with normal-stress dependence than models without it. Additionally, dilational steps show larger differences in dissipated energy than compressional steps between models with and without normal-stress dependence as well as larger differences in maximum shear stress. Note that all axes are scaled equally between the main plots and the insets.

1996; Nielsen, 1998; Oglesby et al., 1998, Oglesby and Archuleta, 2000a: Oglesby et al., 2000b). This well-known asymmetry in fault and ground motion between thrust and normal faults is associated with the effect of the free surface on the fault stress: as rupture approaches the free surface along a normal fault, there is a decrease in normal stress ahead of the crack tip and an increase in normal stress behind the crack tip, with the opposite effect for reverse faults. Previous numerical studies using rate-state friction have not investigated such effects; we do so by analyzing peak slip speeds and total slip for reverse and normal faults at various values of α. Additionally, we vary the initial shear stress (i.e., loading stress) for slower, more pulse-like ruptures (Zheng and Rice, 1998) and investigate how waves reflecting off the free surface interact with the rupture front (Oglesby et al., 1998). Finally, we investigate how a rate-strengthening zone near the free surface affects these results.

Figure 2.5a-c shows peak slip speed for models using the RS-AL, RS-SL, and SW friction. Reverse fault models always have larger peak slip speeds than normal fault models, consistent with previous studies (e.g., Oglesby and Archuleta, 2000a). Figure 2.5a shows that increasing α from 0 to 0.5 tends to reduce the asymmetry between reverse and normal models using the RS-AL, making them more similar. Decreasing the loading stress tends to decrease peak slip speed for both reverse and normal faults. For a lower loading stress (14.29 MPa), normal fault ruptures do not propagate to the free surface while the reverse fault ruptures do. Figure 2.5b shows similar results using the RS-SL with regard to α, however, both reverse and normal fault rupture penetrate to the

free surface under all loading stress regimes. This difference is due to differing energy budgets associated with the laws, given the same effective slip-weakening distance. By plotting their effective slip-weakening curves one can see differences in energy budget between friction laws (chapter 1, figure 1.2). Note that the RS-SL has a relatively non-linear weakening curve when compared to the RS-AL, possibly leading to larger slip rates at the edges of the nucleation zone, especially since we implement the same nucleation speed and length for both laws. In figure 2.5c we include the classic slip-weakening models to show that loading stress effects are not RS dependent; the results are very similar to those of the RS-AL with $\alpha = 0$.

Figure 2.6a-c displays total slip for dip-slip models using the RS-AL, RS-SL, and classic slip-weakening friction. Although varying α has noticeable effects on peak slip speeds for both reverse and normal fault models, it does not seem to greatly affect total slip (figure 2.6a-b). However, small differences in total slip updip (that indicate rupture extent) seen in RS-AL models show rupture traveling slightly more updip for normal faults with increasing α, and the opposite is seen for reverse faults. Since smaller loading stresses result in less energetic ruptures, total slip decreases with decreasing loading stress for all models. However, as noted before, all RS-SL models rupture to the free surface.

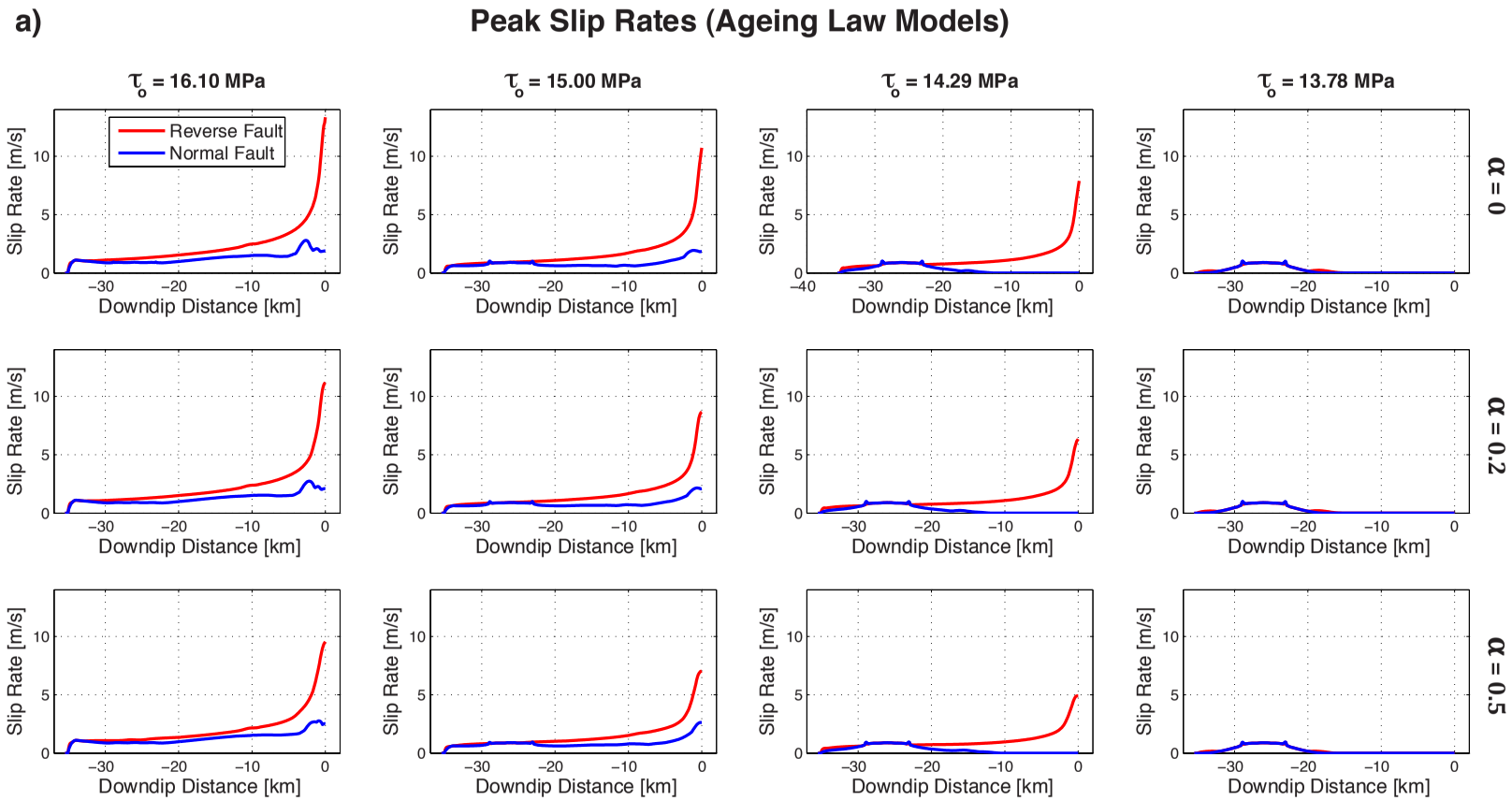
a)
Peak Slip Rates (Ageing Law Models)
τo = 16.10 MPa
τo = 15.00 MPa
τo = 14.29 MPa
τo = 13.78 MPa
Reverse Fault
Normal Fault
Slip Rate [m/s]
Downdip Distance [km]
α = 0
α = 0.2
α = 0.5

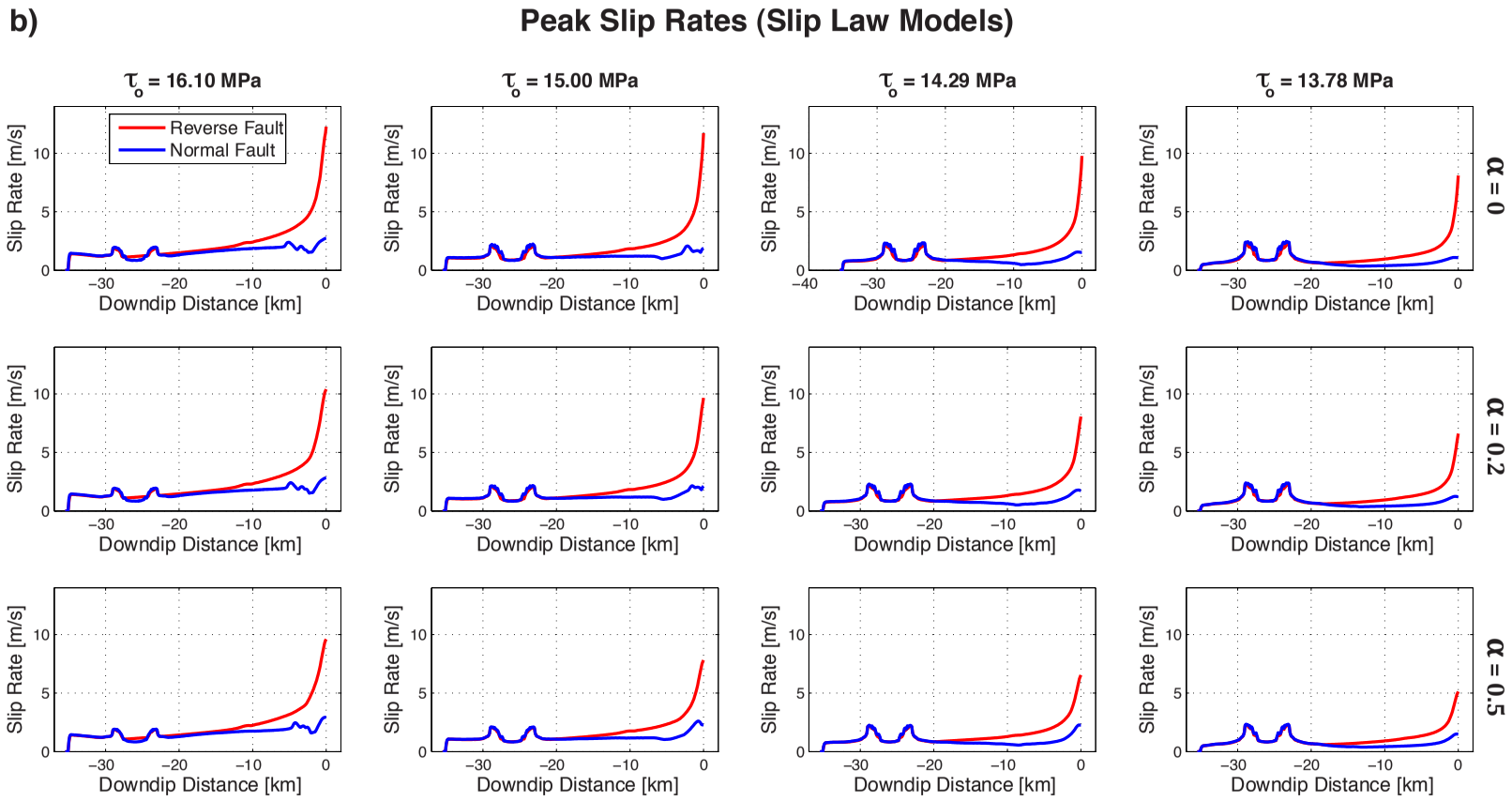
b)
Peak Slip Rates (Slip Law Models)
τo = 16.10 MPa
τo = 15.00 MPa
τo = 14.29 MPa
τo = 13.78 MPa
α = 0
α = 0.2
α = 0.5
Reverse Fault
Normal Fault
Slip Rate [m/s]
Downdip Distance [km]

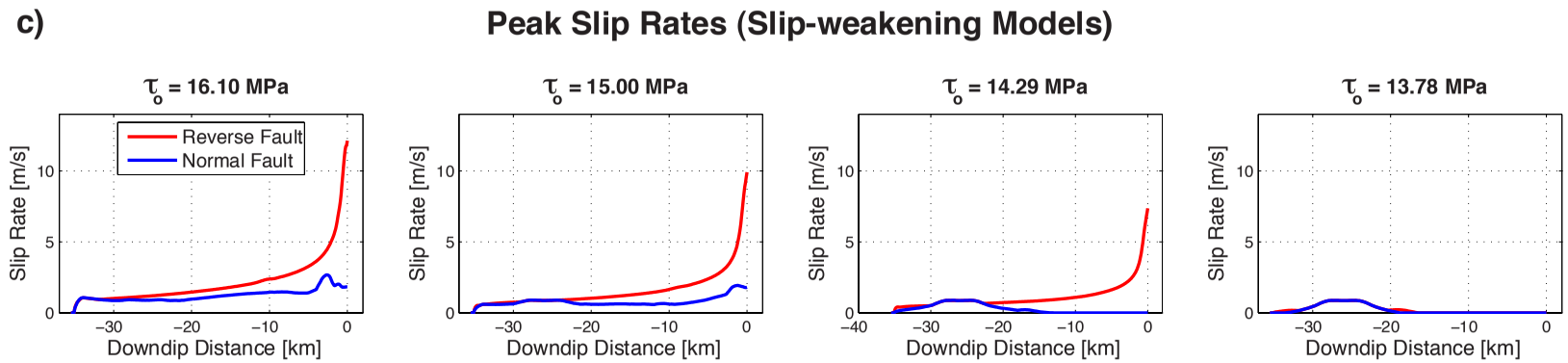

Figure 2.5. (a) Peak slip rates for ageing law models. The free surface is at 0 km downdip. We vary both α and τ_o (loading stress) for rate-state models. Reverse fault models show larger peak slip rates than normal-fault models due to the effect of time-dependent normal stress (induced by the free surface interaction) on fault friction. Both reverse and normal fault models show decreasing peak slip rates with decreasing loading stress. Rupture propagation arrests before it hits the free surface for reverse faults at a loading stress of 13.78 MPa and for normal faults at 14.29 MPa, implying the dynamic stress field facilitates reverse ruptures more than normal ruptures. Increasing alpha quenches the difference in peak slip velocity between reverse and normal faults. This result shows that, as expected, increasing alpha moderates the effect of time-dependent normal stress on the fault friction. (b) Peak slip rates for slip law models. Slip law models are consistent with ageing law models. However, there are larger spikes in peak slip velocity near the nucleation zone. Additionally, both normal and reverse fault models rupture the entire fault, even for the lowest loading stress regime. (c) Peak slip rates for slip-weakening friction models. Slip-weakening friction model results are in agreement with the ageing law results for alpha = 0 (no normal dependence in the state variable).

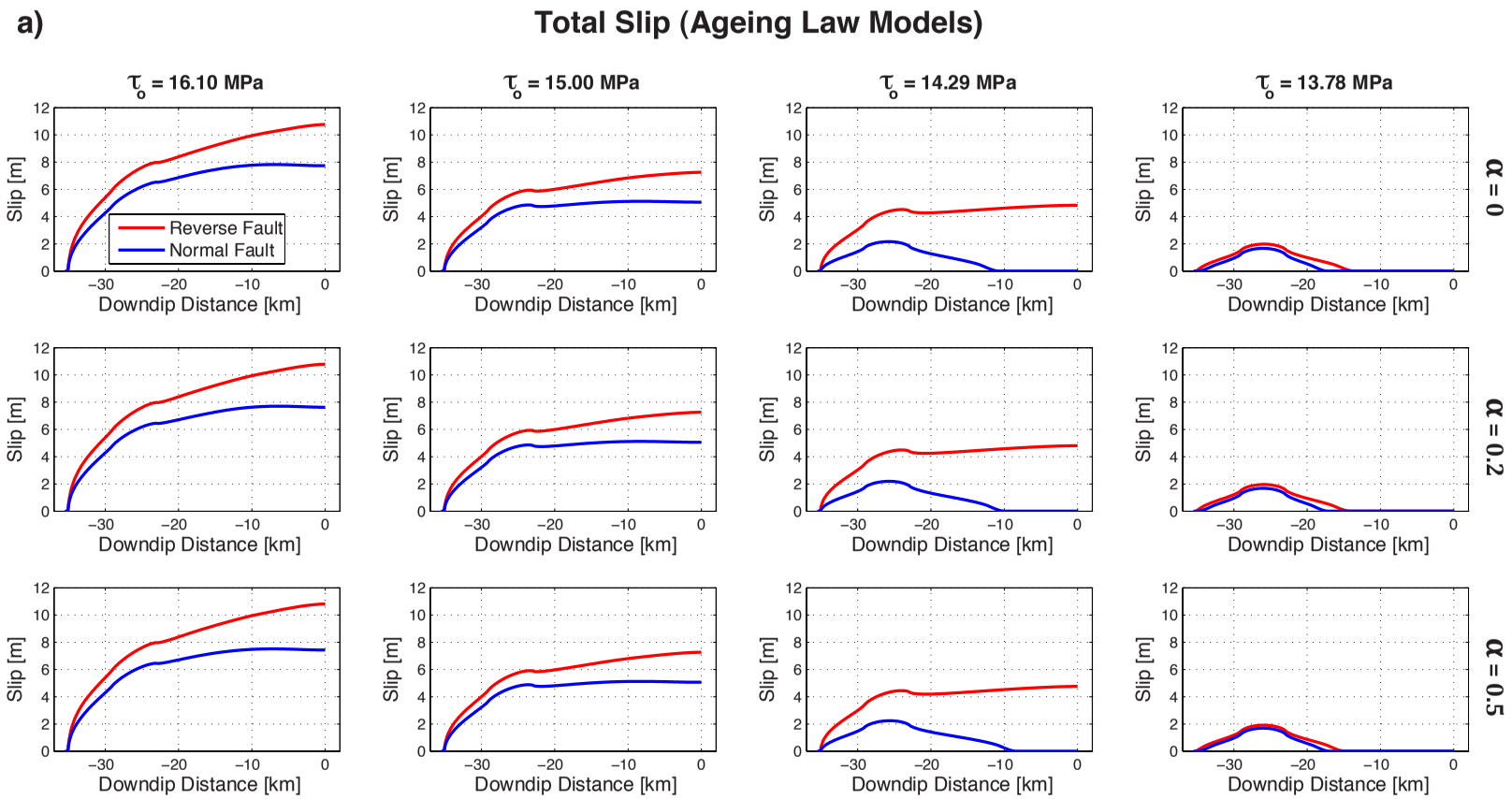
a)
Total Slip (Ageing Law Models)
τo = 16.10 MPa
τo = 15.00 MPa
τo = 14.29 MPa
τo = 13.78 MPa
α = 0
α = 0.2
α = 0.5
Slip [m]
Downdip Distance [km]
Reverse Fault
Normal Fault

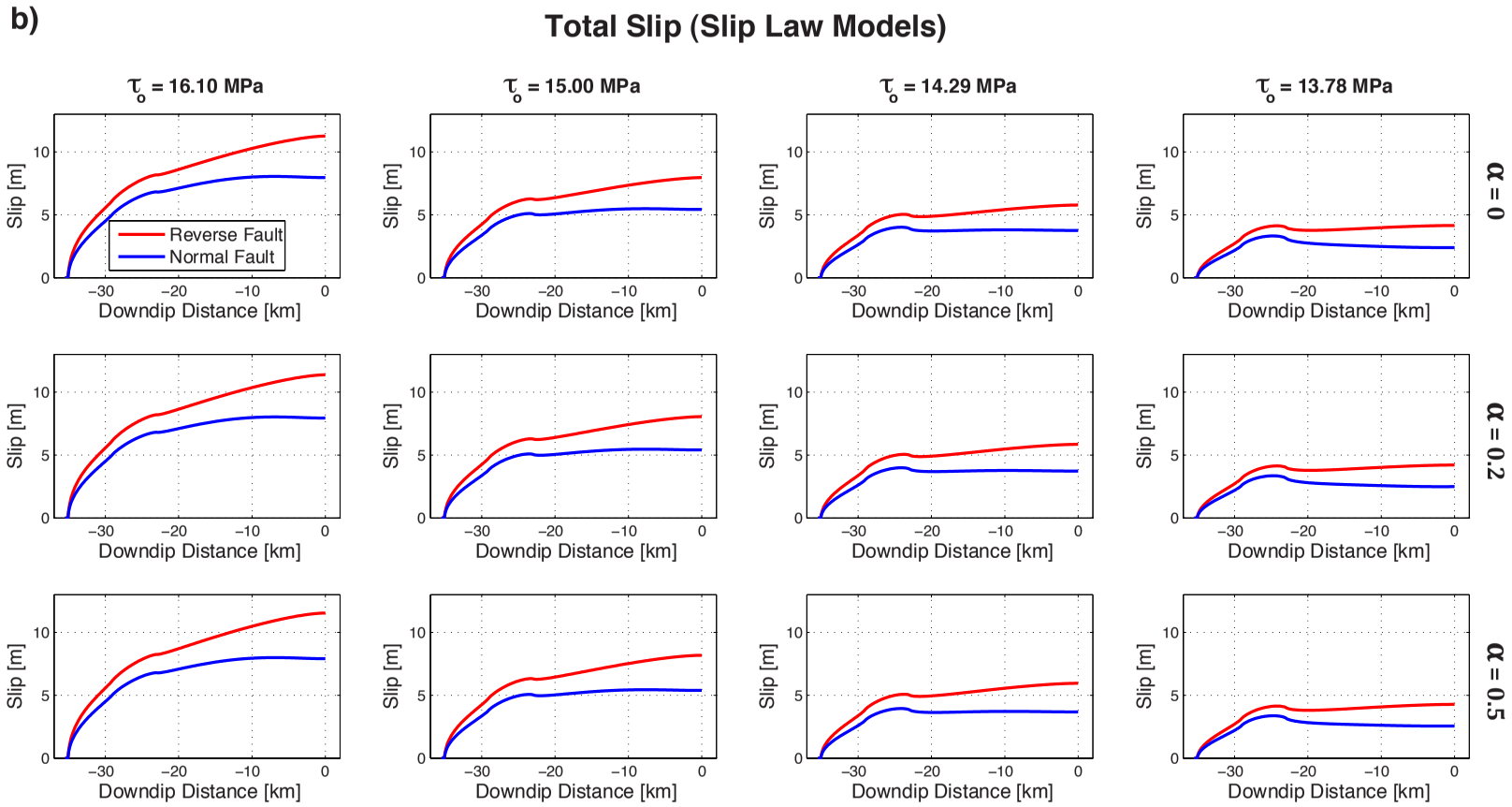
b)
Total Slip (Slip Law Models)
τo = 16.10 MPa
τo = 15.00 MPa
τo = 14.29 MPa
τo = 13.78 MPa
α = 0
α = 0.2
α = 0.5
Reverse Fault
Normal Fault
Slip [m]
Downdip Distance [km]

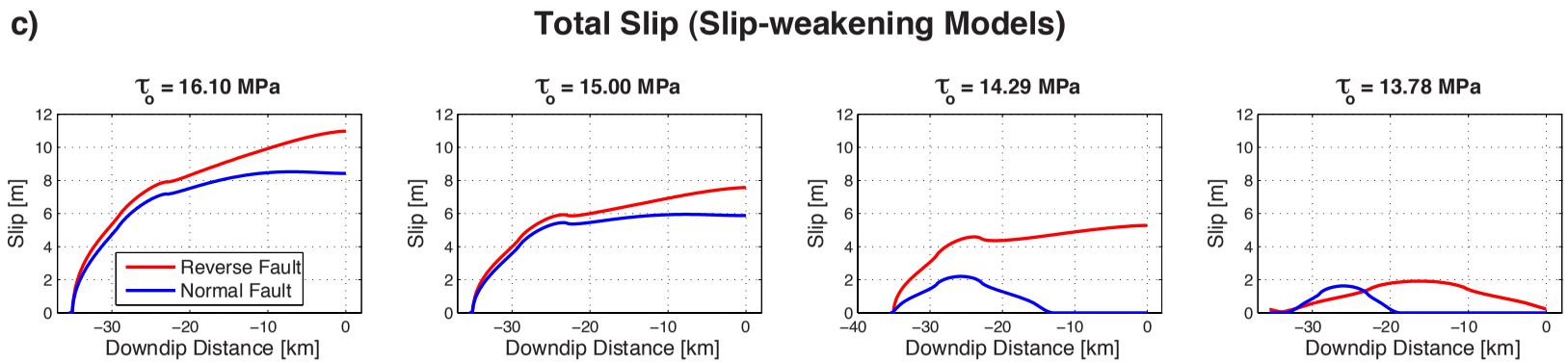

Figure 2.6. (a) Cumulative slip plots for models using the ageing law. Generally, reverse ruptures have more cumulative slip than normal ruptures. Decreasing the loading stress results in normal ruptures not propagating all the way updip, while reverse ruptures propagate further updip for the same initial conditions (i.e., loading stress). Increasing alpha does not significantly change the difference in total slip between reverse and normal faults. (b) Cumulative slip plots for models using the slip law. Changing loading stress and alpha yield similar results to ageing law models, with the exception that slip law models propagate all the way updip for low loading stresses. Note that these results may differ for other parameterizations (e.g. different prestress fields and dip angles). (c) Cumulative slip plots for models using slip-weakening friction. Decreasing loading stress yields similar results to ageing law models.

Stress snapshots of reverse and normal ruptures using the RS-AL are plotted in figure 2.7a-b to elucidate some of the complexities between rupture propagation and the free surface. Nielsen (1998) and Oglesby et al. (1998) found that as rupture approaches the free surface along a normal fault there is a decrease in normal stress ahead of the crack tip and an increase in normal stress behind the crack tip, with the opposite effect for reverse faults. Thus, the free surface causes a coupling between shear stress and (time-dependent) normal stress. The perturbations in normal stress then alter the frictional resistance and the sliding stress. For a loading stress of 16.10 MPa, figure 2.7 shows that normal stress change on the faults from the initial value reverse sign at roughly the location of the crack tip, consistent with previous studies. Thus, as the rupture propagates updip, the crack tip spends most of its time in an area with normal stress relatively unchanged from its initial value (note the position of the rupture front at 8.5 s in the τ_o = 16.10 MPa case in figure 2.7a, and at 8.6 s in the τ_o = 16.10 MPa case in figure 2.7b). However, the region of free-surface-induced normal stress fluctuation may be offset from the crack tip if the rupture is slowed by a lower loading stress (i.e., for lower initial shear stresses, the rupture front tends to lag behind). Although the fault rupture slows for such cases, the wave speeds of the entire model do not change. For a reverse fault, this effect sends the rupture front into an area of decreased normal stress (note the position of the rupture front at 9.8 s in the τ_o = 15.00 MPa case in figure 2.7a), promoting rupture. For a normal fault, this effect sends the rupture front into an area of increased normal stress, inhibiting rupture (note the position of the rupture front at 10.8 s

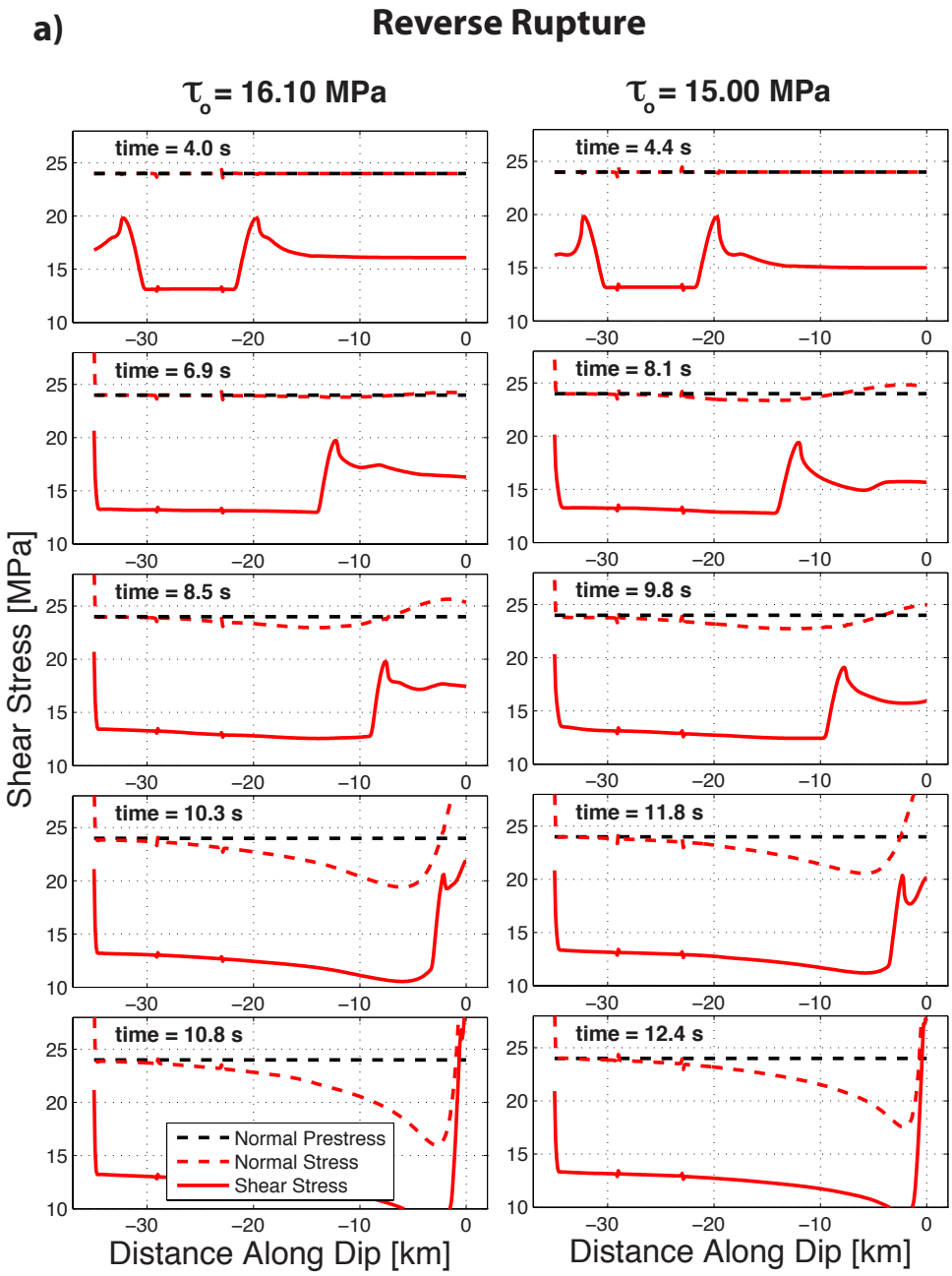

Figure 2.7a. Stress snapshots at different times for ageing law models with reverse fault ruptures. In general, the sense of normal stress change on the fault reverses sign at roughly the location of the crack tip, consistent with previous studies (e.g., Nielsen, 1998; Oglesby et al., 1998; Oglesby and Archuleta, 2000a; Oglesby et al., 2000b). However, for lower initial shear stresses (e.g., 15Mpa), the rupture front tends to lag behind. For a reverse fault, this effect sends the rupture front into an area of decreased normal stress, promoting rupture.

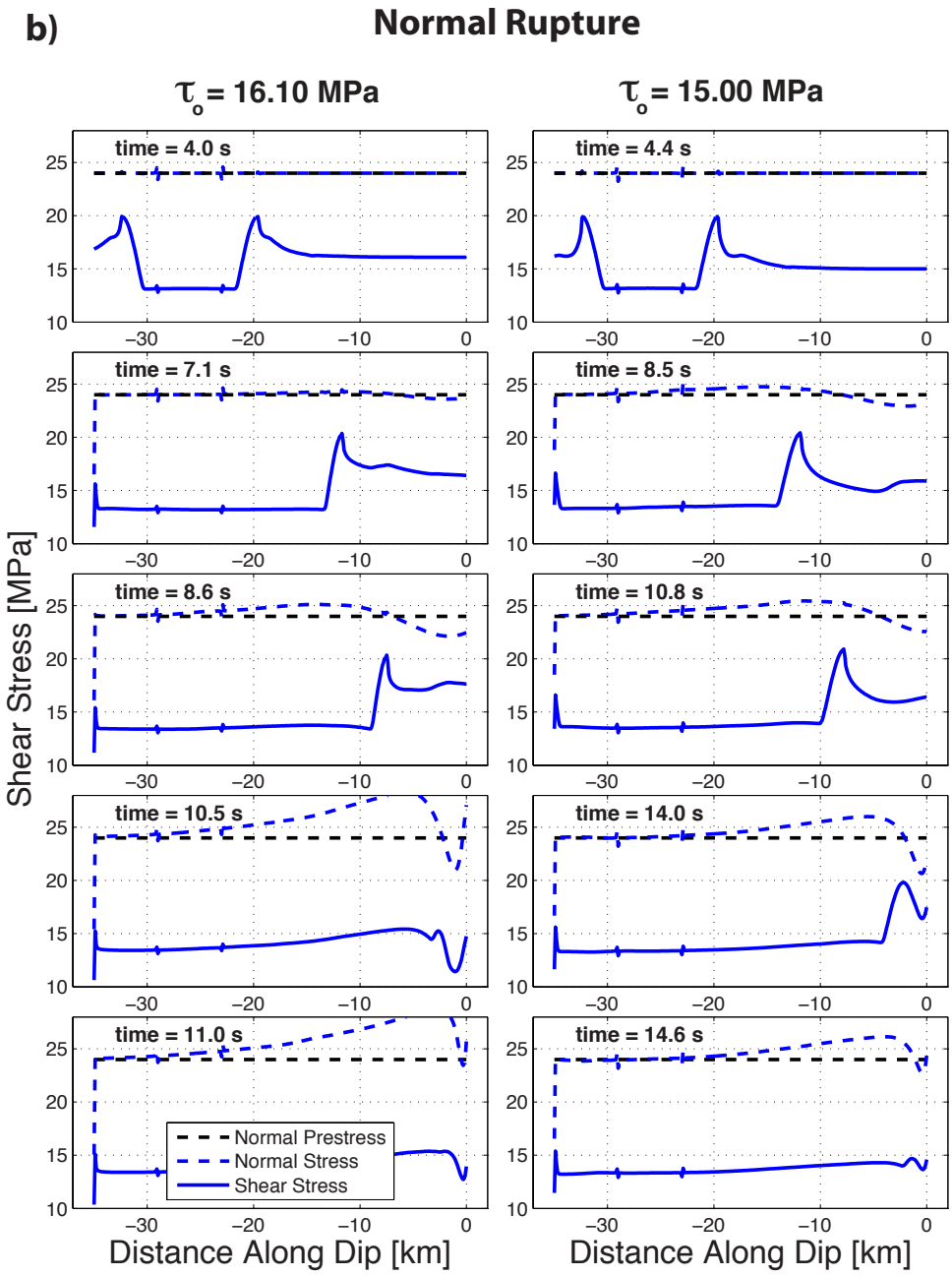

Figure 2.7b. Stress snapshots at different times for ageing law models with normal fault ruptures. In general, the sense of normal stress change on the fault reverses sign at roughly the location of the crack tip, consistent with previous studies (e.g., Nielsen, 1998; Oglesby et al., 1998; Oglesby and Archuleta, 2000a; Oglesby et al., 2000b). However, for lower initial shear stresses (e.g., 15Mpa), the rupture front tends to lag behind. For a normal fault, this effect sends the rupture front into an area of increased normal stress, hindering rupture. Results show larger static stress drops and smaller frictional energies for reverse-fault models relative to normal fault models.

in the τ_o = 15.00 MPa case in figure 2.7b). For some normal fault ruptures, a daughter crack forms ahead of the main rupture front near the free surface (< 5 km down dip).

Since the dynamic normal stress is quite low near the intersection of the fault with the free surface, an S-wave in front of the rupture front can reach the yield shear stress (figure 2.7b) resulting in complex ruptures near the free surface (Nielsen, 1998). Additionally, we see larger static stress drops and smaller or equal shear resistance for reverse-fault models relative to normal-fault models. In turn, this results in reverse ruptures propagating to the free surface even when normal ruptures cannot. In turn, we see larger fault, off-fault, and ground motion for reverse faults than normal faults for this parameter space.

All of the above models assume homogeneous frictional conditions along the entire down-dip extent of the fault. Realistically, however, faults are heterogeneous with regard to stress, geometry, friction, and material properties. In an effort to incorporate a more realistic frictional regime, we implement a RS-AL rate-strengthening zone in the uppermost (along dip) 5 km of a reverse rupture model and a normal rupture model with an initial loading stress of 15 MPa and $\alpha = 0$ (figure 2.8). In order to quantify such effects, we plot maximum and minimum shear stresses for both types of fault, with and without a rate-strengthening zone near the free surface. Without a rate-strengthening zone, reverse rupture travels up dip with smaller maximum and minimum shear stress

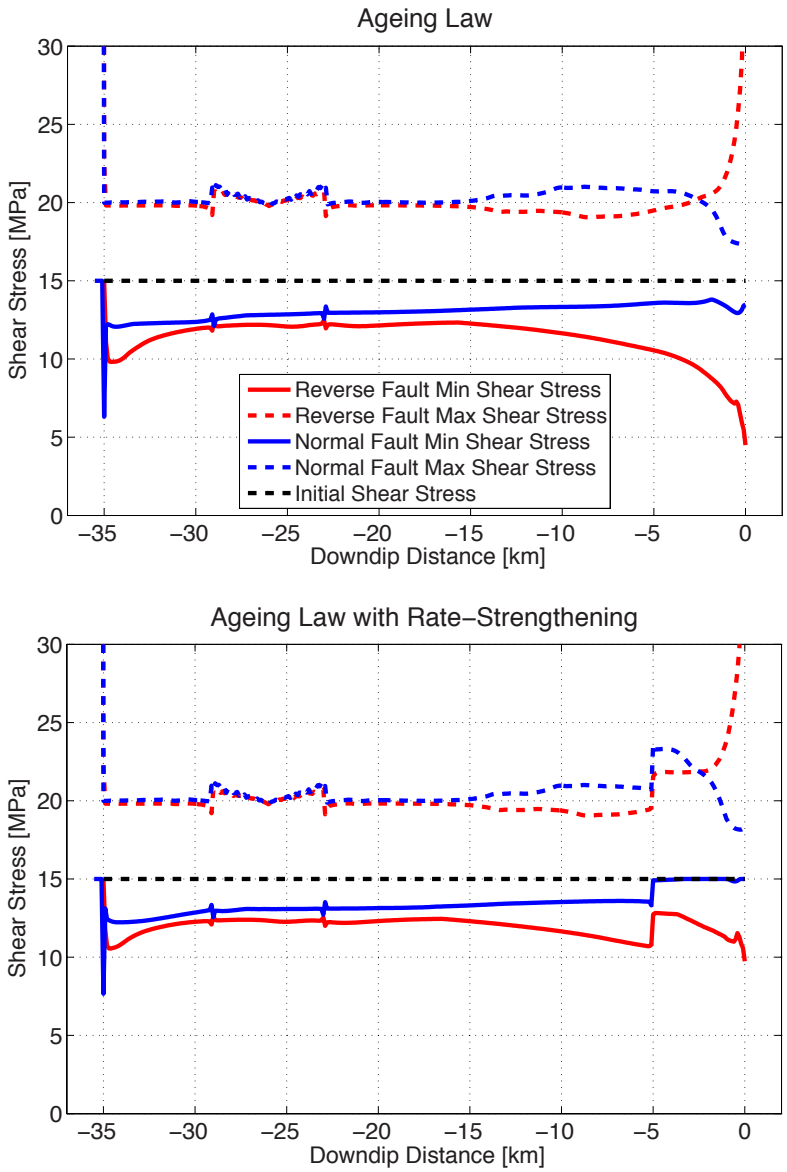

Figure 2.8. Minimum and maximum shear stress for both reverse (red) and normal-fault (blue) models with τ_o=15 MPa and α=0. Reverse rupture travels up dip with smaller maximum and minimum shear stress than the corresponding normal rupture until near the free surface (< 3 km), indicating a larger static stress drop than the normal rupture. For analogous models with a rate-strengthening zone near the free surface (0-5 km downdip), reverse rupture travels up dip with smaller maximum and minimum shear stress than the corresponding normal rupture; however, note that the normal-fault simulation has no significant stress drop in the rate-strengthening region while the reverse-fault simulation does (although both ruptures produce significant slip in the rate-strengthening region). These results indicate that the time-dependent normal stress induced by the free surface allows reverse rupture to more easily penetrate a rate-strengthening region near the surface, compared to normal fault rupture.

than the corresponding normal rupture until near the free surface (< 3 km), indicating a larger static stress drop than the normal rupture Near the free surface, the maximum shear stress for the reverse fault is greatly amplified, while the sliding frictional stress is greatly reduced. The normal fault reverses this pattern. With a rate-strengthening zone near the free surface, reverse rupture travels up dip with reduced maximum and minimum shear stress, much as in the no-rate-strengthening case. In particular, there is a strong stress drop even in the rate-strengthening zone near the free surface. However, the normal fault simulation shows no significant stress drop in the rate-strengthening region , although both ruptures produce significant slip in the rate-strengthening region. For the reverse fault case we see a large decrease in normal stress that results in a net stress drop and more slip than the normal fault in the rate-strengthening region. These results indicate that the time-dependent normal stress induced by the free surface allows thrust rupture to more easily penetrate a rate-strengthening region near the surface, compared to normal rupture. Rate-strengthening zones are normally associated with regions of stress increase during rupture. The current results indicate that it is possible to obtain a stress drop in a rate-strengthening zone due to a large free-surface-induced reduction in normal stress. Although the frictional coefficient inevitably increases in such a zone as slip accumulates (eq. 2.8), a large dynamic normal stress drop can compensate to ultimately lower the shear stress, resulting in a static stress drop (Kozdon and Dunham, 2012).

In light of the peak velocity differences between reverse and normal fault models, as well as the normal stress perturbations that seem to drive reverse ruptures more efficiently at

lower loading stresses, we examine particle velocities in the mesh. Figure 2.9 shows particle speed snapshots throughout the mesh for reverse and normal ruptures using the RS-AL with τ_o = 15 MPa and $\alpha = 0$. Snapshots at 4 seconds have identical particle motion amplitudes for both reverse and normal faulting, because no signal has yet arrived from the free surface to break the symmetry of the rupture process. However, at 8 seconds the reverse rupture begins to accelerate, and increased particle speed is apparent relative to the normal rupture. The reverse and normal fault ruptures breakout to the free surface at 13 seconds and 15 seconds, respectively, with the reverse case showing much larger particle motion. A sub-Rayleigh (S-R) breakout phase subsequently travels downdip to the base of each fault. At 18 and 20 seconds, respectively, the reverse rupture again shows larger particle motion. Additionally, we note the presence of a supershear (S-S) Mach cone traveling immediately behind a reflected P-wave downdip along the reverse fault. This is likely the result of changing normal stress (and thus the seismic S ratio, which controls rupture speed) values near the free surface. Large normal stress fluctuations are certainly a mechanism for such a supershear transition, as seen in previous stepover models (chapter 1). The Mach cone is not as clearly seen in the normal fault model, although it exists. This mode of supershear transition has not yet been reported or observed in the Earth to the best of our knowledge. We plan to investigate this supershear mechanism more thoroughly in future work by looking at more heterogeneous stress regimes, various dip angles, and other various material properties.

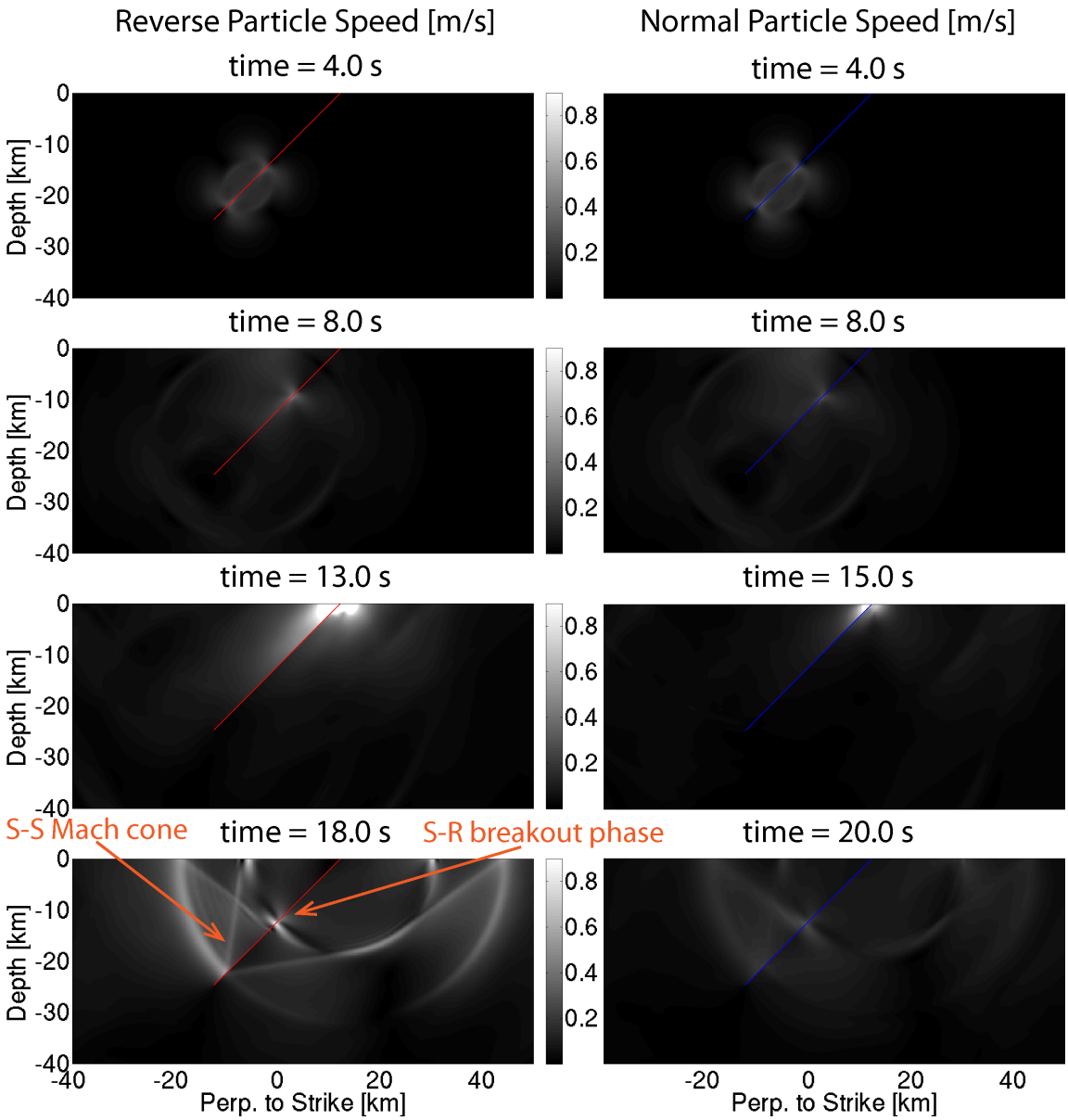

Figure 2.9. Particle speed snapshots at different times for ageing law models with reverse and normal fault ruptures (τ_o = 15MPa and α = 0). Red lines indicate a reverse fault; blue lines indicate a normal fault. Results show larger particle speeds for reverse fault models relative to normal fault models. Due to normal stress changes on each fault, rupture propagates much more energetically for the reverse case. At time steps 13 seconds and 15 seconds for the reverse and normal rupture, respectively, we see a more intense surface rupture for the reverse case. Later seen at time step 18 seconds, the sub-Rayleigh (S-R) breakout phase travels downdip along the reverse fault much more prominently than the normal fault. Additionally, a prominent supershear (S-S) Mach cone travels downdip ahead of the breakout phase along the reverse fault. The Mach cone and breakout phase have close proximity ground motions.

Discussion

Perturbations in normal stress have been experimentally determined to cause changes in the state variable, and therefore friction coefficient, of the opposite sign (Linker and Dieterich, 1992). This is quite significant for faults that are known to exhibit large dynamic fluctuations in normal stress during rupture, including both stepovers and dip-slip faults. Adding a normal-stress-dependent state variable to our stepover models reduces maximum rupture jump distance for both compressional and dilational models, due to the fact that both dilational and compressional steps lead to dynamic re-nucleation in regions of decreased normal stress. Although this idea may seem counterintuitive, since compressional steps are associated with large dynamic increases in normal stress near the step region, the complex stress fields generated in our models do show a decrease in normal stress that facilitates re-nucleation. Secondly, dilational steps tend to have larger decreases in maximum rupture jump due to a stronger reduction in normal stress, which leads to a corresponding stronger perturbation in state variable and frictional resistance. We tested this idea by examining slip-weakening plots for a point in the middle of the nucleation zone for each stepover type, showing that the normal stress dependence of state leads to a larger increase in dissipated energy for dilational steps than for compressional steps. A secondary mechanism for this result is the increased normal stress around the re-nucleation point for a compressional step, which leads to a decrease in frictional coefficient; however, this secondary mechanism can be critical-crack length dependent. Specifically, if the critical crack radius for re-nucleation does not encompass

this zone of decreased frictional coefficient, then the rupture would already be spontaneously propagating by the time it reached such a zone.

The above effects correspond to an overall decrease in the distance that rupture can jump using laboratory-derived friction laws with normal-stress-dependent state. Therefore, using classic slip-weakening friction may lead to an overestimation of maximum jump distance, given otherwise equivalent models. Whether or not rupture jumps a fault step certainly relates to the size of potential multi-segment earthquakes. Taking into account stepover width, fault segment overlap, whether or not the region is compressional or extensional, and absolute stresses at fault steps could be useful in hazard mitigation. Although absolute fault stress has proven difficult for seismologists to measure and therefore is somewhat arbitrary as a modeling parameter, many models are in good agreement with maximum jumping distances determined observationally (e.g., Harris and Day, 1993; Wesnousky, 1988). Dynamic models can and should continue using more realistic friction parameterizations since we can directly quantify friction in lab experiments. Additionally, high speed and large slip friction experiments can push the boundary of scaling laboratory earthquakes to real earthquakes (e.g., Tsutsumi and Shimamoto, 1997).

Decreasing the loading stress of the dip-slip models makes the slip pulses less crack-like (Zheng and Rice, 2000), however, we do not quantify this effect specifically. More importantly for the current study, decreasing loading stress eventually leads to ruptures

dying out on their way updip to the free surface; this effect is more pronounced for normal fault ruptures, consistent with reverse ruptures having smaller frictional resistance and lower final shear stress near the free surface. This effect does not necessarily lead to larger dynamic stress drops for reverse ruptures. Nonetheless, if the reverse and normal fault rupture fronts travel updip with the same frictional resistance (τ_o = 16.10 MPa case in figure 2.7) exactly at the border between regions of normal stress increase and decrease, then it is easily seen that the reverse rupture does have a larger dynamic stress drop. Most importantly, given the same initial conditions, reverse fault ruptures are more likely to reach the free surface and produce larger magnitude earthquakes. Adding a rate-strengthening zone near the free surface does not preclude the ruptures from having static stress drops, particularly in the case of thrust earthquakes. Static stress drop depends on the dynamics of the rupture. In our case, reverse rupture does have an increase in friction coefficient in the rate-strengthening zone (figure 2.8). However, there is also a large normal stress reduction (figure 2.7a), which leads to a net shear stress decrease and thus a stress drop.

Increasing the normal stress dependence of state variable (i.e., increasing α) in the dip-slip models tends to quench the difference in peak slip speed between reverse and normal faulting. However, the difference in total slip remains relatively small. This effect is probably due to a relatively unchanged energy budget for the models. In other words, the slope of the weakening curves change with changing alpha, however, the total dissipated energy (fracture energy) does not change much, so the energy left over for slip remains

largely unchanged. One can imagine fracture energy remaining the same if both the effective slip-weakening distance and the strength excess change by the right amount, and this is consistent with Guatteri and Spudich (2000) who suggest that the effective slip-weakening distance and the strength excess for earthquakes cannot both be determined accurately from fracture energy estimates. We note that d_o can change within are models, especially near the free surface, where large perturbations in normal stress alter shear stress weakening more substantially. Differences in peak slip speed (and to some small extent total slip) between reverse and normal ruptures result from differences in dynamic stress drop and frictional resistance. Thus, strong particle motion seen in the reverse models does not come from directivity, which would imply similar motion along both reverse and normal faults. Results can depend on dip angle, fault width, and the burial depth of the fault (e.g., Abrahamson and Somerville, 1996; Oglesby and Archuleta, 2000a).

Observationally, reverse/thrust ruptures are associated with large energy release and correspondingly large ground motion. Some examples of reverse faults reaching the surface include the 1973 San Fernando (Hanks, 1974) and the 1978 Tabas, Iran earthquakes (Berberian, 1982). Reverse faults often outcrop under the ocean, and can have large tsunami potential. Therefore our models would imply larger water height during tsunamigenesis for reverse ruptures. Additionally, adding a rate-strengthening region near the free surface may be one way to simulate tsunami earthquakes (Kanamori, 1972) that are devoid of strong, high frequency radiation. Our rate-strengthening models

show decreased rupture speed and decreased slip rate within the rate-strengthening zones that could simulate a slow earthquake rupture in the trench with substantial slip,

Brune (1996) argues that radiated energy estimates for thrust faults are underestimated due to 'trapped' waves in the hanging wall. Radiation patterns for reverse/normal faults could provide some insight into this idea. For example, figure 2.9 shows large particle speed in the hanging wall of the reverse rupture. Such trapped waves could be attenuated before reaching seismic equipment unless the equipment is close to the fault trace. The supershear Mach cone seen traveling downdip in the reverse rupture model has not been noted in other dip-slip studies (e.g., Oglesby and Archuleta, 2000a). Future work will include a more thorough investigation as to its mechanism including variations in dip angle and stress regime. Because the S-waves along the Mach cone may nearly coincide with the Rayleigh breakout phase along the free surface, observations for such a supershear transitions may not be obvious. Additionally, the standard Burridge-Andrews mechanism for supershear rupture cannot be applied to dynamic simulations with a free surface, therefore, a new set of criteria must be developed and used to investigate the free surface mechanism for supershear transition.

Using laboratory-based friction formulations such as rate- and state-dependent friction can make dynamic models of earthquake rupture more realistic. For earthquake ruptures that exhibit strong perturbations in normal stress, for example, stepovers and dip-slip faults intersecting the free surface, it is crucial to use laboratory-derived friction laws that

incorporate changes in normal stress. For our study, using too simplistic a friction law (e.g., linear slip-weakening friction) exaggerates both maximum jump distance as well as the asymmetric dynamics of compressional versus dilational steps and reverse versus normal fault ruptures. Although it is still somewhat unclear how such friction laws scale to large slip speeds and over large lengths (e.g., fault length), laboratory faults do indeed exhibit behaviors similar to real faults: steady creep, oscillatory creep, and unstable slip. Additionally, rate-state friction has reasonable properties including slip weakening, rate-strengthening, and healing (Dieterich, 1992). For very large changes in normal stress, the state variable may naturally saturate (approach a limiting value), and therefore we may be over predicting state variable changes in our models. For increments in normal stress that last for long time periods (10^3 or 10^4 seconds) the change in state variable is probably less accurate (Linker and Dieterich, 1992).

Our 2-D plane strain models can generalize to 3-D under our homogeneous conditions. However, since our models are 2-D there is a concentration of energy near the crack tip and an overestimation of particle motion. Stepovers with small step widths may produce some grid-dependent results if the dynamic waves interacting between the fault segments have much larger wavelengths than the step width. Normal stress fluctuations are well resolved in our models, as seen by the smooth transition in normal stress across elements. However, larger fluctuations in normal stress in larger absolute stress models than we have studied here may not be resolved from our discretization, especially if the fluctuations happen quickly in time (Andrews and Ben-Zion, 1997). We do not look at

specific frequencies of peak velocities, although they might provide a more robust comparison between reverse and normal faulting especially for more realistic ground motion (Abrahamson and Somerville, 1996), since attenuation is frequency dependent (e.g., Castro et al., 1995). Future work will incorporate more advanced geometries of dip-slip faults including rough and curved faults. Finally, we will look for the mechanism of the observed Mach cone in the dip-slip models by including such fault geometries as well as heterogeneous stress and velocity structure.

Conclusion

Overall, the range in rupture jump distance for our stepover models are in good agreement with both observational (e.g., Wesnousky, 1988; Elliot et al., 2009) and numerical studies (e.g., Harris and Day, 1993) even though the friction formulations employed produce slightly differing results. By equating the effective slip-weakening distance d_o of the friction formulations we cannot equate the fracture energies between different frictional parameterizations. Nonlinear weakening laws such as the rate-state slip law have relatively lower fracture energies and relatively higher seismic radiation energies when the weakening distance is equated. Perhaps a more accurate way to ensure that different friction parameterizations will produce similar results is to equate their fracture energies, since we have shown that doing so produces more similar maximum rupture jump distances between different friction laws. One way to increase accuracy further could be increasing the initial shear stress for models using the classic slip-weakening friction and the ageing law relative to slip law models, so all have the same

average amount of seismic radiation. It is definitely worth considering friction law effects for hazard analysis at stepovers, since maximum jump distance is related to maximum earthquake size. Friction governs the rupture process directly along the entire rupture path, and is equally as important as absolute stress levels and detailed fault geometry, although all of these are ultimately critical to more accurate modeling.

Using the more advanced Linker-Dieterich form of rate-state friction quenches the asymmetries that have been shown in previous stepover and dip-slip studies (e.g., Harris and Day, 1993; Oglesby et al., 1998). Intuitively, it can be easy to understand such a result when the friction coefficient compensates for changes in normal stress, since differences between compressional and dilational stepovers as well as normal and reverse faults are caused by fluctuations in normal stress.

For the same initial conditions, rupture propagation updip is hindered more in the normal fault case than the reverse fault case with decreasing loading stress. Decreasing the loading stress does not decrease the wave speeds of the elastic material, and therefore normal ruptures travel updip in less favorable conditions (larger shear strength and larger final shear stress) than reverse ruptures. It has been shown that intense asymmetries in normal and reverse-type faulting still exist with differing dip angles (Oglesby et al., 1998), but that the asymmetries reduce dramatically for buried dip-slip faults (Oglesby and Archuleta, 2000a, Oglesby et al., 2000b).

A novel and unexpected result of the current work is that a supershear transition can occur in both stepover and dip-slip models that would otherwise preclude the transition based on initial stress regimes in a symmetric whole space (Andrews, 1976b). Changes in normal stress produce conditions for the transition to occur on the secondary faults for high-stress stepover models and downdip for reverse fault and normal fault models (albeit with a much smaller intensity for the normal fault). Observing supershear transitions along stepovers may be possible by analyzing the direction of strongest ground motion, which is known to be fault parallel for strike-slip supershear ruptures (e.g. Dunham and Archuleta, 2004) rather than the more common fault-perpendicular direction for subshear rupture. However, to the author's knowledge no supershear transition has been observed for dip-slip ruptures. Our results show that the ground motion resulting from the breakout phase is in close proximity to the ground motion from the Mach cone that travels downdip after the rupture has reached the free surface. The breakout phase possibly masks any observations of the supershear slip pulse. Locating the breakout phase for such an observed rupture could provide a starting point to locate supershear pulses if they exist in nature. We plan to further investigate the cause of the supershear transition for dip-slip faults by exploring other geometries and stress regimes.

References

Abrahamson, N. A., and P. G. Somerville (1996). Effects of the Hanging Wall and Footwall on Ground Motions Recorded during the Northridge Earthquake, *Bull. Seismol. Soc. Am.* **86**, S93-S99.

Allen, C. R., J. N. Brune, L. S. Cluff, and Allan G. Barrows, Jr. (1998). Evidence for Unusually Strong Near-field Ground Motion on the Hanging Wall of the San Fernando Fault during the 1971 Earthquake, *Seismol. Res. Lett.* **69**, 524-531.

Andrews, D. J. (1976b). Rupture Velocity of Plane Strain Shear Cracks, *J. Geophys. Res.* **81**, 5679-5687.

Andrews, D. J. (1985). Dynamic Plane-Strain Shear Rupture with a Slip-Weakening Friction Law Calculated by a Boundary Integral Method, *Bull. Seismol. Soc. Am.* **75**.

Andrews, D. J. (2005). Rupture dynamics with energy loss outside the slip zone, *J. Geophys. Res.* **110**, doi:10.1029/2004JB003191.

Archuleta, R. J. (1984). A Faulting Model for the 1979 Imperial Valley Earthquake, *J. Geophys. Res.* **89**, 4559-4585.

Barall, M. (2008). FaultMod Finite Element Code, *available at http://scecdata.usc.edu/cvws/download/codedesc/Barall_FaultMod_Desc.pdf*.

Barall, M. (2009). A grid-doubling finite-element technique for calculating dynamic three-dimensional spontaneous rupture on an earthquake fault, *Geophys. J. Int.* **178**, 845-859.

Bartlett, W. L., Friedman, M., and J. M. Logan (1981). Experimental Folding and Faulting of Rocks Under Confining Pressure, *Tectonophysics* **79**, 255-277.

Beeler, N. M., and T. E. Tullis (Southern California Earthquake Center (SCEC), Los Angeles). Constitutive relationships for fault strength due to flash-heating, *SCEC Annual Meeting Proceedings and Abstracts, 2003*.

Beeler, N. M., Tullis, T. E., and D. L. Goldsby (2008). Constitutive relationships and physical basis of fault strength due to flash heating, *J. Geophys. Res.* **113**, doi:10.1029/2007JB004988.

Berberian, M. (1982). Aftershock tectonics of the 1978 Tabas-e-Golshan (Iran) earthquake sequence: a documented active 'thin- and thick-skinned tectonic' case, *Geophys. J. R. astr. Soc.* **68**, 499-530.

Bernard, P, and D. Baumont (2005). Shear Mach wave characterization for kinematic fault rupture models with constant supershear rupture velocity, *Geophys. J. Int.* **162**, 431-447.

Bernard, P, and R. Madariaga (1984). High-frequency seismic radiation from a buried circular fault, *Geophys. J. R. astr. Soc.* **78**, 1-17.

Bizzarri, A., and M. Cocco (2003). Slip-weakening behavior during the propagation of dynamic ruptures obeying rate- and state-dependent friction laws, *J. Geophys. Res.* **108**, doi:10.1029/2002JB002198.

Bizzarri, A., M. Cocco, D. J. Andrews, and E. Boschi (2001). Solving the dynamic rupture problem with different numerical approaches and constitutive laws, *Geophys. J. Int.* **144**, 656-678.

Bouchon, M., and M. Vallée (2003). Observation of Long Supershear Rupture During the Magnitude 8.1 Kunlunshan Earthquake, *Science* **301**, 824-826.

Brune, J. N. (1996). Particle motions in a physical model of shallow angle thrust faulting, *Proc. Indian Acad. Sci. (Earth Planet. Sci.)* **105**, L196-L206.

Brune, J. N., and A. Anooshehpoor (1999). Dynamic geometrical effects on strong ground motion in a normal fault model, *J. Geophys. Res.* **104**, 809-815.

Burridge, R. (1973). Admissible Speeds for Plane-Strain Self-Similar Shear Cracks with Friction but Lacking Cohesion, *Geophys. J. R. astr. Soc.* **35**, 439-455.

Burridge, R., and G. S. Halliday (1971). Dynamic Shear Cracks with Friction as Models for Shallow Focus Earthquakes, *Geophys. J. R. astr. Soc.* **25**, 261-283.

Castro, R. R., L. Munguia, and J. N. Brune (1995). Source Spectra and Site Response from P and S Waves of Local Earthquakes in the Oaxaca, Mexico, Subduction Zone, *Bull. Seismol. Soc. Am.* **85**, 923-936.

Chester, F. M. (1994). Effects of temperature on friction: Constitutive equations and experiments with quartz gouge, *J. Geophys. Res.* **99**, 7247-7261.

Chester, F. M., and N. G. Higgs (1992). Multimechanism Friction Constitutive Model for Ultrafine Quartz Gouge at Hypocentral Conditions, *J. Geophys. Res.* **97**, 1859-1870.

Cocco, M., and A. Bizzarri (2002). On the Slip-Weakening Behavior of Rate- and State-Dependent Constitutive laws, *Geophys. Res. Lett.*, doi:10.1029/2001GL013999.

Cocco, M., A. Bizzarri, and E. Tinti (2004). Physical interpretation of the breakdown process using a rate- and state-dependent friction law, *Tectonophysics*, 241-262.

Cocco, M., and A. Rovelli (1989). Evidence for the Variation of Stress Drop Between Normal and Thrust Faulting Earthquakes in Italy, *J. Geophys. Res.* **94**, 9399-9416.

Cochard, A., and J. R. Rice (2000). Fault rupture between dissimilar materials: Ill-posedness, regularization, and slip-pulse response, *J. Geophys. Res*.

Dalguer, L. A., and S. M. Day (2007). Staggered-grid split-node method for spontaneous rupture simulation, *J. Geophys. Res.* **112**, doi:10.1029/2006JB004467.

Das, S., and K. Aki (1977). Fault Plane With Barriers: A Versatile Earthquake Model, *J. Geophys. Res.* **82**, 5658-5670.

Day, S. M. (1982b). Three-dimensional Simulation of Spontaneous Rupture: The Effect of Nonuniform Prestress, *Bull. Seismol. Soc. Am.* **72**, 1881-1902.

Dieterich, J. H. (1978b). Time-dependent friction and the mechanics of stick-slip, *Pure Appl. Geophys.* **116**, 790-806.

Dieterich, J. H. (1979). Modeling of Rock Friction 1. Experimental Results and Constitutive Equations, *J. Geophys. Res.* **84**, 2161-2168.

Dieterich, J. H. (1992). Earthquake nucleation on faults with rate- and state-dependent strength, *Tectonophysics* **211**, 115-134.

Dieterich, J. H., and B. D. Kilgore (1994). Direct Observation of Frictional Contacts: New Insights for State-dependent Properties, *PAGEOPH* **143**, 283-302.

Duan, B., and D. D. Oglesby (2006). Heterogeneous fault stresses from previous earthquakes and the effect on dynamics of parallel strike-slip faults, *J. Geophys. Res.* **111**, doi:10.1029/2005JB004138.

Dunham, E. M. (2007). Conditions governing the occurrence of supershear ruptures under slip-weakening friction, *J. Geophys. Res.* **112**, doi:10.1029/2006JB004717.

Dunham, E. M., and R. J. Archuleta (2004). Evidence for a Supershear Transient during the 2002 Denali Fault Earthquake, *Bull. Seismol. Soc. Am.* **94**, S256-S268.

Dunham, E. M., P. Favreau, and J. M. Carlson (2003). A Supershear Transition Mechanism for Cracks, *Science* **299**, 1557-1559.

Ekström, G., Nettles, M., and A. M. Dziewoñski (2012). The global CMT project 2004-2010: Centroid-moment tensors for 13,017 earthquakes, *Phys. Earth Planet In.*, 1-9.

Elliot, A. J., J. F. Dolan, and D. D. Oglesby (2009). Evidence from coseismic slip gradients for dynamic control on rupture propagation and arrest through stepovers, *J. Geophys. Res.* **114**, doi:10.1029/2008JB005969.

Ellsworth, W. L., M. Celebi, J. R. Evans, E. G. Jensen, R. Kayen, M. C. Metz, D. J. Nyman, J. W. Roddick, P. Spudich, and C. D. Stephens (2004). Near-Field Ground Motion of the 2002 Denali Fault, Alaska, Earthquake Recorded at Pump Station 10, *Earthquake Spectra* **20**, 597-615.

Fukuyama, E., and K. B. Olsen (2002). A Condition for Super-shear Rupture Propagation in a Heterogeneous Stress Field, *Pure Appl. Geophys.* **159**, 2047-2056.

Goldsby, D. L., and T. E. Tullis (2002). Low Frictional strength of quartz rocks at subseismic slip rates, *Geophys. Res. Lett.* **29**, doi:10.1029/2002GL015240.

Guatteri, M., and P. Spudich (2000). What Can Strong-Motion Data Tell Us about Slip-Weakening Fault-Friction Laws, *Bull. Seismol. Soc. Am.* **90**, 98-116.

Gu, J. C., J. R. Rice, and A. L. Ruina (1984). Slip Motion and Stability of a Single Degree of Freedom Elastic System with Rate and State Dependent Friction, *J. Mech. Phys. Solids* **32**, 167-196.

Hanks, T. C. (1974). The Faulting Mechanism of the San Fernando Earthquake, *J. Geophys. Res.* **79**, 1215-1229.

Harris, R. A., and S. M. Day (1993). Dynamics of fault interaction - parallel strike-slip faults, *J. Geophys. Res.* **98**, 4461-4472.

Harris, R. A., R. J. Archuleta, and S. M. Day (1991). Fault Steps and the Dynamic Rupture Process: 2-D Numerical Simulations of a Spontaneously Propagating Shear Fracture, *Geophys. Res. Lett.* **18**, 893-896.

Harris, R. A., M. Barall, R. Archuleta, E. Dunham, B. Aagaard, J. P. Ampuero, H. Bhat, V. Cruz-Atienza, L. Dalguer, P. Dawson, S. Day, B. Duan, G. Ely, Y. Kaneko, Y. Kase, N. Lapusta, Y. Liu, S. Ma, D. Oglesby, K. Olsen, A. Pitarka, S. Song, and E. Templeton (2009). The SCEC/USGS Dynamic Earthquake Rupture Code Verification Exercise, *Seismol. Res. Lett.* **80**, 119-126.

Harris, R. A., and S. M. Day (1997). Effects of a Low-Velocity Zone on a Dynamic Rupture, *Bull. Seismol. Soc. Am.* **87**, 1267-1280.

Harris, R. A., and S. M. Day (1999). Dynamic 3D simulations of earthquakes on en echelon faults, *Geophys. Res. Lett.* **26**, 2089-2092.

Hirose, T., and T. Shimamoto (2005). Growth of the molten zone as a mechanism of slip weakening of simulated faults in gabbro during frictional melting, *J. Geophys. Res.* **110**, doi:10.1029/2004JB003207.

Hughes, T. J. R. (2000). The Finite Element Method, Linear Static and Dynamic Finite Element Analysis, *Dover Publications* New York, USA.

Hyndman, R. D., M. Yamano, and D. A. Oleskevich (1997). The seismogenic zone of subduction thrust faults, *The Island Arc* **6**, 244-260.

Ida, Y. (1972). Cohesive Force across the Tip of a Longitudinal-Shear Crack and Griffith's Specific Surface Energy, *J. Geophys. Res.* **77**, 3796-3805.

Ide, S., and M. Takeo (1997). Determination of constitutive relations of fault slip based on seismic wave analysis, *J. Geophys. Res.* **102**, 27379-27391.

Kanamori, H. (1972). Mechanism of Tsunami Earthquakes, *Phys. Earth Planet In.* **6**, 346-359.

Kanamori, H., and L. Rivera (2006). Energy Partitioning During an Earthquake, *Earthquakes: Radiated Energy and the Physics of Faulting. Geophysical Monograph Series 170* , doi:10.1029/170GM03.

Kase, Y., and K. Kuge (1998). Numerical simulation of spontaneous rupture processes on two non-coplanar faults: the effect of geometry on fault interaction, *Geophys. J. Int.* **135**, 911-922.

Kilgore, B. D., M. L. Blanpied, and J. H. Dieterich (1993). Velocity Dependent Friction of Granite Over a Wide Range of Conditions, *Geophys. Res. Lett.* **20**, 903-906.

Knuepfer, P. L. K. (1989). Implications of the characteristics of endpoints of historical surface fault ruptures for the nature of fault segmentation, *U. S. Geol. Surv. Open-file Rep.* , 193-228.

Kozdon, J. E., and E. M. Dunham (2012). Rupture to the Trench: Dynamic Simulations of the 11 March 2011 Tohoku Earthquake, *Bull. Seismol. Soc. Am.* Accepted for publication on 27 August 2012 Special Issue.

Lettis, W., Bachhuber, J., Witter, R., Brankman, C., Randolph, C. E., Barka, A., Page, W. D., and A. Kaya (2002). Influence of Releasing Step-Overs on Surface Fault Rupture and Fault Segmentation: Examples from the 17 August 1999 Izmit Earthquake on the North Anatolian Fault, Turkey, *Bull. Seismol. Soc. Am.* **92**, 19-42.

Linker, M. F., and J. H. Dieterich (1992). Effects of Variable Normal Stress on Rock Friction: Observations and Constitutive Equations, *J. Geophys. Res.* **97**, 4923-4940.

Liu, Y., and N. Lapusta (2008). Transition of mode II cracks from sub-Rayleigh to intersonic speeds in the presence of favorable heterogeneity, *J. of the Mechanics and Physics of Solids* **56**, 25-50.

Madariaga, R. (1976). Dynamics of an Expanding Circular Fault, *Bull. Seismol. Soc. Am.* **66**, 639-666.

Madariaga, R., and K. B. Olsen (2000). Criticality of Rupture Dynamics in 3-D, *Pure appl. geophys.* **157**, 1981-2001.

Mai, P. M., P. Somerville, A. Pitarka, L. Dalguer, S. Song, G. Beroza, H. Miyake, K. Irikura (2006). On Scaling of Fracture Energy and Stress Drop in Dynamic Rupture Models: Consequences for Near-Source Ground Motions, *Earthquakes: Radiated Energy and the Physics of Faulting. Geophysical Monograph Series 170* , 283-293.

Marone, C., and B. Kilgore (1993). Scaling of the critical slip distance for seismic faulting with shear strain in fault zones, *Letters to Nature* **362**, 618-621.

Marone, C., C. B. Raleigh, and C. H. Scholz (1990). Frictional Behavior and Constitutive Modeling of Simulated Fault Gouge, *J. Geophys. Res.* **95**, 7007-7025.

McGarr, A. (1984). Scaling of Ground Motion Parameters, State of Stress, and Focal Depth, *J. Geophys. Res.* **89**, 6969-6979.

Nason, R. (1973). Increased seismic shaking above a thrust fault; San Fernando, California, Earthquake of February 9, 1971, *U.S. Dept. of Commerce, Washington, D.C.*, 123-126.

Nielsen, S. B. (1998). Free surface effects on the propagation of dynamic rupture, *Geophys. Res. Lett.* **25**, 125-128.

Nielsen, S. B., and K. B. Olsen (2000). Constraints on Stress and Friction from Dynamic Rupture Models of the 1994 Northridge, California, Earthquake, *Pure Appl. Geophys.* **157**, 2029-2046.

Oglesby, D. D. (2005). The Dynamics of Strike-Slip Step-Overs with Linking Dip-Slip Faults, *Bull. Seismol. Soc. Am.* **95**, 1604-1622.

Oglesby, D. D. (2008). Rupture Termination and Jump on Parallel Offset Faults, *Bull. Seismol. Soc. Am.* **98**, 440-447.

Oglesby, D. D., and R. J. Archuleta (2000a). Dynamics of dip-slip faulting: Explorations in two dimensions, *J. Geophys. Res.* **105**, 13643-13653.

Oglesby, D. D., R. J. Archuleta, and S. B. Nielsen (1998). Earthquakes on Dipping Faults: The Effects of Broken Symmetry, *Science* **280**, 1055-1059.

Oglesby, D. D., R. J. Archuleta, and S. B. Nielsen (2000b). The Three-Dimensional Dynamics of Dipping Faults, *Bull. Seismol. Soc. Am.* **90**, 616-628.

Oglesby, D. D., P. M. Mai, K. Atakan, and S. Pucci (2008). Dynamic models of earthquakes on the North Anatolian fault zone under the Sea of Marmara: Effect of hypocenter location, *Geophys. Res. Lett.* **35**, doi:10.1029/2008GL035037.

Oglesby, D. D., and P. M. Mai (2012). Fault geometry, rupture dynamics and ground motion from potential earthquakes on the North Anatolian Fault under the Sea of Marmara, *Geophys. J. Int.* **188**, 1071-1087.

Okubo, P. G. (1989). Dynamic Rupture Modeling With Laboratory-Derived Constitutive Relations, *J. Geophys. Res.* **94**, 12321-12335.

Olsen, K. B., R. Madariaga, and R. J. Archuleta (1997). Three-Dimensional Dynamic Simulation of the 1992 Landers Earthquake, *Science* **278**, 834-838.

Olson, A. H., and R. J. Apsel (1982). Finite Faults and Inverse Theory with Applications to the 1979 Imperial Valley Earthquake, *Bull. Seismol. Soc. Am.* **72**, 1969-2001.

Palmer, A. C., and J. R. Rice (1973). The growth of slip surfaces in the progressive failure of over-consolidated clay, *Proc. Roy. Soc. Lond. A.* **332**, 527-548.

Prakash, V. (1998). Frictional response of sliding interfaces subjected to time varying normal pressures, *Journal of Tribology* **120**, 97-102.

Prakash, V., and F. Yuan (2004). Results of a Pilot Study to Investigate the Feasibility of Using New Experimental Techniques to Measure Sliding Resistance at Seismic Slip Rates, *American Geophysical Union, Fall Meeting 2004, abstract #T21D-02*.

Rabinowicz, E. (1951). The Nature of the Static and Kinetic Coefficients of Friction, *J. Appl. Phys.* **22**, 1373-1379.

Rice, J. R. (1999). Flash heating at asperity contacts and rate-dependent friction, *Eos Trans. AGU* **77**, Fall Meet. Suppl., F6811.

Rice, J. R. (2006). Heating and weakening of faults during earthquake slip, *J. Geophys. Res.* **111**, doi:10.1029/2005JB004006.

Rojas, O., E. M. Dunham, S. M. Day, L. A. Dalguer, and J. E. Castillo (2009). Finite difference modeling of rupture propagation with strong velocity-weakening friction, *Geophys. J. Int.* , doi:10.111/j.1365-246X.2009.04387.x.

Rosakis, A. J. (2002). Intersonic shear cracks and fault ruptures, *Advances in Physics* **51**, 1189-1257.

Rosakis, A. J., O. Samudrala, and D. Coker (1999). Cracks Faster than the Shear Wave Speed, *Science* **284**, 1337-1340.

Ruina, A. (1980). Friction laws and instabilities: A quasistatic analysis of some dry friction behavior, Ph.D. Thesis, Brown Univ., Providence, R. I.

Ruina, A. (1983). Slip Instability and State Variable Friction Laws, *J. Geophys. Res.* **88**, 10359-10370.

Scholz, C. H. (1998). Earthquakes and friction laws, *Nature* **391**, 37-42.

Segall, P., and D. D. Pollard (1980). Mechanics of Discontinuous Faults, *J. Geophys. Res.* **85**, 4337-4350.

Sibson, R. H. (1973). Interactions between Temperature and Pore-Fluid Pressure during Earthquake Faulting and a Mechanism for Partial or Total Stress Relief, *Nature Physical Science* **243**, 66-68.

Sieh, K., Jones, L., Hauksson, E., Hudnut, K., Eberhart-Phillips, D., Heaton, T., Hough, S., Hutton, K., Kanamori, H., Lilje, A., Lindvall, S., McGill, S. F., Mori, J., Rubin, C., Spotila, J. A., Stock, J., Thio, H. K., Treiman, J., Wernicke, B., and J. Zachariasen (1993). Near-Field Investigations of the Landers Earthquake Sequence, April to July 1992, *Science, New Series* **260**, 171-176.

Spudich, P., and E. Cranswick (1984). Direct Observation of Rupture Propagation During the 1979 Imperial Valley Earthquake Using a Short Baseline Accelerometer Array, *Bull. Seismol. Soc. Am.* **74**, 2083-2114.

Spudich, P., and L. Neil Frazer (1984). Use Ray Theory to Calculate High-frequency Radiation from Earthquake Sources having Spatially Variable Rupture Velocity and Stress Drop, *Bull. Seismol. Soc. Am.* **74**, 2061-2082.

Tsutsumi, A., and T. Shimamoto (1997). High-velocity frictional properties of gabbro, *Geophys. Res. Lett.* **24**, 699-702.

Tullis, T. E., and D. L. Goldsby (Southern California Earthquake Center (SCEC), Los Angeles). Laboratory experiments on fault shear resistance relevant to coseismic earthquake slip, *SCEC Annual Progress Report, 2003a*.

Tullis, T. E., and D. L. Goldsby (). Flash Melting of Crustal Rocks at Almost Seismic Slip Rates, *American Geophysical Union, Fall Meeting 2003b, abstract #S51B-05*.

Vedder, J. G., and R. E. Wallace (1970). Map showing recently active breaks along the San Andreas and related faults between Cholame Valley and Tejon Pass, California, *U. S. Geol. Surv. Misc. Field Invest. Map, I-574, scale 1:24000*.

Wesnousky, S. G. (1988). Seismological and structural evolution of strike-slip faults, *Nature* **335**, 340-343.

Wesnousky, S. G. (2006). Predicting the endpoints of earthquake ruptures, *Nature* **444**, 358-360.

Xia, K., A. J. Rosakis, and H. Kanamori (2004). Laboratory Earthquakes: The Sub-Rayleigh-to-Supershear Rupture Transition, *Science* **303**, 1859-1861.

Xia, K., A. J. Rosakis, H. Kanamori, and J. R. Rice (2005). Laboratory Earthquakes Along Inhomogeneous Faults: Directionality and Supershear, *Science* **308**, 681-684.

Zheng, G., and J. R. Rice (1998). Conditions under which Velocity-Weakening Friction Allows a Self-healing versus a Cracklike Mode of Rupture, *Bull. Seismol. Soc. Am.* **88**, 1466-1483.